LONG–TERM POTENTIATION AND MATHEMATICAL ANALYSIS OF ELECTRIAL MODELS OF DENDRITIC SPINES

by

RAJPAL SINGH THIARA

B.Sc. (Mathematics) University of Calgary, 1994

A THESIS SUBMITTED IN PARTIAL FULFILLMENT OF

THE REQUIREMENTS FOR THE DEGREE OF

MASTER OF SCIENCE

in

THE FACULTY OF GRADUATE STUDIES

Department of Mathematics
Institute of Applied Mathematics

We accept this thesis as conforming
to the required standard

THE UNIVERSITY OF BRITISH COLUMBIA

July 1998

In presenting this thesis in partial fulfillment of the requirements for an advanced degree at the University of British Columbia, I agree that the Library shall make it freely available for reference and study. I further agree that permission for extensive copying of this thesis for scholarly purposes may be granted by the head of my department or by his or her representatives. It is understood that copying or publication of this thesis for financial gain shall not be allowed without my written permission.

Department of Mathematics
The University of British Columbia
Vancouver, Canada

Date July 15/98

Abstract

Dendritic spines are small evaginations of the dendrites of neurons first discovered late in the 19th century. Since their discovery, many theories have been put forth to explain the physiological role of the spine. However, only recently with the advent of new laboratory technology has data been available to test the various theories put forward. The two most compelling theories today are that spines are important mediators of a form of cellular memory known as long–term potentiation (LTP), and that spines may be involved in the conduction of regenerative electrical impulses within dendrites similar to action potentials in axons.

We will review some of the major mathematical models put forth which attempt to explain the role spines may play in the induction of LTP. We will address the importance of calcium signals in LTP induction and suggest how the unique morphology of the spine may allow for transient, spatially localized increases in calcium within the spine head, but not elsewhere in the dendrite. This could help account for the associativity, cooperativity, and input specificity requirements of LTP.

We will also review some of the major mathematical models on dendritic action potentials. These models generally assume the existence of voltage–gated ion channels with Hodgkin–Huxley (HH) type dynamics exist in the spine head. We will employ a continuum approach in which spines are modeled as having a certain uniform density. We will further make use of the FitzHugh–Nagumo (FHN) equations without recovery to approximate the HH equations. We will examine the new set of equations in the traveling wave frame and seek to determine how the various parameters influence the speed, and the shape of the traveling wave front solutions. We show that there is a certain balance between local excitation of the spine heads, and freedom for the electrical current to pass from spine head to dendrite required for traveling front solutions to exist. Furthermore, strict parameter spaces in which traveling front solutions exist are determined, as is the profile of the wave in the special case of a standing wave.

Table of Contents

List of Figures

Acknowledgements

This thesis was produced under the supervision of Dr. Robert Miura, and was funded by a scholarship from the National Sciences and Engineering Research Council. I would like to thank Dr. Miura for his encouragement, support, and many suggestions on how to improve the thesis. I would also like to thank David Iron and Athan Spiros for their technical assistance in the production of the thesis.

Chapter 1
Introduction to Dendritic Spines

Cajal's classic work on neurophysiology [17] conclusively proved that the cell doctrine, the idea that all organs are made up of cells, applied equally well to the brain as it did to all other organs of the body. Since then, physiologists have pondered the role of the neuron's unusual morphology in its capacity for computation. The neuron contains highly arbourized appendages known as dendrites and axons, which branch off of a central body known as the soma. It is conventionally thought that the computational complexity of the brain is a consequence of the numerous connections neurons form with each other at synapses. By synapse we mean that morphological entity in which the terminal branch of an axon of one neuron, the presynaptic neuron, is directly opposed to another neuron, the postsynaptic neuron, but separated by some small distance (50 nm) [48]. It is estimated that there are approximately 10^{12} neurons each forming up to as many as 2×10^5 synaptic connections with other neurons [48]. Since it is thought that synapses are the main sites of "information transfer," this enormous connectivity makes the problem of decoding how the central nervous system (CNS) functions enormously difficult, and gross simplifications are required to elucidate important principles.

One classical simplification is the theory of dynamic polarization. This theory holds that dendrites act as antennae which are acted upon by neurotransmitters released at the axon terminal opposed to it in response to an action potential. These neurotransmitters cause a local change in conductance of the dendritic membrane to certain ions, resulting in a

passive electrical current which propagates towards the soma. This current is converted into a frequency of action potentials at the axon and is the sole output for a neuron.

The foundations of this theory were weakened by experimental and theoretical investigations of the granule cells in the olfactory bulb. It was shown that the dendrites of granule cells release neurotransmitters which mediate the inhibition of mitral and tufted cells [89]. This was the first demonstration that dendrites not only could receive inputs, but also could act as output devices. The key compartment is the dendritic spine, "the smallest neuronal compartment capable of performing a complete input–output operation of a single synapse" [105].

Spines are small evaginations of dendrites first noticed by Cajal in 1888 [17]. They are the site of type 1 excitatory synapses, which make up over 90% of all excitatory synapses in the CNS [31] with glutamate usually acting as the neurotransmitter [105]. The typical morphology of a spine is a small, roughly spherical head connected via a long, thin cylindrical stem to the dendrite [35]. Spines are typically just large enough to form one, or occasionally two synapses, and thus form "a structural, biochemical, and physiological compartment that is specific for that synapse" [35]. In this regard, it should be pointed out that the physical composition of spines is discontinuous from that of its parent dendrite.

The most obvious example of this discontinuity can be seen in the structure of the cytoskeleton [35] where there is the complete absence of microtubules. Instead, the cytoskeleton is composed of a loose filamentous network of actin and actin-regulating proteins which provide the scaffolding for the basic spine structure. The actin-regulating proteins, calmodulin (CaM), fodrin, myosin, and microtubule associated protein 2 (MAP2), interact with actin in a calcium–dependent manner. This interaction has been suggested as a mechanism underlying short–term memory [23]. One of the unique morphological

characteristics of the spine is the postsynaptic density (PSD) which is an area approximately 50 nm thick lying just beneath the spine head membrane and directly opposed to the axon terminal. Its dimensions are usually proportional to the dimensions of the spine head, but not the spine neck [36]. Furthermore, it has been shown that the area of the PSD also is proportional to the number of presynaptic vesicles in the axon terminal to which it is opposed, and this suggests that some form of pre– and postsynaptic dynamic coregulation is involved and points to a possible role for spines in regulating synaptic efficacy.

The spine also is unique in the presence of a select group of organelles [35]. All spines contain smooth endoplasmic reticula (SER), which is involved in Ca^{2+} sequestration and membrane synthesis. Many also contain polyribosomes, which function in protein synthesis. Some complex spines also contain mitochondria and multivesicular bodies which are restricted to the base of the spine. Thus, spines appear to have the capability of "independent energy metabolism, membrane turnover, and protein synthesis and thus in theory could function as a semi–autonomous unit within a neuron" [35]. In this light, it should be noted that von Neumann suggested that the fundamental unit of integration is not likely to be the whole neuron, but instead the single synapse [109]. The spine seems to be uniquely situated to mediate this role within the synapse.

This would not be of much interest except for the fact that there is experimental evidence suggesting that the spine may, in fact, actually perform such roles. Spines are degenerate or irregular in many mental disorders: thin and tiny in Down's syndrome and long and tortuous in mental retardation (Fragile X syndrome) [105]. Furthermore, in partial epilepsy, cortical pyramidal cells at a distance from the site of the seizure show simplified dendritic trees and decreased spine density, graded with the duration of the seizures. In less pathological cases, it has been shown that: 1) there are changes in spine stem length during field learning in honeybees, 2) rats trained in spatial learning show increased spine

densities on basal dendrites of CA1 hippocampal neurons, and 3) chicks show increased spine density in the lobus parolfactorius following one learning experience [35]. However, the best example of a role for spines in memory comes from the Bruce effect where exposure of unfamiliar male pheromones to an impregnated female causes abortion. This effect is thought to be mediated by metabotropic glutamate receptor 2 (mGluR2) in the olfactory granule spine [47] and could be prevented by the mGluR2 agonist, DCV–IV. As a result, it has been suggested that mGluR2s in the olfactory granule spine acts as a storage device for the original male pheromone [105]. Thus, there is an increasing amount of evidence suggesting that spines may be quite important both in memory and in normal cognitive function, but its exact role and the mechanism through which it accomplishes this still is largely unknown.

One of the great difficulties in studying dendritic spines is that their sizes situate them just at the edge of optical resolution using light microscopy (typical dimensions of dendritic spines in pyramidal cells of rodent neurons are 0.1–0.2 μm for the spine stem length, 0.04–0.2 μm for the spine stem diameter, 0.004–0.2 μm^3 for total spine volume, and 0.1–0.7 μm^2 for total spine surface area). Furthermore, they are virtually impossible to study in detail using traditional electrophysiological techniques as they cannot be impaled by electrodes and generally are electrically remote from the soma. Recently, more sophisticated fluorescence microscopy techniques have been developed and have allowed some insight into spine function. However, due to the long period before these new experimental techniques became available, and the great deal of interest in the possible roles of spines, many theories about how spine morphology could contribute to its hypothesized functions have been put forward.

Perhaps the simplest claim that has been made is that spines increase the surface area of the dendrites and simply serve to connect neurons [17]. However, it has been shown that even if all spines were removed from the dendrites in pyramidal cells there would still

be ample room for the formation of synapses in the dendrites. A more likely possibility in this regard is that spines "allow more synaptic connections to be compacted into a limited brain volume, and hence they can be considered the microscopic parallel to sulci and gyri in the brain"[35].

A recent claim that has begun to garner a great deal of interest is the idea that the spine acts as a compartment to allow for the biochemical amplification and spatial localization of second messengers that are produced as a result of local synaptic activity. Another area of interest has been the electrical roles that spines may have in mediating synaptic excitation. As a model system that has drawn a great deal of interest recently, we will review some theories put forth on how features of spines may be critical in the induction and expression of a cellular correlate of memory known as long–term potentiation (LTP) in Chapter 2 (for a more general review of LTP, see [12]). This chapter will serve as background material and is an area of much current interest amongst experimentalists and theoreticians in the neurosciences.

The remainder of the thesis will focus on theories put forth on the electrical roles that spines may play. We will start by giving a thorough review of the literature in Chapter 3. We will focus, in particular, on theories concerned with excitable dynamics. These theories suggest that there may be dendritic action potentials mediated by voltage–gated sodium and potassium channels within spine heads. Of special interest will be a continuum model developed by Baer and Rinzel [5] in which spines are not treated as individual entities, but rather are averaged out over space as a uniform density of spines. This allows several important simplifications to be made.

At this stage, the reader will be well acquainted with the various theories of excitable dynamics in spine heads, and some of the inferences made based on numerical experimentation. However, one failing of numerical simulations is that they fail to give one a good

grasp of what roles various biophysical features of a neuron are important in allowing for the existence of traveling wave pulse solutions. The reason that numerical simulations are so vitally important is that the system of equations used to approximate the excitable dynamics, the Hodgkin–Huxley equations, involve transcendental PDEs. A very successful approach that has been used over the years in this situation is to replace the complicated nonlinear functions with a cubic function and to replace the complicated recovery equations, with one simple linear ODE. This new set of equations is known as the Fitzhugh–Nagumo (FHN) equations, and they are amongst the most commonly studied set of equations in applied mathematics. Occasionally, instead of using a cubic nonlinearity as in the FHN equations, other functional forms are used. These equations are usually piecewise linear and attempt to mimic some of the general features of the cubic. The advantage of this approach is that the equations can be solved exactly. In Chapters 4, 5, and 6, we will use the FHN approach to simplify the equations governing the excitable dynamics in a continuum spine model of an infinite dendrite. In Chapter 4, the functional form we will use is a piecewise linear discontinuous function of the form $-v + H(v-a)$. In Chapter 5, the functional form we will use is a piecewise linear continuous function whose shape approximates that of a cubic polynomial. In Chapter 6, we will use the standard cubic used in the FHN equations. We will show how the various parameters play a role in determining whether traveling wave solutions exist and show how the speed of the propagating wave depends on the values of the parameters.

Chapter 2
Spines and Long-Term Potentiation

2.1 Introduction to Long-Term Potentiation

In 1949, Donald Hebb proposed a coincidence detection rule in which the strength of association between two neurons would increase if they were simultaneously active [38]. In 1973, such a phenomena was first observed in the dentate gyrus of anesthetized rabbits and was termed long-term potentiation (LTP) [11, 10]. LTP may be expressed as a persistent increase in the size of the synaptic component of the evoked response recorded from individual cells or from populations of neurons [12]. By persistent, we mean a stable increase in synaptic efficacy which lasts at least one hour. This is to be differentiated from shorter changes such as post–tetanic potentiation (PTP), which lasts on the order of seconds, and short–term potentiation (STP), which is a transient increase in synaptic weight that decays back to baseline within the first 30 minutes.

One of the most interesting features of LTP is that it is prominent in all areas of the hippocampus. This brain structure has long been implicated from lesion studies as being important to memory [104]. What is even more intriguing is that stimulation protocols that are capable of inducing LTP in the laboratory are qualitatively similar to those actually seen within the hippocampus during learning.

LTP exhibits three very important features that are expected of any cellular substrate of memory: cooperativity, associativity, and input–specificity [12]. Cooperativity is used

to describe the requirement that LTP has a threshold wherein weak stimuli are not encoded into an increase in synaptic efficacy. Such a mechanism is required to prevent "spontaneous memory" formation. Associativity means that a subthreshold activation at one synapse may become potentiated if there is strong activity at a nearby synapse. Thus the efficacy of a synapse is dependent upon its coactivity patterns with its neighbors. Input–specificity is the requirement that inactive synapses should not undergo an increase in efficacy. This once again can be viewed as some form of prevention of "spontaneous memory".

2.2 The Coincidence Detector

LTP has garnered a great deal of interest because of its possible linkage with memory and because it has yielded many fascinating biochemical results. One of the first problems to be dealt with was the identification of a coincidence detector. By a coincidence detector, we mean a cellular process which is activated during strong pre– and postsynaptic coactivation and serves as a signal for the induction of LTP [12]. In CA1 hippocampal pyramidal neurons, the coincidence detector is most likely a ligand–gated cation channel, the nicotinic–methyl–D–aspartate receptor (NMDAR), which opens in response to glutamate and NMDA. NMDARs are thought to be capable of functioning as the coincidence detector because they are largely blocked at potentials below -20 mV by Mg^{2+} [73]. Thus in order for a synapse to become potentiated, it has to be active, and the neuron has to be highly depolarized in the vicinity of the NMDAR. As a result, the neuron may be in the firing mode (threshold is typically a potential of ≈ -50mV at the axon hillock). In support of this theory, it has consistently been found that NMDAR antagonists block the induction of LTP [12, 73].

The next issue becomes what feature of NMDAR activation is crucial to LTP induction. NMDARs are highly calcium permeable, and $Ca^{2+}$is a potent second messenger capable of

initiating many different biochemical cascades involving enzymes such as protein kinases (PKs), which add PO_4^{3-} to proteins, and protein phosphatases (PPs) which remove PO_4^{3-} from proteins, and a variety of other proteins such as CaM and actin. Evidence for the importance of calcium in LTP induction comes from experiments which show that calcium chelators are capable of preventing the induction of LTP when administered to the postsynaptic neuron.

Thus, the idea that LTP is a calcium–dependent process depending on NMDAR activation became entrenched within the discipline. This led inevitably to the question about the nature of the calcium transients that are involved in the induction of LTP. It was generally accepted that there must be some sort of threshold relating to some feature of the calcium transient. Above this threshold, LTP would be induced, but below this threshold, only STP or perhaps even PTP could be induced. However, due to the limitations of experimental techniques, there was no known method of actually observing the calcium transients within dendritic spines, the presumed locus for LTP induction. As a result, a number of mathematical models were proposed to help gain insight into the importance of various biophysical systems thought to be important in mediating the calcium transients.

2.3 First Generation Mathematical Models of LTP

The first generation models of LTP focussed heavily on what was biophysically necessary to produce large, spatially localized Ca^{2+} transients under stimulation protocols similar to ones that experimentally induce LTP. It was thought that memory formation should involve some sort of a biochemical threshold. Below this threshold, there is very weak activation of a critical molecule, and above this threshold there is near maximal activation of this molecule. Thus, some recurring themes in these models were: the limitation of calcium channels to spine heads which acted as the sole source of calcium for the cell, and

a heterogeneous distribution of calcium pumps and calcium buffers (these are calcium–binding proteins (CaBPs) which generally diffuse slowly and can be seen to function, in some sense, as a capacitance [121]).

The basic physical geometry of the spine was a cylindrical spine head attached via a cylindrical spine stem to a cylindrical dendritic shaft. In some of the models, only a single spine stem was modeled, while in others, many were.

In the electrical part of models, the spine head was modeled as an isopotential compartment which is linked through a resistor to the parent dendrite. The resistor represents the theoretical total resistance conferred by the spine stem. This represents a lumped-sum resistance approximation which gives a good approximation to the actual system. Certainly, the amount of error introduced in this approximation is far smaller than the uncertainty in the electrical parameters used. The voltage in the dendrite was determined from the passive cable equation.

The motion of calcium was based on simple linear diffusion, coupled to nonlinear effects due to the pumps and buffers. The entry of Ca^{2+} is voltage–dependent and occurs only in the distal part of the spine head. Otherwise, the voltage and Ca^{2+} movement equations are decoupled. However, this may not be justified in small compartments such as dendritic spines [86].

The following parameters and variables are common in many of the following models and will be defined here:

Parameter or Variable name	*Description*
V_c	The synaptic reversal potential of a channel, c
$t_{peak,c}$	The time to peak conductance of a channel, c
g_c	peak conductance of a channel, c
C_m	specific membrane capacitance
R_m	specific membrane resistance
R_i	specific intracellular membrane resistance
$R_{\infty,sp}$	spine input resistance
$R_{\infty,d}$	infinite dendrite input resistance
D_{Ca}	calcium diffusion coefficient
R_N	spine neck resistance
r_n	radius of spine neck
l_n	length of spine neck
r_{sp}	radius of spine head
l_{sp}	length of spine head
r_d	radius of dendrite
kb_f	forward buffer rate constant
kb_b	backwards buffer rate constant
kp_i	rate constant for a first–order kinetic Ca^{2+} pump
K_{max}	Ca^{2+} turnover rate for a Ca^{2+} pump
P_s	surface density of a Ca^{2+} pump
K_d	constant of dissociation
F	Faraday's constant (9.6×10^4 Coulombs/mol)
$[B]$	concentration of Ca^{2+}–bound buffer
$[M]$	concentration of free buffer
$[Bt]$	total concentration of buffer
D_B	diffusion coefficient of the bound buffer

2.3.1 The First Attempt: Gamble and Koch, 1987

The first realistic LTP model was put forth by Gamble and Koch (GK) in 1987 [27]. In this model, the dendritic spine head contained synaptic receptors, voltage–gated calcium channels (VGCCs), voltage–gated noninactivating potassium channels, and a leak conductance. The spine head was heterogeneous and contained a specialized area under the outer circular face called the shell which roughly corresponds to the post–synaptic density. The spine neck also was divided into distal and proximal portions, which correspond to the sides furthest and nearest, respectively from the dendrite. The parent dendrite was homogeneous and contained only one leak conductance. Calcineurin and CaM were present as non–mobile, spatially inhomogeneous buffers. The concentrations of calcineurin and CaM were taken to be 10 μM and 50 μM, respectively, in the shell, and 5 μM and 25 μM, respectively, in all other areas. The binding of Ca^{2+} to calcineurin and to each of CaM's four Ca^{2+} binding sites was taken to be governed by first–order kinetics. There was also a non–saturable adenosine triphosphate (ATP) driven calcium–pump with first–order kinetics, an equilibrium value of 50 nM for $[Ca^{2+}]_i$, the intracellular calcium concentration, and a time constant of 2 ms located in a thin compartment apposed to the subsynaptic membrane.

Some of the main discoveries from this model were:

1. HFS is much more important than the total amount of synaptic activity in inducing large increases in $[Ca^{2+}]_i$ in small compartments such as dendritic spines.

2. The relative change in $[Ca^{2+}]_i$ was much smaller than the relative change in concentration of $Ca_4^{2+} - \text{CaM}$. This was due to the fact that the concentration of $Ca_4^{2+} - \text{CaM}$ depends on the fourth power of $[Ca^{2+}]_i$.

3. Synaptic activity at a nearby spine was simulated by the injection of depolarizing current during spike activity at the spine of interest. Depolarizing current more

than doubled the increase in $[Ca^{2+}]_{sp}$. the concentration of calcium within the spine head. This showed the possible importance of associativity in LTP.

4. The high input resistance of the spine allowed for much larger EPSPs in the spine head than in the parent dendrite. This allowed for the activation of high–threshold VGCCs.

2.3.2 The Second Attempt: Holmes and Levy, 1990

Holmes and Levy (HL) developed a model in 1990 looking for insights into how NMDARs might be important for the associative nature of LTP. They based their model on a rat hippocampal dentate granule cell and explicitly included 1–115 dendritic spines in their model. The model also contained buffers, pumps, and diffusion for Ca^{2+} . The model differed from the GK model in that it included other spines and a completely different set of receptors. The HL model included NMDARs and non–NMDARs, which were thought to conduct a mixed Na^+/K^+ current. The model had no VGCCs since they are not important in the induction of LTP in these cells, and there is little evidence for their existence in significant numbers.

At that point in time there was little quantitative information about the kinetics of the NMDARs. Thus, Holmes and Levy developed a mathematical model involving simple kinetics for receptor binding and for the transitions of receptor to different conductance states for both the NMDARs and non–NMDARs.

The qualitative features that they were trying to build into their model of NMDAR function were that the unbinding of neurotransmitters (NTs) from NMDARs had to be slow, the transition of the NMDAR–NT complex to an open channel state had to be even slower, the NMDAR is blocked by Mg^{2+} in a voltage–dependent manner, and the average number of NMDARs on a single spine head that were open at any given time had to be small (usually < 1). The approach used to calculate Ca^{2+} influx was simply to

determine the conductance of the NMDARs and turn it into a Ca^{2+} –flux by assuming that NMDARs were permeable to Ca^{2+}, Na^{+}, and K^{+} with a relative permeability ratio of $P_{Ca} : P_K : P_{Na}$ of 10.6:1.0:1.0. The important qualitative differences between the NMDARs and non–NMDARs were the longer mean open times for NMDARs,

The one major assumption made was the linearity of conductance addition. That is, the conductance changes due to activation of receptors from temporally separated presynaptic events do not affect each other. This assumption is only valid if the number of receptors bound to NTs is small compared to the number of receptors.

For the Ca^{2+} part of the model, the spine head was split into four compartments: two just under the outer circular surface of length 50 nm representing the PSD, and two more of length 225 nm. The spine neck was split into three roughly equal sized compartments. To model the Ca^{2+} in the vicinity of a spine, four dendritic compartments of length 0.5 μm were used, but adding additional ones didn't affect the $[Ca^{2+}]_{sp}$. Ca^{2+} movement between the different compartments was modeled according to simple linear diffusion between compartments, binding to buffers (based on CaM dynamics as assumed in the ZK model), and elimination by nonhomogeneously distributed pumps.

The main conclusions of this model were:

1. Prior theories about the NMDAR acting as the source of the nonlinearity in LTP are probably not true. It was previously thought that the voltage–dependence of the NMDAR could result in a positive feedback loop which would generate a large Ca^{2+} influx. However, Ca^{2+} influx could never be increased more than four–fold over the control.

2. The role of fast buffers is to amplify the nonlinearity in $[Ca^{2+}]_i$, and buffers play a more important role in modifying the Ca^{2+} transient than pumps, or diffusion.

3. The associativity of LTP could be seen in the voltage–dependence of the NMDAR

as it required a large number of coactive synapses firing at high frequency to result in large changes in Ca^{2+} influx, and $[Ca^{2+}]_{sp}$.

4. Dendritic spines, because of their small volume, "provide a locus for physiologically important transient increases in $[Ca^{2+}]_i$" [41].

2.3.3 The Third Attempt: Zador and Koch, 1990

Later in 1990, Zador and Koch (ZK) put forward a model [122], with the same spirit as the HL model. The basic models for the voltage equations were the same although only one spine was explicitly modeled, and the basic Ca^{2+} movement model was the same, incorporating diffusion, pumps, and buffers for Ca^{2+}. There were, however, a couple of differences which make this model worth noting.

The most fundamental difference is that the ZK model is based on CA1 hippocampal tissue with pyramidal neurons which is the most thoroughly studied tissue in the field of LTP research. The morphology of the model was similar to the one used in the previous two models with only slight quantitative differences. It should be noted that the value of the input resistance was much larger than in the HL model and result in less stringent requirements for associativity.

In the electrical model, explicit, empirical formulas for the forms of the time–dependent conductances for NMDA, and non–NMDAR (here it was based on AMPARs) were found:

$$g_{non-NMDA}(t) = \bar{g}_{non-NMDA}\frac{t}{t_{peak}}\exp\left(1-\frac{t}{t_{peak}}\right), \tag{2.1}$$

$$g_{NMDA}(t,V) = \bar{g}_{NMDA}\frac{\exp\left(\frac{-t}{\tau_1}\right)-\exp\left(\frac{-t}{\tau_2}\right)}{1+\eta[Mg^{2+}]\exp(-\gamma V)}, \tag{2.2}$$

where $g_{non-NMDA}$ is an alpha function with $t_{peak} = 1.5$ms, and a peak conductance of $\bar{g}_{non-NMDA} = .5$nS. The parameter values for g_{NMDA} were $\tau_1 = 80$ms, $\tau_2 = .67$ms, $\eta = 0.33\text{mM}^{-1}$, $\gamma = 0.06\text{mV}^{-1}$ and $\bar{g}_{NMDA} = 0.2\,\text{nS}$. The corresponding currents generated

in the spine head were calculated under the assumption of linear conductance addition as in the HL model.

In the Ca^{2+} part of the model, it was assumed that all of the Ca^{2+} influx was mediated by the NMDARs within the spine head. The factors involved in Ca^{2+} mobility were immobile cytosolic buffers based on CaM, as in previous models, a heterogeneous density of Ca^{2+} pumps obeying first–order Michaelis–Menton kinetics, and Ca^{2+} diffusion. The density of pumps in the proximal spine neck, the part closest to the dendrite, was much higher in the spine neck due to the possible presence of the spine apparatus which may be important in calcium sequestration. The method of determining the size of the calcium flux was to convert the current mediated by the NMDAR by using Faraday's constant, the valence of calcium, and by multiplying by 0.02, into the amount of the current thought to be due to Ca^{2+} .

The basic assumption of the modeling is that the degree of potentiation of a synapse should be a monotonic function of peak $[Ca_4CaM]$. Some of the results from these simulations were:

1. The high surface area to volume ratio of the pumps allowed for a great deal of separation between dendritic calcium concentration and spine calcium concentration. Thus spines are to a great extent isolated from each other with respect to calcium fluxes.

2. Ca^{2+} dynamics in the spine are quite sensitive to spine morphology and this could be an important mechanism in metaplasticity, the plasticity of synaptic plasticity [1] (for a model which explicitly explored this concept see [29]).

3. The associativity nature of LTP arises through the voltage–dependence of the NMDAR. It was found that a weak input which alone resulted in very little elevation of $[Ca^{2+}]_i$ in the spine could result in a much greater elevation of $[Ca^{2+}]_i$ if there

was enough activity at coactive synapses along the dendrite.

2.3.4 Conclusions about first generation LTP models

At this point, it would seem that these first models had done a credible job of explaining the robust experimental properties of LTP. LTP occurs when there is a sufficient amount of presynaptic activity at a synapse coupled to strong, local depolarization in the neighbourhood of the dendritic spine to alleviate the voltage–dependent Mg^{2+} block of the NMDAR — this explains the associativity and cooperativity properties of LTP. The spine is critical since its morphology allows large local changes in $[Ca^{2+}]_i$ due to the presence of buffers, the diffusional restriction of its thin neck, the presence of calcium pumps, and its small volume relative to that of its parent dendrite — this explains the input specificity of LTP. Lastly, the threshold nonlinear type behavior expected of LTP induction can be seen in the activation of CaBPs.

Part of the difficulty with the models as presented is that they are computationally intensive and fail to give much qualitative insight into the nature of calcium dynamics in a dendritic spine. One simplification is to identify a smaller number of lumped parameters whose values would give a good understanding of the nature of the calcium dynamics. If this is not possible, then a more thorough numerical investigation into how buffering, pumping, and diffusion parameters interact with spine shape to determine the shape of calcium transients should be carried out. Work has been done in both of these areas by Woolf and Greer who carried out numerical simulations on diffusion of second messengers in dendritic spines [118], and by Zador and Koch [121] who carried out analytical work (based on the approach used by Wagner and Keizer [110]).

2.4 Numerical Investigation of Second Messenger Diffusion in Dendritic Spines

Woolf and Greer numerically modeled the diffusion of second messengers in the dendritic spines of granule cells of the olfactory bulb. The spine morphologies were based on serial electron microscopy reconstruction [119]. These cells were chosen rather than hippocampal pyramidal cells since their spines have both input and output operations, and their necks are thinner and longer than hippocampal pyramidal cell dendritic spines so the lack of spatial localization of second messengers in the granule cell spines implies the same of the hippocampal pyramidal cell spines.

The numerical results of their simulations suggested the following:

1. In general, longer and thinner spine necks resulted in larger transients of second messengers in the spine heads, and longer times were required to reach peak concentrations in the spine neck.

2. Extrusion mechanisms often can be inefficient in spatial sequestration of second messenger signals at physiologically plausible density levels.

3. Binding mechanisms can profoundly affect the shape of second messenger transients and the ability of the signals to reach the base of the spine.

These results have some important implications. If there is a calcium–induced calcium release (CICR) mechanism in spine heads, then the effect may simply prolong the elevation of calcium in the spine head. However, if the release mechanisms are present in the spine neck and throughout the dendrite, then there could be active propagation of calcium signals from one spine head to another. There is also a question about the diffusion of activated CaBPs such as CaM. An important factor to consider here is the off–rate, or the rate of unbinding. CaM has a relatively rapid off–rate, so activated CaM levels will quickly decay once the calcium transient begins to die. Thus the degree of

localization will be strongly influenced by calcium–clearance mechanisms. The picture is a bit different for membrane–bound second messengers such as DAG and PKC. They will probably be restricted to the spine head and theoretically allow a much better spatial localization of the effects of synaptic activity than cytoplasmic diffusible second messengers such as Ca^{2+} . This suggests that modeling the effect of buffering on calcium transients by scaling the diffusion coefficient of calcium may lead to qualitatively incorrect results.

2.5 Linearizing Calcium Dynamics through Asymptotic Expansions

To obtain a better understanding of the non–linear calcium dynamics, Zador and Koch [121] show how it is possible in certain limiting cases to reduce the dynamics to one linear PDE with constant coefficients in cylindrical domains. This equation is formally identical to the cable equation in the low $[Ca^{2+}]_i$ range, and simple linear diffusion in the high $[Ca^{2+}]_i$ range. Their method used asymptotics for cases in which $[Ca^{2+}]_i$ is expected to be small and large relative to certain parameters and then to determine a leading order equation.

The calcium dynamics involve diffusion, saturable pumps obeying Michaelis–Menton dynamics, and diffusible buffers. The governing system of equations are

$$\frac{\partial [Ca]}{\partial t} = D_{Ca}\frac{\partial^2 [Ca]}{\partial x^2} - P([Ca]) - kb_f[Ca][M] + kb_b[B] + \frac{2}{r}f(x,t), \tag{2.3}$$

$$\frac{\partial [B]}{\partial t} = D_b\frac{\partial^2 [B]}{\partial x^2} + kb_f[M][Ca] - kb_b[B], \tag{2.4}$$

$$[Bt] = [M](x,t) + [B](x,t), \tag{2.5}$$

where $P[Ca]$ is the contribution of the pump term, D_B is the diffusion coefficient of bound buffer, r is the radius of the cylinder, and $\frac{2}{r}f(x,t)$ is a source term. Here we have made the implicit assumption that $[Bt]$ is a constant which is tantamount to a spatially homogeneous distribution of buffers and equivalent diffusion coefficients for bound and

free buffers.

There are two assumptions that are critical in the reduction. The first is to assume that the time scale of diffusion is much longer than the time scale for buffering (i.e. for a length l, we require $\frac{l^2}{D_B} \gg \tau_B$ where $\tau_B = \frac{1}{kb_b + kb_f[Ca]}$). If we follow the methods of Zador and Koch, we can obtain a single equation for the Ca^{2+} dynamics

$$(1 + \beta[Ca])\frac{\partial[Ca]}{\partial t} = \frac{\partial}{\partial x}\left[(D_{Ca} + D_B\beta([Ca]))\frac{\partial[Ca]}{\partial x}\right] - P([Ca]) + \frac{2}{r}f(x,t). \qquad (2.6)$$

The second assumption has to do with looking at high and low Ca^{2+} limits of the terms in equation (2.6).

First, let us consider the low calcium limit. If we assume that $[Ca] \ll K_{d,B}$, and $[Ca] \ll K_{d,p}$ the leading order equation becomes

$$(1 + \beta)\frac{\partial[Ca]}{\partial t} = (D_{Ca} + \beta D_B)\frac{\partial^2[Ca]}{\partial x^2} - \frac{2K_{max}P_s}{r}[Ca] + \frac{2}{r}f(x,t) \qquad (2.7)$$

where $\beta = \frac{[B_t]}{K_{d,B}}$. If we multiply both sides by $r/2$ we can rewrite the above equation as:

$$\begin{aligned} \frac{r(1+\beta)}{2}\frac{\partial[Ca]}{\partial t} &= \frac{r(D_{Ca} + \beta D_B)}{2}\frac{\partial^2[Ca]}{\partial x^2} \\ &\quad -P_sK_{max}[Ca] + K_\infty P_sK_{max}I(x,t), \qquad (2.8) \\ I(x,t) &= \frac{f(x,t)}{P_sK_{max}K_\infty}. \qquad (2.9) \end{aligned}$$

Now notice that if $I(x,t) = I_0$ is a constant and we look for steady state solutions of (2.8), we get

$$K_\infty = \lim_{t\to\infty}\frac{[Ca](x,0)}{I_0}. \qquad (2.10)$$

If we make the following substitutions:

$$R_m = P_s K_{max}, \tag{2.11}$$

$$C_m = \frac{r(1+\beta)}{2}, \tag{2.12}$$

$$R_i = \frac{1}{D_{Ca} + \beta D_B}, \tag{2.13}$$

$$R_\infty = K_\infty, \tag{2.14}$$

$$V = [Ca], \tag{2.15}$$

into (2.8), we obtain

$$C_m \frac{\partial V}{\partial t} = \frac{r}{2R_i} \frac{\partial^2 V}{\partial x^2} - \frac{1}{R_m} V + \frac{R_\infty}{R_m} I(x,t), \tag{2.16}$$

which is readily recognized as the cable equation with a normalized current source term. The value of doing this is that the cable equation has been very thoroughly studied (see [43]). In the framework of the cable equation, we can see the pump acting like a membrane resistance, the buffers contributing to the capacitance, and the diffusion terms acting like intracellular resistances. More quantitatively, we can immediately define quantities such as the space constant, λ, the time constant, τ, and the input resistance of an infinite cable, R_∞. In cable theory, these quantities are determined by the following formulas

$$\lambda = \sqrt{\frac{r R_m}{2R_i}}, \tag{2.17}$$

$$\tau = R_m C_m, \tag{2.18}$$

$$R_\infty = \frac{(2r)^{-\frac{3}{2}}}{\pi} \sqrt{\frac{R_m}{R_i}}. \tag{2.19}$$

If we now substitute (2.11)–(2.14) into the expressions listed above, we get

$$\lambda_C = \sqrt{\frac{r(1+\beta)}{2P_s K_{max}}}, \tag{2.20}$$

$$\tau_C = \sqrt{\frac{r(D_{Ca} + \beta D_B)}{2P_s K_{max}}}, \tag{2.21}$$

$$K_\infty = \frac{(2r)^{-\frac{3}{2}}}{\pi \sqrt{(D_{Ca} + \beta D_B) P_s K_{max}}}, \tag{2.22}$$

where λ_C is the chemical space constant, τ_C is the chemical time constant, and K_∞ is the chemical input resistance of an infinite cylinder. Now notice that τ_C is dependent on the radius of the cylinder, but τ is not. Thus the time required for equilibration is going to be much larger for a larger cylinder. In particular, the time constant is expected to be small for a structure such as a dendritic spine suggesting that $[Ca^{2+}]_{sp}$ could rise quickly during stimulation and return to normal levels quickly at the end of stimulation. Also notice that just as in the electrical case, the space constant scales like the square root of the radius. However, the one big difference is that for reasonable physiological values of the given parameters, $\lambda_C \ll \lambda$. It can, in fact, be up to three orders of magnitude shorter than the electrical space constant. Thus, it is expected that the localization of chemical signals is going to be much more efficient than the localization of electrical signals within neurons.]

A similar reduction can be performed in the high calcium limit. If one applied this assumption as we did with the low calcium limit, one could reduce the calcium dynamics to a simple linear diffusion equation with a source. In this case, the buffers and pumps are totally saturated, and all the essential nonlinearities are removed.

Zador and Koch then applied this linearization in the low Ca^{2+} limit to their ZK model. One of their observations was that the chemical input resistance of the spine was 10 times larger than that of the parent dendrite. Thus, the same source located on the spine will produce a much larger transient than if it were located on the parent dendrite. Furthermore, the chemical space constant of the spine neck was 0.27 μm making the spine neck length $\approx 4\lambda_C$ which means that steady state $[Ca^{2+}]_{sp}$ would decay by a factor of ≈ 55 by the time it reached the parent dendrite. Furthermore, the small radius of the spine neck and head also mean that spines have much smaller chemical time constants than the parent dendrite. This will only further amplify the concentration gradient between spine head and parent dendrite during calcium transients. This result shows

how important the morphology of the spine is in both allowing for the development of a large, transient increase in $[Ca^{2+}]_{sp}$ while simultaneously limiting the extent to which it will spread throughout a dendrite.

Another interesting facet of the linearized Ca^{2+} dynamics can be seen in the morpho-electrotonic transform [123]. Not only are local Ca^{2+} transients in active spines isolated from the dendritic shaft, but Ca^{2+} transients in the dendritic shaft are to a large extent isolated from the spine heads. This is in contrast to the tremendous voltage attenuation from spine head to dendrite when there is an input to the spine head, but when there is an input to the dendrite then there is very little voltage attenuation from dendrite to spine head [88].

This gives us a good understanding of calcium dynamics and how spines provide a microenvironment for large changes in $[Ca^{2+}]_{sp}$. However, LTP cannot be explained simply as a result of Ca^{2+} influx through NMDARs when strong presynaptic activity is coupled to strong depolarization in the neighbourhood of the spine, with the resulting large non-linear increase $[Ca^{2+}]_i$ in the spine, and the activation of CaBPs and Ca^{2+}–dependent enzymes. Thus, the modeling cannot end here.

2.6 The Spatial Nature of Ca^{2+} Transients in LTP

Due to the input–specificity requirements of LTP, the Ca^{2+} transient must be severely restricted spatially in order to prevent the induction of LTP at adjacent synapses. Thus, it has been suggested that the dendritic spine may act as a separate compartment from the parent dendrite which acts to amplify the $[Ca^{2+}]_i$ for a given level of stimulation [81]. This idea was built into the models reviewed above in the form of calcium pumps and buffers within the spine. However, only in the last few years have experimental techniques to measure $[Ca^{2+}]_i$ in dendritic spines been developed.

It has been found in a number of experiments that the $[Ca^{2+}]_{sp}$, the concentration of Ca^{2+} in the spine head, is significantly higher than $[Ca^{2+}]_d$, the concentration of Ca^{2+} in the parent dendrite, during synaptic stimulation [84, 75]. This difference could largely be negated by application of the NMDAR antagonist, D–APV . Furthermore, bath application of NMDA resulted in values of $[Ca^{2+}]_{sp}$ greater than $[Ca^{2+}]_d$ in a manner depending on $[Ca^{2+}]_o$, the extracellular calcium concentration [101]. Lastly, depolarization of the soma to -20 mV results in a larger increase in $[Ca^{2+}]_{sp}$ than in $[Ca^{2+}]_d$ [101, 99]. This difference could be blocked by application of L–type voltage gated calcium channel (VGCC) blockers, but not by either a P–type VGCC blocker or an N–type VGCC blocker. This suggests that spines have a hyperconcentration of NMDARs and L–type VGCCs compared to the parent dendrites, or a smaller concentration of CaBPs as assumed in the mathematical models of LTP. For example , a recent experiment [32, 33] followed the dispersal of Ca^{2+} in a dendrite that was temporarily made permeable to Ca^{2+} . It was found that there was a significant lag in the change in $[Ca^{2+}]_{sp}$ compared to $[Ca^{2+}]_d$ in one–third of all spines. This difference was more frequently found in spines with long, thin stems than in spines with short, stubby stems.

However, it should be noted that the lag in spines for spreading Ca^{2+} was not due to a physical diffusion barrier as there was no lag in the change in $[Co^{2+}]$ between spine and parent dendrite when Co^{2+} was substituted for Ca^{2+} in the extracellular fluid (ECF). This suggests the possible importance of calcium pumps in keeping $[Ca^{2+}]_{sp}$ somewhat isolated from $[Ca^{2+}]_d$. However, notice that the degree of difference is considerably smaller than that suggested theoretically. This may in large part be due to the fact that calcium fluorescence techniques do not actually measure the Ca^{2+} directly but rather the concentration of calcium bound to certain exogenous CaBPs which fluoresce when irradiated with light of certain wavelengths.

The idea that calcium dynamics are not always as intuitive as one might think is an

important one when dealing with such a qualitative endeavor. Nowycky and Pinter [78] performed a rigorous numerical analysis of the motion of Ca^{2+} and CaBPs in model cells (for a less rigorous treatment of simulations of the movement of CaBPs, but one that is specific to spines see [45]). One of their chief results was the spatio–temporal distribution of Ca^{2+} –bound buffers and Ca^{2+} can be quite different. This is especially true for small, mobile calcium chelators such as fura–2 which are typically used in calcium fluorescence experiments. This may partially explain the paradoxical results of the above experiment.

2.7 The temporal nature of Ca^{2+} transients in LTP

The experimental data shows reasonable qualitative agreement with the theoretical models in terms of limiting the spread of Ca^{2+} . Unfortunately, the same cannot be said of the temporal nature of the Ca^{2+} transients.

In a recent study [64], a photolabile Ca^{2+} chelator, diazo–4, which increases its affinity for calcium 1600–fold upon exposure to intense light, was used to determine some of the temporal features of the Ca^{2+} signal required to induce LTP. A stimulus which normally induces LTP (100 Hz stimulation for 1 s) was found to induce PTP if the light was applied 1 second after the beginning of the stimulus (1s of 100 Hz stimulation), STP or weak LTP if light was applied 1.5–2.0 seconds following the beginning of the stimulus, and full LTP if the light was shone 2.5 seconds or later after the beginning of the stimulus. While these results may possibly allow for the release of Ca^{2+} from intracellular stores such as the SER, they do rule out any possible influences due to long–lasting Ca^{2+} waves or oscillations. Furthermore, since the peak $[Ca^{2+}]_i$ is reached within 1.5 seconds when only STP was induced, this indicates that incomplete activation of some quickly activated $[Ca^{2+}]_i$ dependent process does not distinguish whether STP or LTP is induced. This is where the models discussed above fail. The Ca^{2+}–dependent processes that were assumed to underlie LTP were quick, and the peak level of $[Ca^{2+}]_i$ in these simulations occurred

well before that noticed during experiments (this can be seen in the small value of τ_C). Thus, the nature of the nonlinearity that is produced during LTP could not be of the type that would have been noted in the previous modeling efforts. We will need to consider some more results from the biology of LTP before attempting to proceed.

While a fairly robust result in LTP has been the requirement of increase in $[Ca^{2+}]_i$ and the activation of NMDARs, there are other possible sources of Ca^{2+} such as the SER.

CA1 hippocampal pyramidal neuron dendritic spines contain a high concentration of mGluR5 [94], a metabotropic glutamate receptor, which catalyzes the hydrolysis of phosphoinositide bis–phosphate (PIP_2) to inositol trisphosphate (IP_3) and diacylglycerol (DAG). IP_3 acts on IP_3 receptors located in the SER to cause release of Ca^{2+} (see [9] for a review), while DAG is a potent activator of protein kinase C (PKC). This is of some interest since it is known that IP_3 receptors are found in CA1 hippocampal pyramidal neurons but ryanodine receptors (RyRs) which are involved in calcium–induced calcium release (CICR) processes are not, even though they are typically found in high concentrations in dendritic spines [103]. Furthermore, IP_3 is produced during the induction of LTP [37], and topical application of IP_3 to their dendrites can result in a Ca^{2+} wave which propagates throughout the dendrite [44]. Moreover, thapsigargin [7, 37] and dantrium [79], which act to inhibit the release of Ca^{2+} from intracellular stores, can prevent the induction of LTP. A direct link between these results and a role for mGlur5 comes from agonist/antagonist studies. mGluR5 antagonists have been shown to prevent the induction of LTP [6], while agonists have been shown to be capable of potentiating LTP [20, 13, 14]. The effects of mGluR5 agonists could be prevented by thapsigargin which strengthen the link between intracellular Ca^{2+} stores and the induction of LTP. In light of this evidence, I will now review a model of LTP which explicitly included the presence of intracellular calcium stores.

2.7.1 A Model of Ca^{2+} Dynamics in Dendritic Spines

Schiegg et al. developed a model [97] in 1995 which incorporated a mechanism for the release of Ca^{2+} from intracellular stores as a result of the experimental results noted above. In particular, they were concerned with meeting the criterion for elevated levels of $[Ca^{2+}]_{sp}$ for $2 - 2.5$ s as noted in the study using the photoactivable calcium chelator, diazo–4 [64].

The modeling approach was to use a 10 compartment electrical model of a CA1 hippocampal pyramidal neuron split into a soma compartment, a basilar bush, a lower apical branch, and an upper apical branch which is subdivided into 6 dendritic compartments. The upper apical branch was subdivided to allow better spatial resolution in the neighbourhood of the synaptic input. A set of $Nspine$ identical spines were attached to the fourth dendritic compartment away from the soma on the upper apical branch. The spine morphology was as before, a cylindrical spine head attached via a spine neck, which was reduced to a lumped potential in the electrical model, to the parent dendrite. It further was assumed that there was synchronous activity in each spine, and thus the voltage and current loss to the dendrite was the same for each spine. As a result, only one spine needed to be explicitly included in the electrical model. The voltage channels used in this model were based on the NMDA and non–NMDAR currents used by Zador and Koch [122].

The calcium dynamics were essentially the same as in the ZK model. The spine head was split into three compartments in the discretization, with all synaptic channels located in the subsynaptic compartment. The spine neck also was subdivided into three compartments. There are a couple of differences worth noting. First, it was assumed that 10% of the current flowing through the NMDAR is due to Ca^{2+}, rather than the 2% used in the ZK model. Rather than model the four separate sites on CaM, which was assumed

to have a total concentration of $\approx 30\,\mu$M, it was assumed that there was a buffer with a single calcium binding site with $[Bt] = 120\,\mu$M in the spine. The forward and backward binding constants of the buffers were the same as in the ZK model. The form of the pumps were as in the ZK model, but the pump efficiencies were larger than the values used in the ZK model by a factor of 10. Rather than explicitly model the $[Ca^{2+}]_d$, it was assumed that $[Ca^{2+}]_d$ was clamped at 50 nM. However, by far the biggest difference between the two models is the inclusion of a CICR mechanism in this model.

Both the IP_3 receptor and the RyR show a bell–shaped calcium response with little calcium release at low $[Ca^{2+}]_i$ and high $[Ca^{2+}]_i$. Rather than using a detailed model of both IP_3 receptors and RYRs, Schiegg et al. combined the two in the form of one phenomenological equation with a bell–shaped calcium dependence. It was assumed that there was one common intracellular Ca^{2+} pool which occupied $\frac{1}{10}^{th}$ of the spine head volume. In the discretization scheme used, this intracellular pool was placed in the second compartment, directly below the subsynaptic membrane. The release of Ca^{2+} from this store and into the second spine compartment is modeled by

$$\frac{\partial [Ca]_{store}}{\partial t} = \rho X \left([Ca]_{store} - [Ca]_2 \right) \tag{2.23}$$

where $[Ca]_{store}$ is the concentration of Ca^{2+} in the store, $[Ca]_2$ is the concentration of calcium in the second compartment, and X is the number fraction of open channels. X is calculated from

$$\frac{dX}{dt} = -\frac{1}{\tau_{store}} \left[X - (RA) Re([Ca]_2) \right] \tag{2.24}$$

where RA is the probability of receptor–agonist binding and $Re([Ca])$ models the bell–shaped calcium response of the receptors. In these simulations, when the effects of intracellular Ca^{2+} release was thought to occur, RA was set equal to 1. This is equivalent to assuming the receptors are saturated by agonist molecules. The following functional

form was used for Re:

$$Re([Ca]) = \begin{cases} 0, & [Ca] < [Ca]_\theta, \\ \nu([Ca]) \exp\left[1 - \nu([Ca])\right], & [Ca] > [Ca]_\theta, \end{cases} \tag{2.25}$$

$$\nu([Ca]) = \frac{[Ca] - [Ca]_\theta}{[Ca]_{max} - [Ca]_\theta}. \tag{2.26}$$

The form of the above equation is an α–function (i.e. it has the form $c\alpha e^{\frac{-t}{\alpha}}$ for $t > 0$, and 0 otherwise) which attains a maximum of 1 at $[Ca] = [Ca]_{max}$. In the simulations, $[Ca]_\theta$ was chosen to be 150 nM as it is thought that there is little CICR release when $[\mathrm{Ca}^{2+}]_i$ is less than 150 nm. Thus the intracellular stores only will act as a source so long as $[Ca]_2$ is above 150 nM.

If RA was set equal to zero, it was found that previous models could not sustain high calcium concentrations for longer than 100 ms after the end of the stimulus. If we refer back to the analysis done on linearizing calcium dynamics, we can see this is a result of the extremely small value of the chemical time constant. This is where intracellular Ca^{2+} stores come into the picture. If four pulses are applied at 100 Hz with $Nspine = 30$ and $RA = 1$, it was found that $[\mathrm{Ca}^{2+}]_{sp}$ could be kept above 400 nM for longer than 1 s. Because of the steep drop–off in $Re([Ca])$ for $[Ca] > 250$ nM, it was found that there was minimal involvement of intracellular stores until $[Ca]_2 \approx 400$ nM. The intracellular stores are able to maintain this concentration by compensating for the loss of calcium through pumps and diffusion if there is enough calcium present in the store, and if ρX (see (2.23)) is large enough. If ρ or X is reduced by a factor of 10, then it is not possible to sustain elevated $[\mathrm{Ca}^{2+}]_{sp}$ under any stimulation protocols. If, however, ρ and X are large enough, the drop–off in $[Ca]_{store}$ is nearly linear in time from the time it begins until the time it ends, resulting in a quasi–steady-state in which $[\mathrm{Ca}^{2+}]_{sp}$ is elevated for over 1 s after the end of the stimulation at a near constant value. The key factor that controls whether a spine is in the high X range is receptor–agonist binding which can be thought of as a function of IP_3 concentration. Thus, if a stimulus is large enough to result

in significant IP_3 release, it is expected that $[Ca^{2+}]_{sp}$ may be elevated for a significant amount of time. Otherwise, $[Ca^{2+}]_{sp}$ will decay quickly as the value of ρX will be too small to compensate for the loss of calcium through diffusion and pumps.

This model nicely builds a mechanism showing how intracellular calcium stores can explain the results of the diazo–4 experiment where the previous models fail, and it also helps explain the importance of IP_3 in LTP. Unfortunately, there is evidence suggesting that there are other calcium stores of importance in LTP, and that the biochemical cascade involved may be a bit more complicated than initially thought. It turns out that protein kinases (PKs), and protein phosphatases (PPs) may be quite important in LTP induction.

2.8 Protein Kinases and Phosphatases in LTP

As mentioned previously, there is ample evidence for the existence of L–type VGCCs in dendritic spines. However, typically it has been found that depolarization pulses alone could not induce LTP. Some suggested that this may be due to an inability to create the appropriate increase in $[Ca^{2+}]_i$, although it has been found that most of the increase in $[Ca^{2+}]_i$ during synaptic activity is due to VGCCs [72]. However, depolarization pulses coupled to LFS (2 Hz stimulation) which did not act through an increase in Ca^{2+} influx could result in the induction of LTP [54]. This suggests that some aspect of glutamate release may be important in inducing LTP. Three immediate candidates for this effect are NMDARs, mGluR5, and a possible priming effect that action potentials have on the presynaptic cell. The problem with NMDARs as the candidate is that bath application of NMDA is capable of creating large Ca^{2+} transients, but they only can induce STP and not LTP [12] (although, see [108]). The problem with the priming hypothesis is that postsynaptic glutamate iontophoresis is capable of inducing LTP [22]. Thus the most likely stimuli required for the induction of LTP is some combination of a sufficiently

large increase in $[Ca^{2+}]_i$ and the activation of mGluR5.

Since a local, transient increase in $[Ca^{2+}]_i$ itself was never seriously expected to be the ultimate end of the biochemical cascade which results in LTP, the next question becomes what is? That is, there may be a number of biochemical cascades involved which all have one common endpoint — the activation of some critical molecule or biochemical process that once initiated results in a persistent increase in synaptic efficacy. It turns out there is such a candidate molecule, Ca^{2+}–CaM dependent protein kinase II (CaMKII) (for a review of this remarkable enzyme see [16]).

A Brief Introduction to CaMKII

CaMKII is a holoenzyme composed of 8-12 basically identical monomers. Each monomer possesses a catalytic site, a regulatory domain, and a site which allows it to bind to other monomers. Monomers are typically inhibited by their regulatory domain, but this inhibition is relieved when Ca_4^{2+} – CaM binds to the regulatory domain. In its Ca_4^{2+} – CaM bound state, each monomer has a very broad substrate specificity allowing it to regulate such diverse processes as carbohydrate metabolism, neurotransmitter release and resynthesis, cytoskeletal function, and ion flux [98]. Interestingly, CaMKII is the most common Ca^{2+}–dependent PK, comprising $\approx$ 1% of total protein in the brain, and $\approx$ 2% of total protein in the hippocampus, and 30–40% of the total protein in the PSD. Given its high concentration in the PSD and hippocampus, it is not surprising that it is suspected of playing a major role in governing synaptic plasticity.

CaMKII has a unique set of attributes that allow it to respond to the distinctive properties of calcium signals which usually occur over a narrow range of concentrations, and are transient and pulsatile in nature rather than smooth and continuous. CaMKII handles such signals elegantly due to its multiple activity levels which are dependent not only on its monomers Ca_4^{2+} – CaM bound, but also their phosphorylation state. The

CaMKII subunits are involved in autophosphorylation reactions [71] – one subunit in its Ca_4^{2+} – CaM bound state can phosphorylate a neighbor in the same state [34]. This phosphorylation has the effect of trapping Ca_4^{2+} – CaM to a monomer through a dramatic decrease in the off–rate of Ca_4^{2+} – CaM binding. Since there is very little effect on the on–rate of binding, this results in a dramatic increase in the monomer's affinity for CaM – the K_d goes from $\approx 45\,\text{nM}$ to $\approx 60\,\text{pM}$, one of the highest known affinities for CaM [16]. While Ca_4^{2+} – CaM typically dissociates from a monomer within a half–second, in its phosphorylated state, the typical dissociation time is on the order of hundreds of seconds. In this Ca_4^{2+} – CaM bound, phosphorylated state, the monomer maintains 100% of its catalytic activity. Even after the Ca_4^{2+} – CaM dissociates from the monomer, so long as the monomer is phosphorylated, it maintains 20–80% of its catalytic activity. Now it can be seen how the CaMKII molecule can decode calcium signals. If a Ca^{2+} signal is arriving with a certain frequency, a certain number of subunits per holoenzyme are going to bind Ca_4^{2+} – CaM . If two proximal subunits become activated, they may become involved in an autophosphorylation reaction which traps the Ca_4^{2+} – CaM and leads to a potentiation of the calcium signal. If the frequency is low, the Ca_4^{2+} – CaM would escape before the next spike (this can happen because there are phosphatases which also are activated by Ca_4^{2+} – CaM which dephosphorylate the subunits), but if the frequency is high, then there is the possibility of even more subunits becoming activated with each new spike. "This cooperativity of calmodulin trapping may allow the kinase to be a frequency detector with a threshold frequency beyond which it becomes highly active" [16].

A Model of CaMKII Dynamics

Using some estimates of experimental parameters [68], Michelson and Schulman [69] developed a model for the activation and transition between different activity states of a ten subunit CaMKII molecule.

The j^{th} subunit, S_j, had five activation states: inhibited, S_j^I, Ca_4^{2+} – CaM bound, S_j^B,

Ca_4^{2+} – CaM trapped, S_j^T, autonomous, S_j^A, and capped, S_j^C. In the capped state, it is phosphorylated at an additional site compared to the autonomous and trapped states. Once a subunit is bound to Ca_4^{2+} – CaM , it can traverse the trapped, autonomous, and capped states. The transitions between these states were a function of the Ca_4^{2+} – CaM concentration and the activation state of its right–hand neighbor.

If we let S_{j+1}^X denote the activation state of the right–hand neighbor, the following transition matrix describes the probability of transfer between the various activation states:

$$\begin{bmatrix} p_{II}([Ca_4CaM]) & p_{IB}([Ca_4CaM]) & 0 & 0 & 0 \\ p_{BI}([Ca_4CaM], S_{j+1}^X) & p_{BB}([Ca_4CaM], S_{j+1}^X) & p_{BT}([Ca_4CaM], S_{j+1}^X) & 0 & 0 \\ 0 & p_{TB}([Ca_4CaM], S_{j+1}^X) & p_{TT}([Ca_4CaM], S_{j+1}^X) & p_{TA}([Ca_4CaM], S_{j+1}^X) & 0 \\ p_{AI}([Ca_4CaM], S_{j+1}^X) & 0 & p_{AT}([Ca_4CaM], S_{j+1}^X) & p_{AA}([Ca_4CaM], S_{j+1}^X) & p_{AC}([Ca_4CaM], S_{j+1}^X) \\ 0 & 0 & 0 & p_{CA}([Ca_4CaM], S_{j+1}^X) & p_{CC}([Ca_4CaM], S_{j+1}^X) \end{bmatrix}$$

where the nonzero entries in each row are non–negative and sum to 1.

The method used to solve the problem was Monte Carlo simulation. The transition probabilities were based on half–life estimates of the various activity states from experimental data [68]. It was assumed that the transition state probabilities could be fitted to an exponential distribution.

The results of simulations suggest that the trapped state of the subunits can act as a "capacitance" that allows for significant temporal summation even at low frequencies. In fact, a single 1μM Ca_4^{2+} – CaM spike was capable of increasing the activity of CaMKII for minutes following the stimulation. Another observation from the application of sinusoidal Ca_4^{2+} – CaM transients is that while the proportion of subunits in inhibited, bound and trapped state is sinusoidal, the proportion in the autonomous and capped state do not and thus appear to be acting capacitively.

CaMKII and LTP

The idea of CaMKII acting as a frequency detector of high frequency calcium signals, coupled to its high concentration in the hippocampus and PSD immediately suggests that it may be very important in LTP induction. This has been recognized and a very prominent theory in the field has been put forward suggesting that the activation of CaMKII is not only necessary and sufficient for the induction of LTP but may actually be the genesis of LTP and LTD expression [57, 60, 58, 59]. The basic idea is that low levels of $[Ca^{2+}]_i$ which are thought to be involved in LTD induction may preferentially activate protein phosphatases which will dephosphorylate CaMKII subunits and result in a decrease in synaptic efficacy. However, a large increase in $[Ca^{2+}]_i$ will directly lead to the phosphorylation of CaMKII and the resulting increase in CaMKII activity will lead to an increase in synaptic efficacy. In between synaptic weight change episodes, the level of phosphorylation of CaMKII will be set by the competing reactions of dephosphorylation by protein phosphatases and autophosphorylation within CaMKII holoenzymes. In support of this theory, it has been found that postsynaptic injection of $Ca_4^{2+} - CaM$ can lead to the induction of LTP [112], while postsynaptic injection of CaM inhibitors [62] or CaMKII inhibitors [62, 65] can block LTP induction. Furthermore, evidence for the long–term activation of CaMKII following LTP induction has been found [26]. An interesting question now becomes how might CaMKII increase synaptic efficacy. One possibility that has been suggested is that CaMKII directly phosphorylates synaptic glutamate receptors and results in an increase in conductance. In this light, it has been shown that several glutamate receptor subunits have consensus phosphorylation sites for CaMKII [67]. Furthermore, CaMKII can phosphorylate and increase the current through kainate receptors (this is a type of non–NMDAR which is quite similar to the AMPAR) three– to four–fold *in vitro*. A corollary to this CaMKII hypothesis for LTP should be that if CaMKII already is maximally activated or cannot be activated at all, then it should be

impossible to induce LTP. This is, in fact, observed. Transgenic mice without genes for CaMKII are incapable of undergoing LTP [30], and when a constitutively active CaMKII was introduced into hippocampal slices, it resulted in an increase in synaptic efficacy but prevented further induction of LTP [85].

Now the hypothesis that increased receptor conductance leads to an increase in synaptic efficacy seems intuitively obvious, but one has to remember that efficacy here refers to the ability of presynaptic activity to result in action potential generation at the axon hillock. In fact, it has been show that under certain circumstances this may not be true [117]. This will be dealt with in more detail when I review results from electrical modeling of spines later.

Now there is one last question which I should delve into before finishing the LTP portion of this thesis. Is an increase in $[Ca^{2+}]_i$ under normal physiological conditions sufficient for the induction of LTP?

2.8.1 The role of PKC and sufficiency of Ca^{2+} in LTP induction

The question of the sufficiency of increases in $[Ca^{2+}]_i$ in LTP is very contentious. The first of many positive results came from experiments with a calcium chelator, nitr–5, which releases Ca^{2+} upon exposure to light [63]. However, many different experimental results have been found, and there is no clear consensus. One interesting experiment alluded to earlier [112] found that postsynaptic injection of Ca^{2+} or CaM alone could not induce LTP while the injection of a calcium/CaM mixture could in a manner that was inhibited by CaMKII and PKC inhibitors. The role of CaMKII in LTP was discussed previously and will not be discussed again. PKC was mentioned previously as a PK which is activated by DAG which is produced during mGluR5 activation (along with IP_3). It has been a fairly consistent observation that PKC is activated during LTP induction [51], and its inhibition prevents LTP induction [3, 111, 91].

The link between PKC activation and CaMKII activation is not immediate as neither has any direct effect on the other. However, it has been discovered that PKC phosphorylates a protein, RC3 (also called neurogranin), found in high concentration in dendritic spines [113]. RC3 is a calmodulin–binding protein which decreases its affinity for CaM when it is phosphorylated [28]. It has been shown that RC3 can modulate calmodulin availability and decrease the activity of Ca_4^{2+} – CaM–dependent enzymes [66]. For example, in the presence of 1μM of RC3 (a more physiological concentration is 2μM), 10μM of Ca^{2+} was required to achieve half–maximal velocity of nitrous oxide synthase (NOS), a $Ca_4^{2+}-$CaM-dependent enzyme. Only $.55\mu$M of Ca^{2+} was required in the absence of RC3. It was found that inclusion of activated PKC could prevent the RC3–mediated inhibition of NOS. This effect could be negated by inclusion of alkaline phosphatase which dephosphorylates RC3. This is of some interest since RC3 is dephosphorylated by PP1 and calcineurin, both of which are found in dendritic spines [102]. The specific link between RC3 and LTP comes from an experiment in which it was found that antibodies to RC3 which inhibit its PKC–mediated phosphorylation could prevent the induction of LTP [25]. One possible reason for this effect may have been due to some effect on CaM availability. Some have suggested that "RC3 is a biochemical 'capacitor' in that it transduces Ca^{2+} fluxes into kinetic parameters affecting the availability of Ca^{2+}/CaM and the rapidity with which it is made accessible to other enzymes" [28]. Thus, RC3 may be acting as a PKC–mediated CaM store, and this is the connection between PKC and CaMKII activation. However, there is some evidence suggesting a role for phosphorylated RC3 in mobilizing of intracellular Ca^{2+} stores in *Xenopus* oocytes [21].

2.9 Concluding remarks about LTP

What exactly LTP is at this moment is not at all clear, but there seems to be a very strong connection between it and dendritic spines. The connections between LTP and

learning/memory are less clear. The only solid connection between LTP and learning appears to be that mechanisms which reduce the capacity for LTP induction seem to impair spatial memory in rats. This is consistent with the hippocampus being very important in spatial memory. Otherwise, there seems to be little effect for the most part. One has to be a bit cautious because here LTP means LTP induced at the Schaffer collaterals in the stratum radiatum of CA1 hippocampal pyramidal neurons. Thus, LTP induction may be dependent on similar but slightly different mechanisms elsewhere in the CNS. On the other hand, the local learning memory paradigm may not be the way most memories are stored in the CNS. This should not denigrate, however, the work that has been done in this field. LTP is a very robust memory phenomena which may provide insights into the way in which memories are encoded in the CNS, and this is why it is so extensively studied. Moreover, LTP offers an excellent example of theoreticians and experimentalists working side–by–side in deciphering the riddle of biological complexity.

Chapter 3
Electrical Modeling of Spines

3.1 Introduction

While intracellular Ca^{2+} dynamics are difficult to quantify, the cable model for voltage, and the parameters which describe it, are known with much more certainty. Thus, we stand on much firmer ground when we try to obtain insights into the electrical nature of spines than when we try to understand their Ca^{2+} dynamics. The first notion of the possible electrical implications of spine necks was made by Chang in 1952 [19]:

> "If the end bulbs of the gemmules (spines) are the receptive apparatus for the presynaptic impulses, the process of postsynaptic excitation initiated there must be greatly attenuated during its passage through the stems of the gemmules (spine necks) which probably offer considerable ohmic resistance because of their extreme slenderness."

Since then, a number of theories have been put forward to explain the electrical nature of spines. I now will review a few of the major ideas.

3.2 Spines mediate synaptic potential attenuation

As mentioned above, Chang made this proposition in 1952 and explained its functionality by requiring that a number of synapses be coactive to bring a cell to threshold for action potential (AP) generation. From cable theory estimates, one expects the most important

determinant of this phenomena to be spine neck resistance since the spine membrane resistance is large enough to be assumed to be infinite owing to the extremely small surface area of spines. It turns out that because of the extremely short lengths of spine necks (on the order of 1 μm), there is likely to be very little current attenuation across the spine stem (this will be elaborated upon later). However, because the spine input resistance is expected to be much larger than the dendritic input resistance, the spine should be able to mediate a much larger local EPSP than the same current input into the parent dendrite.

An important point which will be made here is the asymmetry in the cable equation. While a synaptic event will produce a large voltage gradient between spine head and the parent dendrite, there will be little voltage difference between the dendritic shaft and neighboring, inactive spines [88]. The large, local EPSP generated in spine heads has implications in terms of the activation of NMDARs, which may be important in LTP, and voltage–gated channels, which may allow for a type of pseudo–saltatory conduction within dendrites (this will be discussed later). Thus, as Shepherd pointed out [105]:

> " ... a spine is a sensitive detector of its own synaptic input, but it follows closely with neighboring spines the integrated potential of its parent dendrite; from this perspective, it is both a detector and an integrator."

3.3 Spines allow for linear summation of EPSPs

One idea put forward was that the attenuation across a spine neck will keep spines isolated from each other and allow linear EPSP summation. This is a consequence of the nature of the current inputs which are proportional to the difference between the transmembrane potential and the reversal potential of the channel which can be considered to be a constant under most normal, physiological conditions (however, see [86]). However, one aspect to be pointed out is that the time course of an EPSP in a spine is expected to

be much shorter than an equivalent one on the parent dendrite. This narrows the time frame over which non–linear interactions between neighboring spines can occur, and this can have important implications when nonlinear spine dynamics are considered. One thing that should be mentioned is that the time course of the EPSP as observed in the dendrite and soma is fundamentally the same whether the synapse is on the spine or the dendrite because the higher capacitance of the dendrite and soma cause them to function as low–pass filters. However, the spine is not so constrained.

3.4 Spine neck resistance as controller of synaptic weight

One idea that has frequently been put forth is that a spine is ideally situated to be a compartment for controlling the strength of an individual synapse. Since changes in spine morphology and density have been correlated with memory [105, 35], this idea does have some merit.

Wilfrid Rall showed the conditions under which a mechanism controlling spine stem length could be prominent [90]. His analysis was under steady state assumptions, but the fundamental underlying idea applies to transient currents as well. He demonstrated that the amount of current that reaches the parent dendrite when injected into the spine head is most malleable when the resistance of the spine neck is approximately equal to the input resistance of the infinite dendrite.

It is a fairly typical observation that spines with the longest and thinnest necks tend to be located on thin distal dendrites. Thus, the thinking was that there is some sort of an impedance matching between R_N and $R_{\infty,d}$ which allows features of the spine neck to control synaptic efficacy. However, the bulk of evidence suggests that typically $R_N \ll R_{\infty,d}$ [107].

3.5 Spines attenuate transient synaptic input

The fundamental ideas of Rall's work led people to delve into the possibility that synaptic events in spines may push the spine membrane potential towards the synaptic reversal potential due to the high input resistance of spines. This notion was a fundamental one in the field for many years with no clear consensus. However, in the early 1980s, several groups came forward with a formal mathematical analysis of the problem [116, 49, 50, 52]. All suggested that there should be little attenuation of current across the spine neck, although it was accepted that there was a range of geometrical and electrical parameters over which local spine EPSPs could push the potential towards the synaptic receptor reversal potential and result in voltage saturation. Koch and Zador [53] showed there is insignificant attenuation of transient synaptic input if the product of the synaptic conductance and input resistance of the spine head is much smaller than one. In this case, the spine could be said to represent a current source of amplitude $g_{syn}(V_{syn} - V_{sp})$ where g_{syn} is the synaptic conductance, V_{syn} is the synaptic reversal potential, and V_{sp} is the spine head potential. Conversely, if $g_{syn}R_{infty} \ll 1$, then the action of a synapse can be seen as a voltage source causing the dendritic EPSP to approach $\frac{R_{\infty,d}V_{syn}}{R_{\infty,d}+R_N}$.

The earlier conclusions that there would be significant attenuation were based on a poor understanding of the electrophysiology of spines and were based on channel densities of squid axons. With more reasonable, physiological estimates, it seems as though $g_{syn}R_{\infty,sp} \ll 1$ for most spines. Thus spines act primarily as current sources and moving a synaptic connection from the spine head to the dendritic shaft would not appreciably change the depolarization achieved within the dendrite or within the soma. Let us now look at some other theories of spines and leave this idea behind.

3.6 Spines increase the low–pass filtering capacity of neurons

One feature of spines that has not been addressed much so far is the idea that spines will increase the surface area of dendrites. Thus, spines would be expected to have a reduced membrane resistance, and an increased capacitance. This will have the net effect of decreasing the electrotonic length and input resistance, while having little effect on the time constant [46] (see below for an analytical justification). This will drastically reduce spatial summation and will amplify the low–pass filtering capacities of dendrites. This effect has been noticed in the torus semicircularis of the weakly electric fish, *Eigenmannia* [95, 96]. It was noticed that the amplitude envelope of a stimulus ($2 - 20\,\mathrm{Hz}$) was nicely reflected in the fluctuations of heavily spined neurons, but not in sparsely spined or aspiny neurons of otherwise similar morphology. This has implications in minimizing the jamming of *Eigenmannia's* electrolocation capabilities by electrical discharges from other nearby electrical fish.

3.7 The effect of passive spines on the cable properties of dendrites

The intuitive notions of spines not affecting membrane time constant while decreasing the electrotonic length and input resistance of dendrites should be quantifiable. The nature of spines is such that compartmental models and numerical simulations are required to represent their discrete nature. However, Baer and Rinzel [5] developed an idea for simplifying the situation for the case of a relatively spiny dendrite with identical spines. Instead of modeling each spine individually, just view them as having a certain density, $\bar{\rho}$. The spines are not connected to each other directly electrically, but are coupled indirectly via the parent dendrite. Thus we can come up with a modified cable equation for passive spines in a passive dendritic tree as follows (see the table in Section 2.3 for some of the

symbols)

$$C_{sp}\frac{V_{sp}}{\partial t} = -\frac{V_{sp}}{R_{m,sp}} - I_N, \tag{3.1}$$

$$2\pi r_d C_m \frac{\partial V_d}{\partial t} = \frac{\pi r_d^2}{R_i}\frac{\partial^2 V_d}{\partial x^2} - \frac{\pi r_d}{R_m}V_d + \rho I_N, \tag{3.2}$$

$$I_N = \frac{V_{sp} - V_d}{R_N}, \tag{3.3}$$

where V_{sp} and V_d are the membrane potentials of the spine and the dendrite, respectively, C_{sp} is the specific capacitance of the spine, $R_{m,sp}$ is the specific membrane resistance of the spine, I_N is the resistive current flowing between the spine head and the dendrite, and ρ is a proportionality factor. If we multiply (3.1) by $R_{m,sp}$ and (3.2) by $\frac{R_m}{2\pi r_d}$ and make the substitutions

$$\tau = R_m C_m, \tag{3.4}$$

$$\lambda = \sqrt{\frac{r_d R_m}{2R_i}}, \tag{3.5}$$

$$T = \frac{t}{\tau}, \tag{3.6}$$

$$X = \frac{x}{\lambda}, \tag{3.7}$$

we get

$$\frac{R_{m,sp}C_{sp}}{\tau}\frac{\partial V_{sp}}{\partial T} = -V_{sp} - R_{m,sp}I_N, \tag{3.8}$$

$$\frac{\partial V_d}{\partial T} = \frac{\partial^2 V_d}{\partial X^2} - V_d + \frac{\rho R_m}{2\pi r_d}I_N. \tag{3.9}$$

If we multiply and divide the term containing I_N in (3.9) by λ, recognize that $R_{\infty,d} = \frac{R_m}{2\pi r_d \lambda}$, and let $\rho = \lambda\bar{\rho}$, which is a measure of spine density per electrotonic length, then we get

$$\frac{\partial V_d}{\partial T} = \frac{\partial^2 V_d}{\partial x^2} - V_d + \rho R_{\infty,d} I_N. \tag{3.10}$$

Now, we can make use of physiological estimates of the parameters to reduce the problem further. Typically, we expect $R_{m,sp} \gg R_N$, and $R_{\infty,d} \gg R_N$, and $V_{sp} \approx V_d$. Let us

introduce a small parameter, $\epsilon = \frac{R_N}{R_{m,sp}}$, and expand V_{sp} as

$$V_{sp} = V_d + \epsilon V_{sp,1} + \epsilon^2 V_{sp,2} \ldots \tag{3.11}$$

If we substitute the above equation into (3.8) and (3.10), and only retain $O(1)$ terms in ϵ, we get

$$\frac{R_{m,sp}C_{sp}}{\tau}\frac{\partial V_d}{\partial T} = -V_d - V_{sp,1}, \tag{3.12}$$

$$\frac{\partial V_d}{\partial T} = \frac{\partial^2 V_d}{\partial X^2} - V_d + \frac{\rho R_{\infty,d}}{R_{m,sp}} V_{sp,1}. \tag{3.13}$$

If we solve (3.12) for $V_{sp,1}$, substitute it into (3.13), and rearrange the terms, we obtain

$$\left(1 + \frac{\rho R_{\infty,d}}{R_{m,sp}}\frac{R_{m,sp}C_{sp}}{\tau}\right)\frac{\partial V_d}{\partial T} = \frac{\partial^2 V_d}{\partial X^2} - \left(1 + \frac{\rho R_{\infty,d}}{R_{m,sp}}\right) V_d. \tag{3.14}$$

Now by analogy with the cable equation, the appropriate thing to do here is to multiply both sides of the equation by $\left(1 + \frac{\rho R_{\infty,d}}{R_{m,sp}}\right)^{-1}$ to get

$$\tau_s \frac{\partial V_d}{\partial T} = \lambda_s^2 \frac{\partial^2 V_d}{\partial X^2} - V_d, \tag{3.15}$$

$$\tau_s = \frac{1 + \frac{\rho R_{\infty,d}}{R_{m,sp}}\frac{R_{m,sp}C_{sp}}{\tau}}{1 + \frac{\rho R_{\infty,d}}{R_{m,sp}}}, \tag{3.16}$$

$$\lambda_s = \left(1 + \frac{\rho R_{\infty,d}}{R_{m,sp}}\right)^{-\frac{1}{2}}. \tag{3.17}$$

Now notice that if $\frac{R_{m,sp}C_{sp}}{\tau} > 1$, we have $\tau_s > 1$, and the effective time constant is larger than the time constant of an equivalent nonspiny dendrite. The opposite is true if $\frac{R_{m,sp}C_{sp}}{\tau} < 1$. Under reasonable physiological assumptions, we expect $\frac{R_{m,sp}C_{sp}}{\tau} \approx 1$ in agreement with the results of Jaslove [46]. However, notice that $\lambda_s < 1$, and thus there always will be a decrease in effective electrotonic length. Furthermore, the same also is expected to be true of the effective input resistance since it is proportional to the effective electrotonic length, i.e.,

$$R_{\infty,d_{eff}} = R_{\infty,d}\lambda_s. \tag{3.18}$$

The unfortunate thing about the above analysis is that it does not show how electrotonic length and input resistance change with R_N. We only have done a leading-order approximation which neglects the effects of R_N under the presumed physiological conditions. However, the certainty with which these predictions can be made must be tentative since no direct measurements from spines have been made. The spine cytoplasm looks quite different from the dendritic cytoplasm and might have a different value of R_i (probably bigger). Spines contain spine apparati, SER, and occasionally mitochondria which should act to increase R_N by an uncertain amount. To clear up this issue, we look at a steady state model. This should not effect the length constant or the input resistance. The equations now become

$$0 = -\frac{V_{sp}}{R_{m,sp}} - I_N, \tag{3.19}$$

$$0 = \lambda^2 \frac{\partial^2 V_d}{\partial X^2} - V_d + \rho R_{\infty,d} I_N. \tag{3.20}$$

We can solve (3.19) for V_{sp} to obtain

$$V_{sp} = \frac{V_d R_{m,sp}}{R_{m,sp} + R_N}. \tag{3.21}$$

Substituting (3.21) into (3.20), we obtain

$$\lambda^2 \frac{\partial^2 V_d}{\partial X^2} - \left[1 + \frac{\rho R_{\infty,d}}{R_N + R_{m,sp}}\right] V_d = 0. \tag{3.22}$$

This yields an effective space constant, λ^{eff}, and effective input resistance, $R^{eff}_{\infty,d}$, of

$$\lambda^{eff} = \frac{\lambda}{\sqrt{1 + \frac{\rho R_{\infty,d}}{R_N + R_{m,sp}}}}, \tag{3.23}$$

$$R^{eff}_{\infty,d} = R_{\infty,d} \frac{\lambda_{eff}}{\lambda}. \tag{3.24}$$

Thus, we immediately can see that increasing R_N has the effect of increasing λ^{eff} and $R^{eff}_{\infty,d}$. This can be reasoned as a result of increasing isolation between spine and shaft and decreasing the conductance load of the spines on the dendrite. Notice that for $R_{m,sp} \gg R_N$, we recover the leading-order multiplicative corrector to λ, λ_s, derived earlier.

3.8 Computational richness of active dendritic spines

Now that we have seen the effects of passive dendritic spines on the cable equation, the next obvious question is: what is the effect of active conductances in dendritic spines? Investigations into the implications of active conductances in dendritic spines began in 1985 with the publication of three papers on the subject [70, 82, 106].

Miller et al. [70] looked into the effects of letting the value of the spine neck resistance depend on the amplitude of the EPSP in the dendritic shaft. They found that the peak dendritic EPSP to a synaptic input was a bell–shaped function of the spine–neck resistance *ceteris paribus* when the active conductances were sufficiently large. Intuitively, one expects that as neck resistance initially is increased from low values, this increases the input resistance of the spine and results in an increase in the spine EPSP. This recruits more and more active channels to open and increases the current output to the dendrite and results in a larger dendritic EPSP. Eventually, at some critical value of spine neck resistance, there should be an action potential in the spine head and a nonlinear increase in dendritic EPSP. As the spine neck resistance continues to increase, the high spine neck resistance will eventually cause a very quick voltage saturation in the spine head as the spine head potential approaches the reversal potential of the active channels. Increasing R_N further has little effect on the voltage–time integral and only serves to decrease I_N and the resulting dendritic EPSP. This is the principal driving force for current through the spine neck which is the cause of the dendritic EPSP [87]. Thus active spines confer an even greater dependence of synaptic efficacy on spine neck resistance than was first implicated by Rall in 1974 [90] (for the appropriate parameter ranges). These results were confirmed by Perkel and Perkel [82], who also showed that in order to get the bell–shaped curve of dendritic EPSP vs. spine neck resistance:

1. The ratio of peak active conductance to peak synaptic conductance had to be sufficiently high (larger than 1).

2. The dendritic input resistance had to sufficiently small, i.e., for high enough dendritic input resistance, the dendritic EPSP is essentially a monotonically decreasing function of spine neck resistance.

A thorough investigation into this problem was made by Rall and Segev in the late 1980s [87]. They suggested that the key to the attainment of threshold for an excitable dendritic spine is

$$I_{active} > I_N - I_{syn} \quad \text{when} \quad V_{sp} = V_{th} \tag{3.25}$$

where I_{active} is the current through active channels, I_{syn} is the synaptic current, and V_{th} is the threshold voltage where net inward current generated at the spine head is greater than the net outward current into the passive dendrite. Thus, the early active current must exceed the difference between the current though the neck and the synaptic current. They concluded that increasing R_N decreases the voltage threshold because

1. Increasing spine neck resistance increases the spine input resistance and results in steeper spine EPSPs.

2. I_N is a monotonically decreasing function of R_N increasing the likelihood that the inequality (3.25) is satisfied.

3. Increasing R_N decreases the conductance loading of the spine head membrane.

The effects of increasing active channel densities in active spines also was investigated. In general, it was found that increasing the density of active channels eventually led to a quick saturation of the voltage in the spine head. However, here the dendritic EPSP was a monotonic function which plateaued at some finite value since I_N is inversely proportional to R_N but independent of the channel density.

Rall and Segev went on to address the significance of placing active channels in spines versus on the dendrites. They suggested that to optimize synaptic efficacy, active membrane channels should be divided into spines such that each has just the right density

of channels to fire action potentials. This is preferred to equally spreading them over the dendrite since the smaller dendritic input resistance would make it more difficult to achieve threshold. Furthermore, the precise synchronous timing of inputs is very crucial to possible nonlinear interactions when dendrites contain active spines. For example, a single synaptic event which is insufficient to result in an active spine firing an action potential, could be sufficient if the dendrite is depolarized from activity at neighboring spines. This is a result of the decreased value of I_N due to the larger value of V_d in inequality (3.25). The possibility of precise timing is strengthened even further for those spines which appear to receive input from both an inhibitory presynaptic terminal and an excitatory presynaptic terminal. Here, conjunction of presynaptic and postsynaptic inputs within a narrow time window could prevent action potential generation and result in a nonlinear decrease in dendritic EPSP.

3.9 Pseudosaltatory conduction in dendritic spines

While it seems as though more attention was paid to R_N than $R_{\infty,d}$ in the above simulations, this is because they tended to focus on the implications of a single excitable spine in isolation from its neighbours. One question that arises naturally is whether or not active spines can mediate action potentials which regeneratively travel down dendrites. Since the active channels would only be in discrete locations in the spine head along the dendrite, the situation is somewhat analogous to saltatory conduction in myelinated axons. Here, we expect that a high dendritic input resistance is essential to ensure that a dendritic EPSP stays above V_{th} as suggested by Rall. The possibility of pseudosaltatory conduction in excitable spines was first simulated by Shepherd et al. in 1985 for spiny, distal dendrites in pyramidal neurons of the cerebral cortex [106]. Their initial results suggested that such dendritic action potentials were possible with Hodgkin–Huxley type kinetics in the spine heads if:

1. active channel densities were large enough,
2. the α_m constant was sufficiently large,
3. spine neck resistance was within a certain range,
4. dendritic radius was sufficiently small (this is correlated with a large space constant and dendritic input resistance, both of which aid in action potential generation), and
5. active propagation past branch points depended on activity in sister branches.

They suggested such a mechanism could allow for large increases in the efficacy of distal dendritic inputs, and allow for much quicker propagation of information to the soma instead of the classical result that distal dendritic inputs only can have a slow, small modulatory effect on the somatic potential. Furthermore, the propagation of an impulse often required several near–synchronous, spatially localized inputs and could greatly increase the complexity of information processing that can take place in dendrites. The action of a set of inputs now not only depends on the size of the depolarization it can elicit at the axon hillock, but also depends on its spatio–temporal coactivation patterns with its neighbours. Rall and Segev showed a similar result for excitable spine clusters [88], that is, for dendrites in which there are passive and active spines, but with the active spines located in close proximity with each other.

Motivation of the spine continuum model

Once the notions of significant synaptic attenuation across spine necks had been put to rest, more interest began to develop about the possible implications of excitable spine membranes. From some of the major papers that had been written in this field over the past few years, the issue of the significance of dendritic spines is not yet clear. However, over the past few years, the paradigm has shifted to spines being mediators of biochemical

specificity of synapses (i.e. their role in LTP) rather than electrical modulators of synaptic activity. The possibility of active membranes in spines is a fascinating one, both in terms of the possible generation of mathematical richness in the model equations, and its capacity for fundamentally altering the way in which the effects of distal dendritic inputs are viewed. However, the problem is plagued with analytical intractability in its present form — the computational modeling of active membrane channels within spines yields results which make intuitive sense, but we seem to lack an understanding of how the parameters work together to elicit the propagation of these dendritic action potentials. The problem has to do with the discrete nature of spines. This is where the ideas of averaging and switching to functional forms which retain enough of the qualitative spirit of the model, but allow for more analytical methods of investigation, become critical in yielding new insights into the problem.

One approach to the problem mathematically would be to follow in the lines of Bell and Cosner [8] and treat the spines as identical point sources of current which are evenly, but discretely distributed on the dendrite. Another would be to try the method analogous to the one previously used to derive the effects of passive spines on the electrotonic properties of passive dendrites. This continuum approach was used by Baer and Rinzel to numerically investigate the propagation of dendritic action potentials mediated by active spines in 1991 [5]. Their approach was to have a passive, homogeneous, infinite dendrite attached to a certain density of spines as explained earlier. Here, however, the spines contained synaptic conductances and Hodgkin–Huxley type dynamics. Baer and Rinzel indicated that their simulations suggested that while the placement of active channels in the spine head had important implications in terms of threshold for the initiation of traveling pulses (namely, less presynaptic pulses were required for dendrites with active channels in the spines), it was relatively unimportant in the propagation of a pre–existing pulse.

In the next section I will try to modify Baer and Rinzel's equations to make them more analytically tractable.

Derivation of the Model

In the paper written by Baer and Rinzel [5], they added active channels based on Hodgkin–Huxley type kinetics to the spine membrane voltage equation used in the study

of passive spines. As a result, their model equations were

$$2\pi r_d C_m \frac{\partial V_d}{\partial T} = \frac{\pi r_d^2}{R_i}\frac{\partial^2 V_d}{\partial X^2} - \frac{2\pi r_d}{R_m}V_d + \bar{N}(x)I_N, \tag{3.26}$$

$$C_{sp}\frac{\partial V_{sp}}{\partial T} = -I_{act} - I_N - I_{syn}(x,t), \tag{3.27}$$

$$I_N = \frac{V_{sp} - V_d}{R_N}, \tag{3.28}$$

$$I_{act} = \bar{\gamma}A_{sp}(\bar{I}_{Na} + \bar{I}_K + \bar{I}_L), \tag{3.29}$$

$$\bar{I}_{Na} = \bar{g}_{Na}(V_{sp} - V_{Na})m^3, \tag{3.30}$$

$$\bar{I}_K = \bar{g}_K(V_{sp} - V_K)n^4, \tag{3.31}$$

$$\bar{I}_L = g_L(V_{sp} - V_L), \tag{3.32}$$

$$\frac{\partial m}{\partial T} = \frac{m_\infty(V_{sp}) - m}{\tau_m(V_{sp})}, \tag{3.33}$$

$$\frac{\partial h}{\partial T} = \frac{h_\infty(V_{sp}) - h}{\tau_h(V_{sp})}, \tag{3.34}$$

$$\frac{\partial n}{\partial T} = \frac{n_\infty(V_{sp}) - n}{\tau_n(V_{sp})}, \tag{3.35}$$

$$m_\infty(V) = \frac{\alpha_m(V)}{\alpha_m(V) + \beta_m(V)}, \tag{3.36}$$

$$h_\infty(V) = \frac{\alpha_h(V)}{\alpha_h(V) + \beta_h(V)}, \tag{3.37}$$

$$n_\infty(V) = \frac{\alpha_n(V)}{\alpha_n(V) + \beta_n(V)}, \tag{3.38}$$

$$\tau_m(V) = \frac{1}{\alpha_m(V) + \beta_m(V)}, \tag{3.39}$$

$$\tau_h(V) = \frac{1}{\alpha_h(V) + \beta_h(V)}, \tag{3.40}$$

$$\tau_n(V) = \frac{1}{\alpha_n(V) + \beta_n(V)}, \tag{3.41}$$

$$\alpha_m(V) = \frac{25 - V}{10\left(e^{\frac{25-V}{10}} - 1\right)}, \tag{3.42}$$

$$\beta_m(V) = 4e^{-\frac{V}{18}}, \tag{3.43}$$

$$\alpha_h(V) = \frac{7e^{-\frac{V}{20}}}{100}, \tag{3.44}$$

$$\beta_h(V) = \frac{1}{e^{\frac{30-V}{10}} + 1}, \tag{3.45}$$

$$\alpha_n(V) = \frac{10 - V}{100\left(e^{\frac{10-V}{10}} - 1\right)}, \tag{3.46}$$

$$\beta_n(V) = \frac{e^{-\frac{V}{80}}}{8}. \tag{3.47}$$

I_{syn} was modeled as an α function

$$I_{syn}(X,T) = G_{syn}(X,T)(V_{sp} - V_{syn}), \tag{3.48}$$

$$G_{syn}(X,T) = \sum g_{syn}(X, T - T_j), \tag{3.49}$$

$$g_{syn}(x,t) = \begin{cases} 0 & T < 0, \\ \bar{g}_{syn} t e^{1 - \frac{T}{T_{peak}}} & T \geq 0. \end{cases} \tag{3.50}$$

If we multiply both sides of (3.26) by $\frac{R_m}{2\pi r_d}$, multiply the numerator and denominator of I_N by λ where $\lambda = \sqrt{\frac{R_m r_d}{2R_i}}$ is the electrotonic length of the passive dendrite, use the identity $R_{\infty,d} = \frac{R_m}{2\pi r_d \lambda}$ for a semi–infinite dendrite, assume that $\bar{N}(X) = \bar{N}$, and let $\rho = \lambda \bar{N}$, we obtain

$$\tau_m \frac{\partial V_d}{\partial T} = \lambda^2 \frac{\partial^2 V_d}{\partial X^2} - V_d + \frac{\rho R_{\infty,d}}{R_N} (V_{sp} - V_d), \tag{3.51}$$

$$\tau_m = R_m C_m. \tag{3.52}$$

The purpose of studying the system of equations stated thus far was to obtain an understanding of whether it is physiologically plausible for the Hodgkin–Huxley-type dynamics found in squid axons to mediate action potentials in dendrites if they are located within the spine heads. The problem with using the above set of equations is that they are intractable analytically. This is where analogues of models become important. One of the more successful analogues employed for gaining an intuitive understanding of action potentials in squid giant axons is the Fitzhugh–Nagumo equations (for a review see [18]).

The Fitzhugh–Nagumo equations replace the I_{act} term in (3.27) by something more tractable analytically while still maintaining the main features of the dynamics. The simplification which is made is that the time scale of the activation of m, which is what controls the initiation of the pulse, is much faster than the activation of h and n which control the "relaxation" of the pulse. Using this idea, it is possible to reduce $\frac{V_{sp}}{R_{m,sp}} + I_{act}$ from being controlled by three variables, m, h, and n to being controlled by two variables

v and w. Here, v represents voltage, and it is assumed that $m \approx m_\infty(v)$, and that h and n can be combined into one recovery variable, r. The reduction usually takes the form

$$\frac{V_{sp}}{R_{m,sp}} + I_{act} = f(v) + r, \tag{3.53}$$

$$\frac{\partial r}{\partial t} = \frac{r_\infty(v) - r}{\tau_r} \tag{3.54}$$

where τ_r is a constant.

In order to match these functions with experimental data, we define the quantities: $I_p(v)$ which is the transient peak current at voltage v and I_{ss} which is the steady state current at voltage v. More formally,

$$I_p(v) = \lim_{T \to 0^+} I_m(T, v), \tag{3.55}$$

$$I_{ss}(v) = \lim_{T \to \infty} I_m(T, v) \tag{3.56}$$

where $I_m(T, v)$ is the membrane current at time T and voltage v. Thus, we may conclude that

$$f(v) = \frac{I_p(v) + I_{ss}(v)}{2}, \tag{3.57}$$

$$r_\infty(v) = I_{ss}(v) - I_p(v). \tag{3.58}$$

Since, $I_p(v_{rest}) = I_{ss}(v_{rest}) = 0$, we know that $f(v_{rest}) = r_\infty(v_{rest}) = 0$. Thus, we can simplify our initial system of equations to the following:

$$C_{sp}\frac{\partial V_{sp}}{\partial T} = -f(V_{sp}) - I_{syn}(x,t) - I_N - r, \tag{3.59}$$

$$\frac{\partial r}{\partial T} = \frac{r_\infty(V_{sp}) - r}{\tau_r}, \tag{3.60}$$

$$\tau\frac{\partial V_d}{\partial T} = \lambda^2\frac{\partial^2 V_d}{\partial X^2} - V_d + \frac{\rho R_{\infty,d}}{R_N}(V_{sp} - V_d). \tag{3.61}$$

Notice that if $I_{syn} = 0$, then $V_{sp} = V_d = 0$ is a rest state of the system. Since we mainly will be interested in traveling wave phenomena not aided by synaptic currents, we can drop the I_{syn} term from (3.59).

In order to make the equations more tractable analytically, typically f is chosen to be a cubic polynomial, and hence the largest root corresponds to the sodium reversal potential, V_{Na}. Furthermore, we usually choose $r_\infty(v) = \sigma v$, $\sigma > 0$. Thus we can write (3.59) and (3.60) as

$$C_{sp}\frac{\partial V_{sp}}{\partial T} = g_{active}V_{sp}(V_{sp} - V_1)(V_{Na} - V_{sp}) - \frac{V_{sp} - V_d}{R_N} - r, \tag{3.62}$$

$$\frac{\partial r}{\partial T} = \frac{1}{\tau_r}(\sigma V_{sp} - r). \tag{3.63}$$

If we divide (3.62) and (3.63) by $V_{Na}g_{active}$ and (3.61) by V_{Na} and make the following substitutions:

$$\tau_s = \frac{C_{sp}}{g_{active}}, \tag{3.64}$$

$$\tau = \frac{\tau_m}{\tau_s}, \tag{3.65}$$

$$\bar{\tau}_r = \frac{\tau_r}{\tau_s}, \tag{3.66}$$

$$\gamma = \frac{1}{g_{active}R_N}, \tag{3.67}$$

$$\kappa = \frac{\rho R_{\infty,d}}{R_N}, \tag{3.68}$$

$$\psi = \frac{\sigma}{g_{active}}, \tag{3.69}$$

$$t = \frac{T}{\tau_s}, \tag{3.70}$$

$$x = \frac{X}{\lambda}, \tag{3.71}$$

$$a = \frac{V_1}{V_{Na}}, \tag{3.72}$$

$$v = \frac{V_{sp}}{V_{Na}}, \tag{3.73}$$

$$w = \frac{V_d}{V_{Na}}, \tag{3.74}$$

$$s = \frac{r}{g_{active}V_{Na}}, \tag{3.75}$$

we obtain

$$\frac{\partial v}{\partial t} = v(v-a)(1-v) + \gamma(w-v) - s, \tag{3.76}$$

$$\frac{\partial s}{\partial t} = \frac{1}{\bar{\tau}_r}(\psi v - s), \tag{3.77}$$

$$\tau\frac{\partial w}{\partial t} = \frac{\partial^2 w}{\partial x^2} - w + \kappa(v-w). \tag{3.78}$$

In general, the value of τ_r will be large $O(10^3)$ (according to [18]), and we see that for $t = O(1)$, $s = O(\frac{1}{\bar{\tau}_r})$. Thus, to leading order, we may assume that $s = 0$. This simplifies the above equations to:

$$\frac{\partial v}{\partial t} = v(v-a)(1-v) + \gamma(v-w), \tag{3.79}$$

$$\frac{\partial w}{\partial t} = \frac{\partial^2 w}{\partial x^2} - \frac{1}{\tau}w + \frac{\kappa}{\tau}(v-w). \tag{3.80}$$

Except for the cubic term, this is the set of equations that will be studied here. Having dropped the recovery term, these sets of equations will not yield pulse solutions, in general, but under certain conditions I will show that traveling front solutions of constant shape and speed can be obtained.

I will look at three different cases. In the first case, I will replace the cubic by a piecewise-linear term $-v+H(v-a)$ where H is a Heaviside function. In the second case, I will look at the case where the cubic is replaced by a piecewise linear continuous function which attains the same maxima and minima at the same places as the cubic and has roots at $v = 0$ and $v = 1$. In the last case, I will examine the cubic case in (3.79) and (3.80).

Chapter 4
Piecewise Linear Discontinuous Model

In this chapter, we begin to look at the model when the cubic polynomial is replaced with a piecewise linear approximation, $v - H(v - a)$ where H is a Heaviside function. This model is quite simple, allows for explicit closed form solutions, and still has the general shape of the cubic.

The purpose of these approximations is to attain the same fundamental dynamic structure for the traveling front solution of constant profile and speed, but with much simpler functions. Hopefully, the approximations are close enough to show how the solution changes and how it depends on the values of the parameters. Linear functions are nice because solving ODEs with constant coefficients is equivalent to solving for the roots of polynomials, which is a much simpler problem analytically and numerically. Also, it affords the possibility of using "continuation" methods to determine how speed depends on certain parameters once a single solution is found. This technique was used successfully by Rinzel to show that the modified FHN equations have a slow, unstable solution [92], which had been suspected from numerical experiments.

The form of the equations that we are studying is:

$$\frac{\partial v}{\partial t} = H(v-a) - v + \gamma(w-v), \tag{4.1}$$

$$\frac{\partial w}{\partial t} = \frac{\partial^2 w}{\partial x^2} - \frac{w}{\tau} + \frac{\kappa}{\tau}(v-w), \tag{4.2}$$

where $\gamma > 0$, $\kappa > 0$, $\tau > 0$, and $a > 0$.

Our approach will initially be to look at the spatially homogeneous steady state solutions to the problem. We will be especially interested in those cases where at least two such steady states exist. We will then proceed to search for constant speed solutions, and use a substitution to reduce the system of PDEs to a boundary value problem for a system of ODEs. The specific type of solution that we are looking for is a traveling front between the two steady state solutions. We will begin by demonstrating the existence of constant speed solutions for certain parameter sets. Then we will use numerics to generate solutions for traveling fronts and examine the dependence of the shape and speed of the front on the different parameters.

4.1 Spatially homogeneous steady states

We begin this study by examining the spatially homogeneous steady states, which are obtained by dropping the $\frac{\partial^2 w}{\partial x^2}$ term from (4.2) and then setting the left–hand sides of (4.1) and (4.2) equal to 0. Thus,

$$0 = H(v-a) - (1+\gamma)v + \gamma w, \tag{4.3}$$

$$0 = -(1+\kappa)w + \kappa v. \tag{4.4}$$

If $v < a$, then $H(v-a) = 0$, and the system reduces to:

$$0 = -(1+\gamma)v + \gamma w, \tag{4.5}$$

$$0 = \kappa v - (1+\kappa)w, \tag{4.6}$$

which only has the trivial solution $v = w = 0$. If $v > a$, then $H(v-a) = 1$, and (4.3) and (4.4) become

$$-1 = -(1+\gamma)v + \gamma w, \tag{4.7}$$

$$0 = \kappa v - (1+\kappa)w. \tag{4.8}$$

The solutions are $v = v_s$ and $w = w_s$ where

$$v_s = \frac{1+\kappa}{1+\kappa+\gamma} > a, \tag{4.9}$$

$$w_s = \frac{\kappa}{1+\kappa+\gamma}. \tag{4.10}$$

The inequality in (4.9) can be rewritten as

$$\frac{\gamma}{1+\kappa} < \frac{1-a}{a} \tag{4.11}$$

and is a consistency condition for the existence of the nontrivial spatially homogeneous steady state:

Now we shall explore the stability of these steady states. The stability matrix corresponding to both steady states (they have the same stability matrix because $H(v-a)$ only contributes a constant) is given by:

$$A = \begin{bmatrix} -(1+\gamma) & \gamma \\ \kappa & -(1+\kappa) \end{bmatrix}. \tag{4.12}$$

If we solve for the determinant and trace, we get

$$det(A) = 1+\kappa+\gamma > 0, \tag{4.13}$$

$$tr(A) = -(2+\kappa+\gamma) < 0. \tag{4.14}$$

$$\tag{4.15}$$

The determinant of A is positive and the trace of A is negative, which imply that the

eigenvalues of A, given by

$$\lambda_1 = \frac{trace(A) + \sqrt{trace^2(A) - 4det(A)}}{2}, \tag{4.16}$$

$$\lambda_2 = \frac{trace(A) - \sqrt{trace^2(A) - 4det(A)}}{2}, \tag{4.17}$$

are both negative. Thus both steady states are stable. Note that this situation is not possible for a continuous dynamical system, where stable steady states always are separated by an unstable steady state.

We now ask under what conditions, in addition to the consistency condition (4.11), do traveling front solutions between the two steady states exist.

4.2 Traveling front solutions

We now seek out solutions that travel with constant speed $c > 0$ to the right with unchanging shape. It should be noted that we designate the speed to be positive arbitrarily here. Solutions with negative speed do exist as well. Such solutions can be thought of as the wave dying out, whereas solutions with positive speed can be thought of as the wave actively propagating forward. Introduce the following change of variables to a traveling wave frame:

$$z = x - ct, \tag{4.18}$$

$$t^* = t. \tag{4.19}$$

Substituting this change of variables into (4.1) and (4.2), we get

$$\frac{\partial v}{\partial t^*} - c\frac{\partial v}{\partial z} = H(v - a) - v + \gamma(w - v), \tag{4.20}$$

$$\frac{\partial w}{\partial t^*} - c\frac{\partial w}{\partial z} = \frac{\partial^2 w}{\partial z^2} - \frac{w}{\tau} + \frac{\kappa}{\tau}(v - w). \tag{4.21}$$

Since we are looking for solutions which go from the steady state $(v = 0, w = 0)$ to the steady state $(v = v_s, w = w_s)$, our boundary conditions are

$$\lim_{z\to\infty} w(z,t^*) = 0, \tag{4.22}$$

$$\lim_{z\to\infty} v(z,t^*) = 0, \tag{4.23}$$

$$\lim_{z\to-\infty} w(z,t^*) = w_s, \tag{4.24}$$

$$\lim_{z\to-\infty} v(z,t^*) = v_s. \tag{4.25}$$

We are looking for continuous solutions for positive speed traveling fronts. Hence, we know that there is some value of z, say $z = z_0$, such that $v(z_0) = a$. Notice that (4.20) and (4.21) are autonomous in z, and thus horizontal translation of a solution is also a solution because the boundary conditions are at infinity. Thus, we shall arbitrarily choose $z_0 = 0$ for simplicity. That is, our consistency condition is $lim_{z\to 0^+} v(z,t^*) = a$ (Note, we have asked for the right–hand limit because solutions to the problem for $c = 0$ are not continuous about $v = a$ but have a jump discontinuity. We can, nevertheless, satisfy this condition). For this problem, we are interested in fronts which represent steady state solutions in the traveling wave frame. Thus, we may drop the time-derivative terms from (4.20) and (4.21) to obtain

$$-cv' = H(v-a) - v + \gamma(v-w), \tag{4.26}$$

$$-cw' = w'' - \frac{w}{\tau} + \frac{\kappa}{\tau}(v-w), \tag{4.27}$$

where $'$ denotes differentiation with respect to z, subject to an overdetermined number of boundary conditions; the problem is third order, but there are four boundary conditions,

and one consistency condition:

$$\lim_{z\to\infty} w(z) = 0, \tag{4.28}$$

$$\lim_{z\to\infty} v(z) = 0, \tag{4.29}$$

$$\lim_{z\to-\infty} w(z) = w_s, \tag{4.30}$$

$$\lim_{z\to-\infty} v(z) = v_s, \tag{4.31}$$

$$\lim_{z\to 0^+} v(z) = a. \tag{4.32}$$

We can eliminate the variable v. Solving (4.27) for v yields

$$v = -\frac{\tau}{\kappa}\left[w'' + cw' - \frac{1+\kappa}{\tau}w\right], \tag{4.33}$$

and differentiation of this equation gives

$$v' = -\frac{\tau}{\kappa}\left[w''' + cw'' - \frac{1+\kappa}{\tau}w'\right]. \tag{4.34}$$

Substituting for v and v' from (4.33) and (4.34), respectively, into (4.26), we obtain

$$cw''' + \left[c^2 - (1+\gamma)\right]w'' - c\left[1+\gamma+\frac{1+\kappa}{\tau}\right]w' + \frac{1+\kappa+\gamma}{\tau}w = \frac{\kappa}{\tau}H(-z). \tag{4.35}$$

Notice that if the following three boundary conditions are met, the other two boundary conditions in (4.28)–(4.32) are automatically satisfied because they correspond to the fulfillment of steady state conditions:

$$\lim_{z\to-\infty} w(z) = w_s, \tag{4.36}$$

$$\lim_{z\to\infty} w(z) = 0, \tag{4.37}$$

$$\lim_{z\to 0+} v(z) = a. \tag{4.38}$$

We proceed to solve for solutions of (4.35) for the special case $c = 0$, which is the easiest case because the third derivative term in (4.35) drops out and reduces the order of the equation. Moreover, this case should give the boundary of the region in the parameter space that corresponds to the existence of positive speed traveling wave solutions.

4.2.1 Stationary front solutions

We set $c = 0$ in (4.35) to obtain the second-order ODE

$$-(1+\gamma)w'' + \frac{1+\kappa+\gamma}{\tau}w = \kappa H(-z). \tag{4.39}$$

The general solution, $w_g(z)$, for this ODE is

$$w_g(z) = \begin{cases} b_{1,1}e^{-\mu z} + b_{1,2}e^{\mu z}, & z < 0, \\ b_{2,1}e^{-\mu z} + b_{2,2}e^{\mu z}, & z > 0, \end{cases} \tag{4.40}$$

where

$$\mu = \sqrt{\frac{1+\kappa+\gamma}{\tau(1+\gamma)}}. \tag{4.41}$$

To match the boundary conditions, we require $b_{1,1} = b_{2,2} = 0$. A particular solution, $w_p(z)$, to (4.39) is given by

$$w_p(z) = \begin{cases} w_s, & z < 0, \\ 0, & z > 0, \end{cases} \tag{4.42}$$

To match the coefficients of $z = 0$, notice that from (4.26) either w or v must have a jump discontinuity when $c = 0$ at $z = 0$. Physically, it makes more sense for v to be discontinuous because it represents spine head voltage. Thus, we look for a solution w which is C^1 in z. For w to be continuous at $z = 0$, we require

$$b_{1,2} + w_s = b_{2,1}, \tag{4.43}$$

and for w to be differentiable at $z = 0$, we require

$$\mu b_{1,2} = -\mu b_{2,1}. \tag{4.44}$$

These yield

$$b_{1,2} = -b_{2,1} = -\frac{w_s}{2}. \tag{4.45}$$

Thus, the solution to (4.39) is

$$w(z) = \begin{cases} \frac{w_s}{2}(2 - e^{\mu z}), & z < 0, \\ \frac{w_s}{2}e^{-\mu z}, & z > 0. \end{cases} \tag{4.46}$$

Now applying (4.33) with $c = 0$, and substituting in for μ using (4.41), we get

$$v(z) = \begin{cases} v_s - \frac{\gamma w_s}{2(1+\gamma)}, & z < 0, \\ \frac{\gamma w_s}{2(1+\gamma)}e^{-\mu z}, & z > 0. \end{cases} \tag{4.47}$$

Applying our matching condition, (4.38), at $z = 0$, we get (after using (4.10) for w_s)

$$\frac{\gamma\kappa}{(1+\gamma)(1+\gamma+\kappa)} = 2a. \tag{4.48}$$

At this point it is hard to say which way the inequality should go for positive speed waves, but intuitively we should expect that smaller values of a make the system more excitable. Thus, the correct condition is

$$\frac{\gamma\kappa}{(1+\gamma)(1+\gamma+\kappa)} > 2a. \tag{4.49}$$

If we rewrite the left–hand side as

$$\frac{\gamma}{1+\gamma}\frac{\kappa}{1+\kappa+\gamma}, \tag{4.50}$$

then it is easy to see that the left–hand side of the matching condition is always less than one. Thus, we see that there are no positive speed solutions for $a \geq \frac{1}{2}$, which is a classical result from the ordinary FHN equations.

4.2.2 Positive speed traveling wave fronts

We look for solutions to (4.35)–(4.38) for which $c > 0$. If we substitute $w = e^{yz}$ into (4.35), we get the characteristic polynomial:

$$cp(y) = cy^3 + \left[c^2 - (1+\gamma)\right] y^2 - c\left[1 + \gamma + \frac{1+\kappa}{\tau}\right] y + \frac{1+\kappa+\gamma}{\tau}. \tag{4.51}$$

Notice that $cp(0) > 0$ and $cp'(0) < 0$. Thus, cp always has one negative real root and may have two positive real roots, a positive root of multiplicity two, or two complex roots with positive real part.

Suppose there are three real roots, $\mu_1 < 0 < \mu_2 < \mu_3$; then, we know that using the technique used above, we can find a solution for w given by

$$w(z) = \begin{cases} b_{1,2}e^{\mu_2 z} + b_{1,3}e^{\mu_3 z} + w_s, & z < 0, \\ b_{2,1}e^{\mu_1 z}, & z > 0. \end{cases} \tag{4.52}$$

Requiring continuity of w and its first two derivatives at $z = 0$ yields

$$b_{1,2} + b_{1,3} - b_{2,1} = -w_s, \tag{4.53}$$

$$\mu_2 b_{1,2} + \mu_3 b_{1,3} - \mu_1 b_{2,1} = 0, \tag{4.54}$$

$$\mu_2^2 b_{1,2} + \mu_3^2 b_{1,3} - \mu_1^2 b_{2,1} = 0. \tag{4.55}$$

This system of equations has the solution

$$b_{2,1} = w_s b_1, \tag{4.56}$$

$$b_{1,2} = w_s b_2, \tag{4.57}$$

$$b_{1,3} = w_s b_3, \tag{4.58}$$

where (4.59)

$$b_1 = \frac{\mu_2\mu_3}{(\mu_3 - \mu_1)(\mu_2 - \mu_1)}, \tag{4.60}$$

$$b_2 = \frac{\mu_1\mu_3}{(\mu_3 - \mu_2)(\mu_2 - \mu_1)}, \tag{4.61}$$

$$b_3 = -\frac{\mu_1\mu_2}{(\mu_3 - \mu_1)(\mu_3 - \mu_2)}. \tag{4.62}$$

Thus, $b_{2,1} > 0$, $b_{1,2} < 0$, and $b_{1,3} > 0$. We define

$$g(\mu) = \mu^2 + c\mu - \frac{1+\kappa}{\tau}, \tag{4.63}$$

so using (4.33), we obtain the solution

$$v(z) = \begin{cases} -\frac{\tau w_s}{\kappa}\left[b_3 g(\mu_3)e^{\mu_3 z} + b_2 g(\mu_2)e^{\mu_2 z}\right] + v_s, & z < 0, \\ -\frac{b_1 \tau w_s}{\kappa} g(\mu_1)e^{\mu_1 z}, & z > 0. \end{cases} \tag{4.64}$$

In order to satisfy our matching condition, (4.38), we require

$$-\frac{\tau b_1 w_s}{\kappa} g(\mu_1) = a, \tag{4.65}$$

which may be rewritten in terms of the eigenvalues as

$$\frac{\mu_2\mu_3\left(\mu_1^2 + c\mu_1 - \frac{1+\kappa}{\tau}\right)}{(\mu_3 - \mu_1)(\mu_2 - \mu_1)} = -\frac{a(1+\kappa+\gamma)}{\tau}. \tag{4.66}$$

If we could find a "near-by solution" for some parameter set to the above problem, then we could use continuation to get a feel for the dependence of c on the parameters. We have a solution for $c = 0$, but that solution is degenerate because $\mu_3 \to \infty$ as $c \to 0$. The obvious method for getting an initial non–degenerate guess is to use singular perturbation techniques.

Assume that κ, τ and a are fixed, and that $c = \epsilon$ is a small parameter. Expand γ in powers of ϵ as

$$\gamma = \gamma_0 + \epsilon\gamma_1 + \ldots \tag{4.67}$$

where

$$\frac{\gamma_0\kappa}{(1+\gamma_0)(1+\gamma_0+\kappa)} = 2a. \tag{4.68}$$

Our boundary condition (4.36) can be expanded as

$$w_s = w_1 + \epsilon w_2 + O(\epsilon^2), \tag{4.69}$$

$$w_1 = \frac{\kappa}{1+\kappa+\gamma_0}, \tag{4.70}$$

$$w_2 = -\frac{w_1\gamma_1}{1+\kappa+\gamma_0}. \tag{4.71}$$

We need to obtain corrections to the eigenvalues. Here, we expect that

$$\mu_1 = \mu_{1,1} + \epsilon\mu_{1,2} + O(\epsilon^2), \tag{4.72}$$

$$\mu_2 = \mu_{2,1} + \epsilon\mu_{2,2} + O(\epsilon^2), \tag{4.73}$$

$$\mu_{1,1} = -\mu, \tag{4.74}$$

$$\mu_{2,1} = \mu. \tag{4.75}$$

If we substitute the above equations into (4.51), and collect terms of $O(\epsilon)$, we get

$$\mu_{1,2} = \frac{\kappa}{2(1+\kappa+\gamma_0)}, \tag{4.76}$$

$$\mu_{2,2} = -\frac{\kappa}{2(1+\kappa+\gamma_0)}. \tag{4.77}$$

In order to come up with an expansion for μ_3, we guess that to leading order, $\mu_3 = \frac{\mu_{3,1}}{\epsilon^p}$ where $p > 0$. Substituting this into (4.51), we get

$$\epsilon^{1-3p}\mu_{3,1}^3 + \epsilon^{-2}\left[\epsilon^2 - (1+\gamma)\right]\mu_{3,1}^2 - \epsilon\left(1+\gamma+\frac{1+\kappa}{\tau}\right) + \frac{1+\kappa+\gamma}{\tau}. \tag{4.78}$$

We get the correct value of p if we match the leading-order quadratic and cubic terms. Thus, $p = 1$. We try to expand μ_3 as

$$\mu_3 = \frac{\mu_{3,1}}{\epsilon} + \mu_{3,2} + \epsilon\mu_{3,3} + \ldots. \tag{4.79}$$

Substituting the above expression into (4.51) and collecting powers of ϵ^{-2} and ϵ^{-1}, respectively, we get

$$\mu_{3,1} = 1 + \gamma_0, \tag{4.80}$$

$$\mu_{3,2} = \gamma_1. \tag{4.81}$$

Now we need to suggest an asymptotic expansion for the coefficients. In this case, we have an exact formula for them in terms of the eigenvalues and the steady states (equations

(4.56)–(4.62) for which we have expansions. One thing that should be noticed from (4.62) is that b_3 is $O(\epsilon^2)$ as $\epsilon \to 0$. However, the exponential term is $O(e^{O(\frac{1}{\epsilon})})$ so its effects are first felt in the second derivative of w, and we can see this evolving into a jump condition in w as $\epsilon \to 0$. Notice that v gets some contribution from w'' in (4.33). Thus we see that v has a jump discontinuity in the limiting case as $c \to 0$. This could be easily seen if one refers back to (4.26) and sets $c = 0$. Here there is a jump when v crosses a, and since it is not in w, it must be in v. The solution is constructed in this manner since w is only indirectly coupled to the nonlinearity, and its effects are damped out.

Returning to solving for the constants, we can solve for the corrections to all of the constants easily and can derive an answer which is only dependent upon γ_1 which is still unknown. To get a guess for γ_1, we have to apply the matching condition (4.38). From (4.64), this condition is equivalent to

$$w_s b_1 g(\mu_1) = -\frac{a\kappa}{\tau}. \tag{4.82}$$

In order to tackle this problem efficiently, we'll need some more notation. Let us write $g(\mu_1)$ as

$$g(\mu_1) = g_0(\mu_1) + \epsilon g_1(\mu_1) \tag{4.83}$$

where

$$g_0(\mu_1) = \mu_1^2 - \frac{1+\kappa}{\tau}, \tag{4.84}$$

$$g_1(\mu_1) = \mu_1, \tag{4.85}$$

and expand b_1 as

$$b_1 = \beta_{1,1} + \epsilon\beta_{1,2} + O(\epsilon^2) \tag{4.86}$$

where

$$\beta_{1,1} = \frac{\mu_{2,1}}{\mu_{2,1} - \mu_{1,1}}, \tag{4.87}$$

$$\beta_{1,2} = \frac{\mu_{2,1}}{\mu_{3,1}(\mu_{2,1} - \mu_{1,1})^2}\left[\mu_{3,1}(\mu_{2,2} - \mu_{1,2}) + (\mu_{3,2} - \mu_{1,1})(\mu_{2,1} - \mu_{1,1})\right] \tag{4.88}$$

$$+\frac{\mu_{2,1}\mu_{3,2} + \mu_{2,2}\mu_{3,1}}{\mu_{3,1}(\mu_{2,1} - \mu_{1,1})}. \tag{4.89}$$

We now match the coefficients of ϵ in (4.82) to obtain

$$0 = w_1 g(\mu_{1,1})\beta_{1,1} + \frac{a\kappa}{\tau}, \tag{4.90}$$

$$0 = w_1\beta_{1,1}[g_0'(\mu_{1,1})\mu_{1,2} + g_1(\mu_{1,1})] + w_1\beta_{1,2}g_0(\mu_{1,1}) + w_2\beta_{1,1}g_0(\mu_{1,1}). \tag{4.91}$$

Equation (4.90) is equivalent to condition (4.48) if condition (4.68) holds. If we solve (4.91) for γ_1, we can use the asymptotics to approximate a guess for a solution with speed ϵ for a particular choice of a, κ, and τ.

Now that we have a means for making a guess, we can use numerics to try to determine solution sets of (μ_1, μ_2, μ_3, c) in terms of $(a, \gamma, \kappa, \tau)$ to determine the effects of the parameters on the shape (which is determined by the eigenvalues) and the speed (which is given by c) of the wave.

4.3 Numerical results

4.3.1 Varying a

In this section, we vary a over the acceptable ranges for $\gamma = 1.5$, $\kappa = 5$, and $\tau = 10$.

In Figure 4.1, we show the speed of the wave as a function of a.

Here we get the intuitively obvious result that c is a monotonic decreasing function of a, *ceteris paribus*. It appears that speed may be becoming large as $a \to 0$, but strictly speaking, it is not appropriate to allow $a = 0$, so this result will not be commented upon more here.

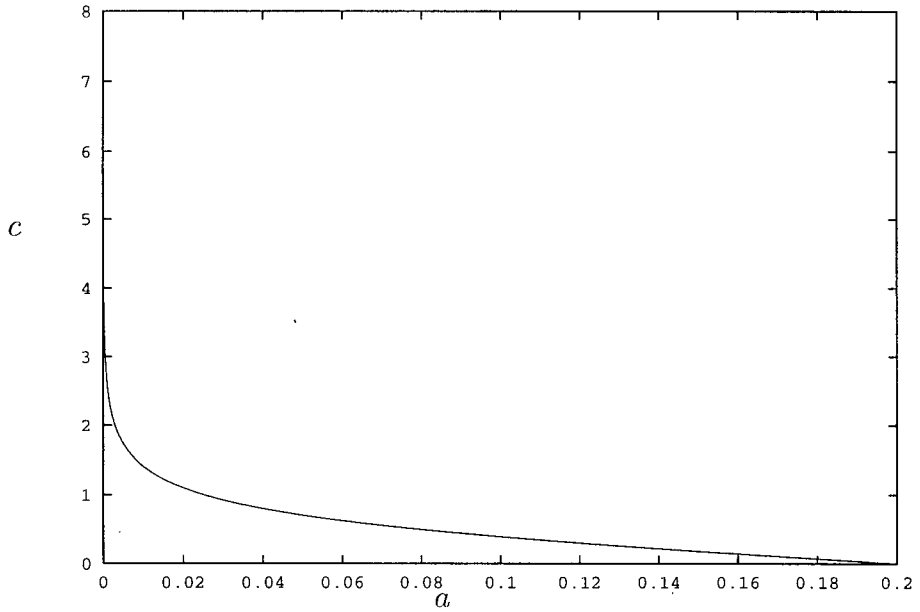

Figure 4.1: Speed of the wave, c, as a function of a for $\gamma = 1.5$, $\kappa = 5$, $\tau = 10$.

If we look at Figure 4.2, we get the expected result that $\mu_3 \to \infty$ as we approach the value of a where speed goes to zero (a wider range for a is not shown because the scaling of the graph required to enclose μ_3 obscures μ_2, and μ_1. We also get the result that as the speed goes to zero $\mu_2 + \mu_1 \to 0$.

4.3.2 Varying κ

In this section we will graph the results obtained for the values of the speed of the wave and the eigenvalues as functions of κ for fixed values of a, γ and τ.

In Figure 4.3 we have graphed the speed of the wave as a function of κ. Here we see that there is some minimum value of κ for which are no positive speed traveling front solutions. This intuitively makes sense as κ measures the ability of the spines to depolarize

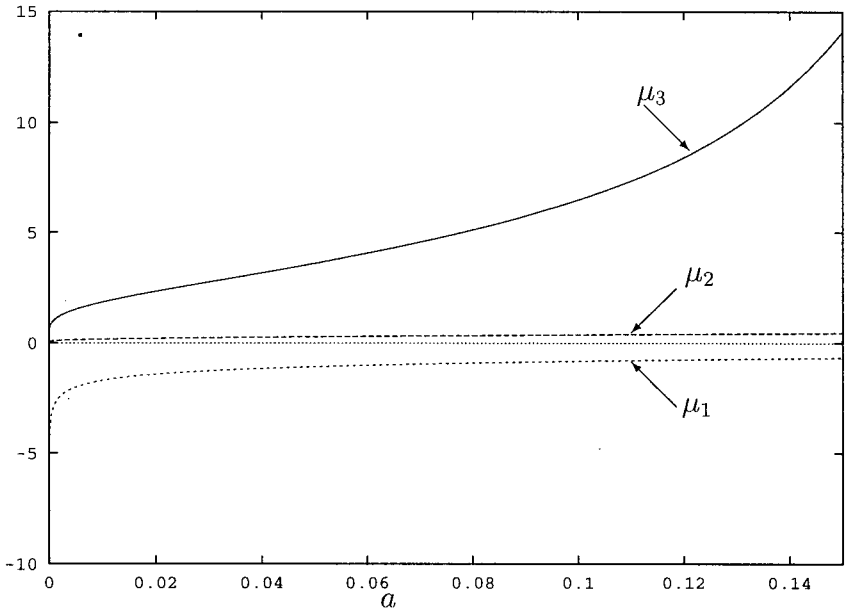

Figure 4.2: Eigenvalues of the wave as functions of a for $\gamma = 1.5$, $\kappa = 5$, $\tau = 10$.

the dendritic shaft. Furthermore, there is some definite maximum value of c for a certain value of κ. Thereafter, the speed of the wave gradually decreases as κ increases. This also makes sense, since κ becoming large is equivalent to the spine density going to infinity which creates a tremendous conductance load that must be overcome to bring spines at the leading edge of the front up to threshold.

In Figure 4.4 we have graphed the eigenvalues of the wave as a function of κ.

4.3.3 Varying γ

In this section, we graph the speed and the eigenvalues of the wave as functions of γ for fixed a, κ and τ.

In Figure 4.5, we have graphed the speed of the wave as a function of γ. As was the case

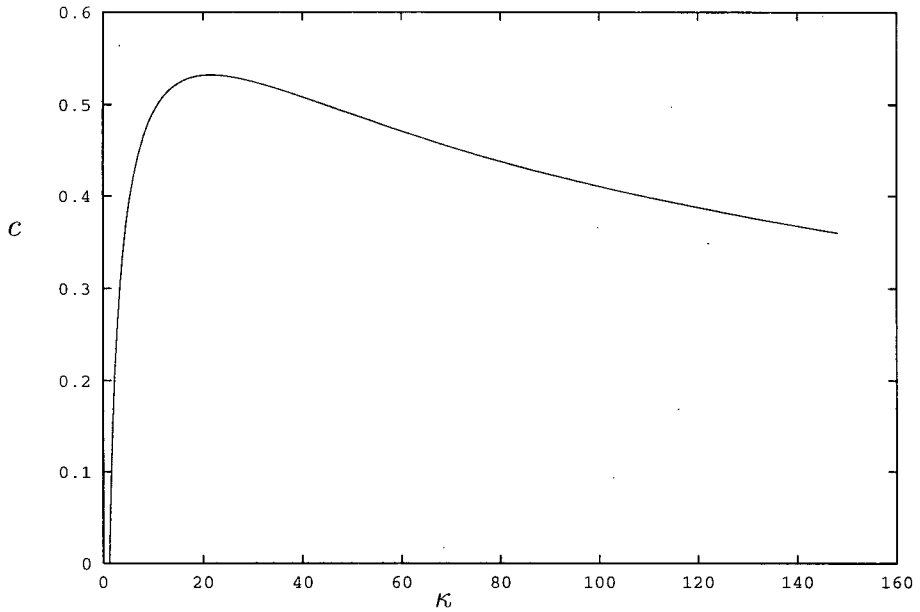

Figure 4.3: Speed of the wave, c, as a function of κ for $a = 0.1$, $\gamma = 1.5$, $\tau = 10$.

for κ, the general shape of the wave is a skewed hump. However, in this case, there is also an upper value of γ which corresponds to a zero–speed wave. The idea that there must be some maximum value of γ above which there are no positive speed traveling waves makes intuitive sense. If γ is too large, then the current generated within the spine head is quickly lost to the dendritic shaft and the spine is not able to reach threshold. The fact that the speed of the wave should become smaller for very small values of γ is related to the fact that the spine head saturates quickly so little current is delivered to the parent dendrite.

In Figure 4.6 we have graphed μ_1 and μ_2 as functions of γ. We again notice that as γ approaches the two values which correspond to zero–speed waves, $\mu_1 + \mu_2 \to 0$.

In Figure 4.7 we have graphed μ_3 as a function of γ. It is easier to see the tendency of μ_3

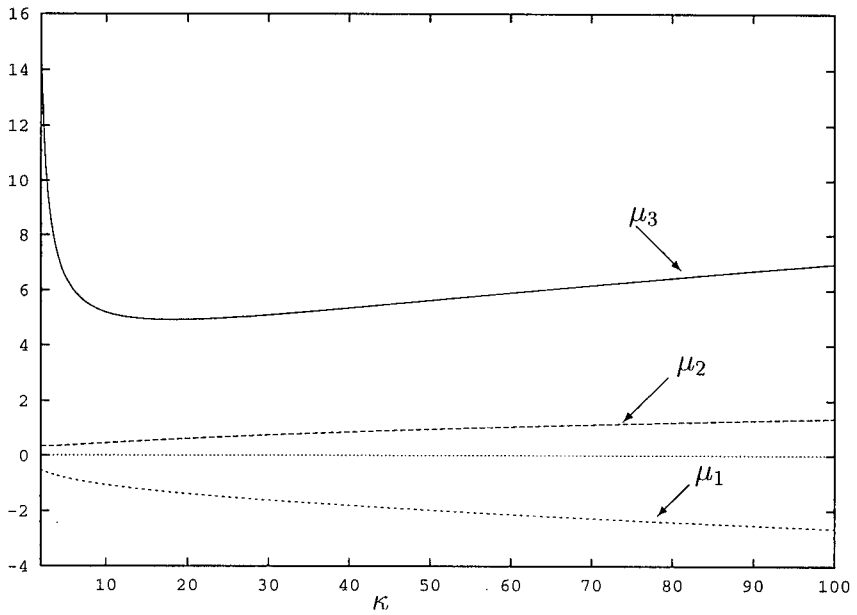

Figure 4.4: Eigenvalues of the wave as functions of κ for $a = 0.1$, $\gamma = 1.5$, $\tau = 10$. It should be noted that the abscissa here is not zero, but is a value close the value of κ which corresponds to zero–speed waves as shown in Figure 4.3.

to become large as γ goes to its upper limit which corresponds to zero–speed waves, but the same occurs at the lower limit as well. It is difficult to graph this region thoroughly due to numerical instability of the routine used.

4.3.4 Varying τ

In this section, we have graphed the speed of the wave, and the eigenvalues as functions of τ for fixed values of a, γ and κ.

In Figure 4.8 we have graphed the speed of the wave as a function of τ. In this case, we have actually graphed $c\sqrt{\tau}$ as a function of τ. This is due to the fact that the original scaling involved a nondimensionalization by a length scale. If we plotted c against τ

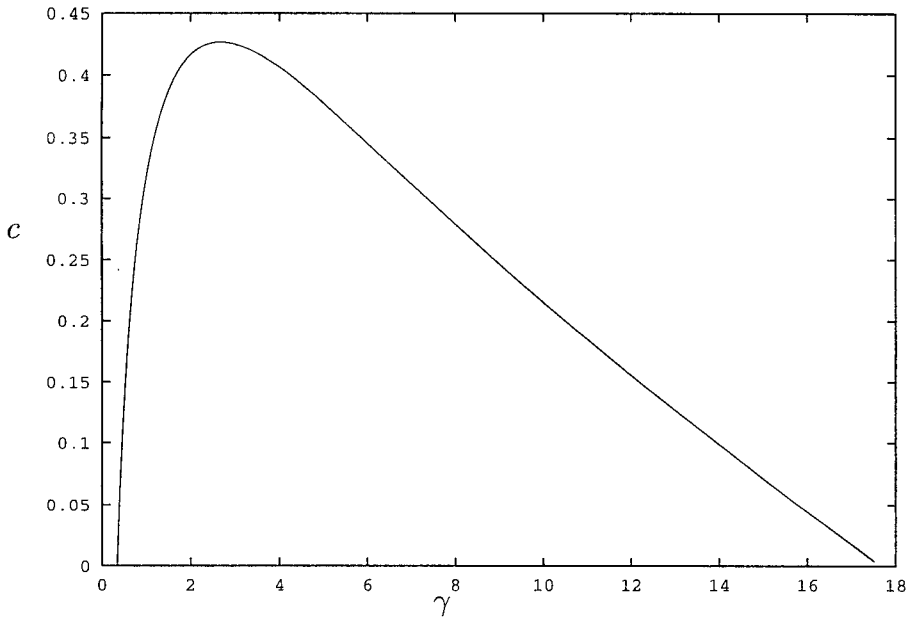

Figure 4.5: Speed of the wave, c, as a function of γ for $a = 0.1$, $\kappa = 5$, $\tau = 10$.

directly, we would get the erroneous impression that $c \to 0$ as $\tau \to \infty$. Physically, τ represents a time-scale of active dynamics in the spine head. We intuitively expect that the speed of the wave should plateau to some maximum value as the speed of the active dynamics becomes very fast. This is, in fact, the case when we correct for the space scaling factor introduced earlier.

In Figure 4.9 we have graphed μ_1 and μ_2 against τ. We have performed a scaling here as well to correct for the initial nondimensionalization. In this case, we see that the long–scale shape of the wave is not appreciably affected by changes in τ as one would intuitively expect. Where we would expect to see a change is in the short–scale behaviour close to the discontinuity in the equation. This is reflected in μ_3 as shown in Figure 4.10.

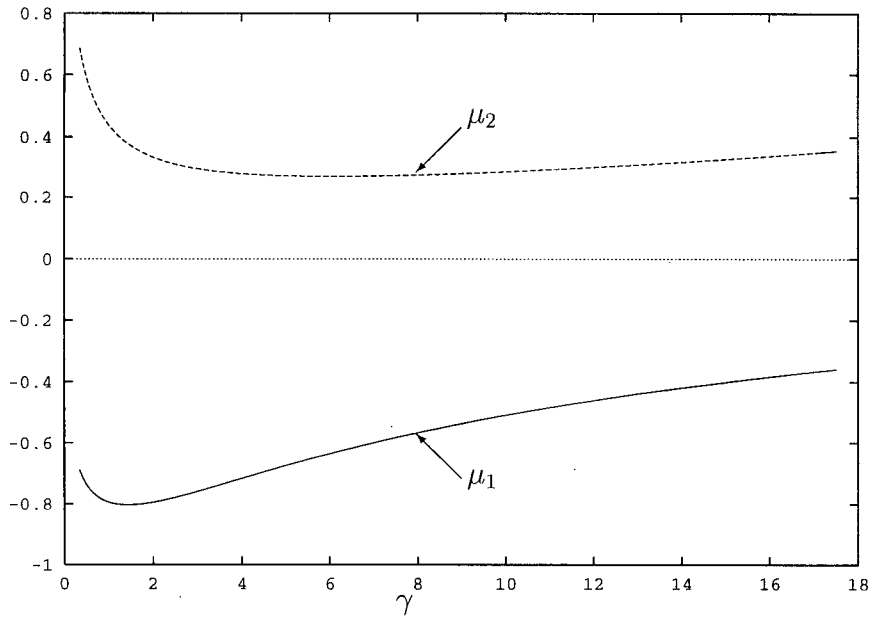

Figure 4.6: Eigenvalues, μ_1 and μ_2, as functions of γ for $a = 0.1$, $\kappa = 5$, $\tau = 10$. The abscissa is not zero in this graph. It corresponds to the lower value of γ which corresponds to zero–speed waves as can be seen in Figure 4.5.

4.4 Numerical simulation of the PDE model

The analytical method we developed for the system of ODEs was extremely useful in exploring some of the important regions of the parameter space. It allowed us to develop an intuitive understanding of some of the processes involved in traveling wave front propagation. Unfortunately, it fails to address whether the solution we found is stable or unstable. Naturally, this would be a good thing to know since the fronts discovered will not be seen experimentally if they correspond to unstable solutions. Since no proof of the stability of the system exists, we decided to examine the system of PDEs numerically using PDEcol.

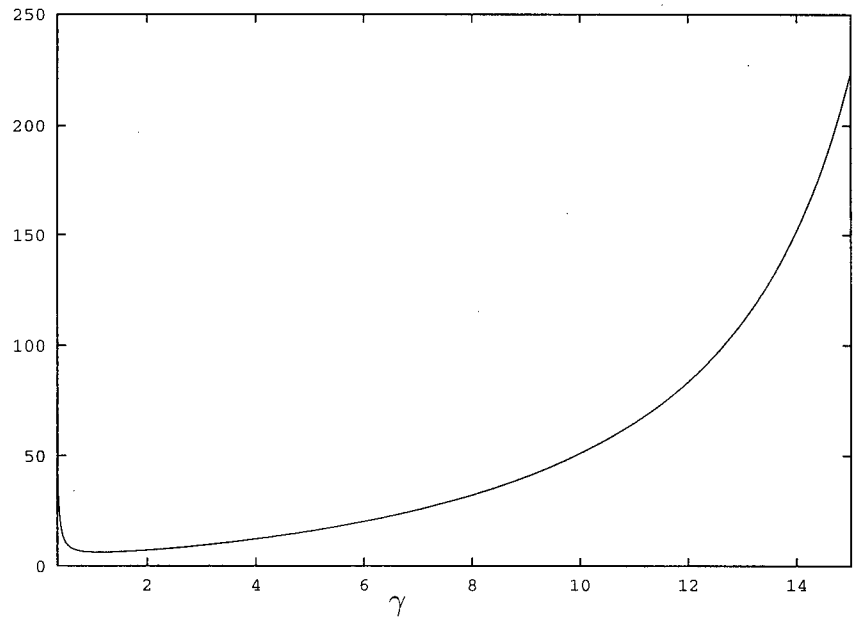

Figure 4.7: Graph of μ_3 as a function of γ for $a = 0.1$, $\kappa = 5$, $\tau = 10$.

Our procedure was to run PDEcol using Neumann boundary conditions, and the initial guess was the computed solution from our analysis (slight perturbations to the initial guess were also made, and they gave the same results). The result is shown in Figure 4.11. The traveling front appears to propagate to the right with approximately the theoretically computed speed without changing shape. This acts to confirm our previous analysis, and strongly suggests that the solution we have discovered corresponds to a stable solution.

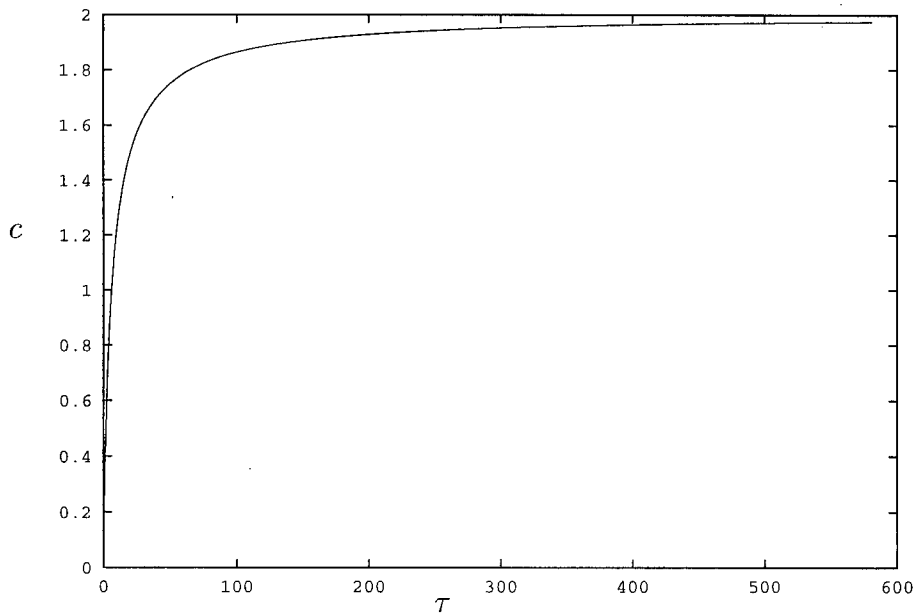

Figure 4.8: Speed of the wave, c, as a function of τ for $a = 0.1$, $\gamma = 1$, $\kappa = 5$.

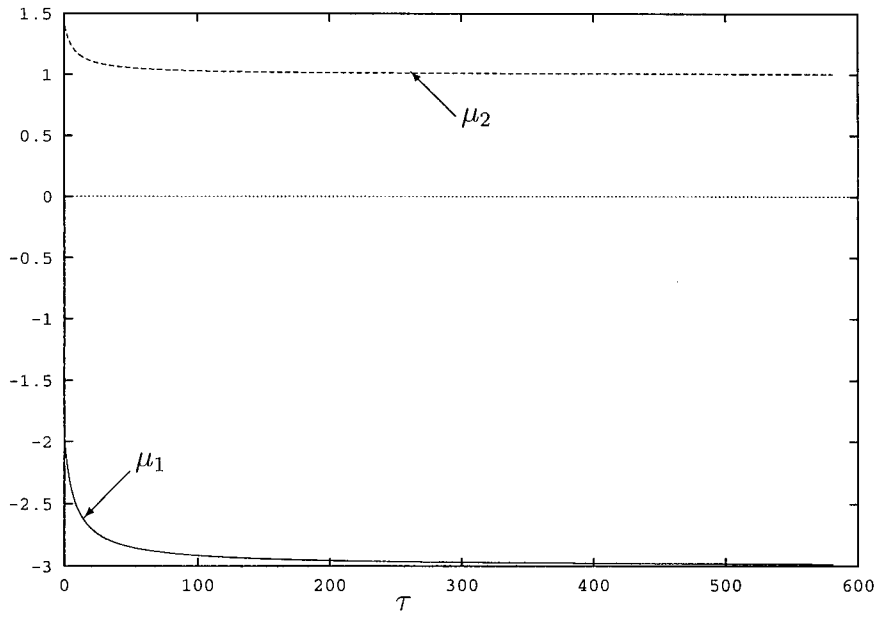

Figure 4.9: Graphs of μ_1 and μ_2 as functions of τ for $\gamma = 1$, $\kappa = 5$, $\tau = 10$.

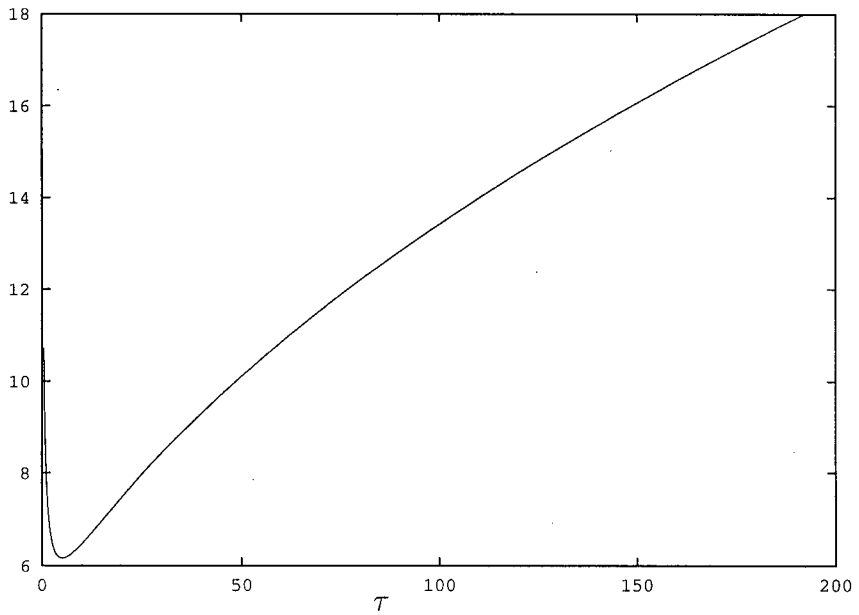

Figure 4.10: Graph of μ_3 as a function of τ for $\gamma = 1$, $\kappa = 5$, $\tau = 10$.

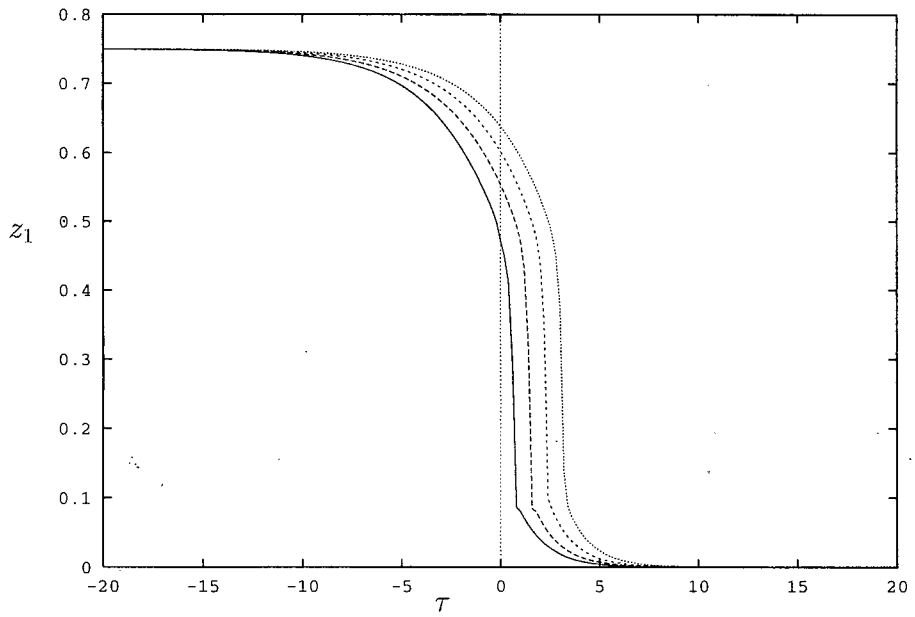

Figure 4.11: Simulation of the traveling front for $\gamma = 1$, $\kappa = 5$, $\tau = 10$.

Chapter 5
Piecewise Linear Continuous Approximation

In this chapter, we will look at the continuum model with a piecewise linear, continuous approximation of the cubic. This function will be qualitatively, and even quantitatively, similar to the cubic. This piecewise linear function has roots at $v = 0$ and $v = 1$ and will attain the same local maximum and local minimum at the same points as the cubic.

The primary motivation for exploring this approximation is that there may be some internal functional structure in these model equations which is important in the behavior of the solution that is not captured in the piecewise linear discontinuous approximation. We will show that for certain parameter ranges, there are three steady states, two of which are stable in the space-clamped case, while the third is a saddle point. Furthermore, we show that there is, in fact, an inner region of the solution, which does not exist in the piecewise linear discontinuous approximation.

We now begin the study of the piecewise linear continuous (PWLC) model, which is given by

$$\frac{\partial v}{\partial t} = \hat{f}(v) + \gamma(w - v), \tag{5.1}$$

$$\frac{\partial w}{\partial t} = \frac{\partial^2 w}{\partial x^2} - \frac{w}{\tau} + \frac{\kappa}{\tau}(v - w), \tag{5.2}$$

where $\gamma > 0$, $\kappa > 0$, $\tau > 0$, and $0 < a < 1$.

In order to write a formula for $\hat{f}$ explicitly, we first need to determine the local maximum/minimum of f and the points where they occur. Differentiating f with respect to v, we find the roots of

$$f'(v_0) = -3v_0^2 + 2(a+1)v_0 - a = 0 \tag{5.3}$$

to be

$$v_{min} = \frac{a+1-\sqrt{a^2-a+1}}{3}, \tag{5.4}$$

$$v_{max} = \frac{a+1+\sqrt{a^2-a+1}}{3}. \tag{5.5}$$

Given the restrictions on a, it is obvious that $0 < v_{min} < v_{max} < 1$. The local minimum and maximum of f are given by:

$$f_{min} = f(v_{min}), \tag{5.6}$$

$$f_{max} = f(v_{max}), \tag{5.7}$$

respectively. If we choose $\hat{f}(0) = 0 = \hat{f}(1)$, then we may write

$$\hat{f}(v) = \begin{cases} m_1 v, & -\infty < v < v_{min}, \\ m_2 v + b_2, & v_{min} < v < v_{max}, \\ m_3 v + b_3, & v_{max} < v, \end{cases} \tag{5.8}$$

where

$$m_1 = \frac{f_{min}}{v_{min}}, \tag{5.9}$$

$$m_2 = \frac{f_{max} - f_{min}}{v_{max} - v_{min}}, \tag{5.10}$$

$$m_3 = -\frac{f_{max}}{1 - v_{max}}, \tag{5.11}$$

$$b_2 = \frac{f_{min}v_{max} - f_{max}v_{min}}{v_{max} - v_{min}}, \tag{5.12}$$

$$b_3 = \frac{f_{max}}{1 - v_{max}}. \tag{5.13}$$

Since $f_{min} < 0$ and $f_{max} > 0$, we conclude that $m_1 < 0$, $m_2 > 0$, $b_2 < 0$, $b_3 > 0$. This can be determined from the x– and y–intercepts of the different linear pieces of $\hat{f}$.

Now that we have an explicit formula for $\hat{f}$, we can examine the spatially homogeneous steady states.

5.1 Spatially homogeneous steady states and stability

We look for spatially homogeneous steady states, so we are looking for solutions to

$$0 = \hat{f}(v) + \gamma(w - v), \tag{5.14}$$

$$0 = \kappa v - (1 + \kappa)w. \tag{5.15}$$

One obvious solution is the origin, $v = 0 = w$.

The equation of the v nullcline is

$$\begin{aligned} w &= v - \frac{\hat{f}(v)}{\gamma}, \\ &= p(v), \end{aligned} \tag{5.16}$$

while the equation for the w nullcline is

$$w = h(v) = \frac{\kappa}{\kappa + 1} v. \tag{5.17}$$

Since $\hat{f}'(v) < 0$ for $v \epsilon (-\infty, v_{min}) \bigcup (v_{max}, \infty)$, then $p'(v) > 1$ for $v \epsilon (-\infty, v_{min}) \bigcup (v_{max}, \infty)$. On the other hand, $h'(v) = \frac{\kappa}{\kappa+1} < 1$. Thus, there will be three steady states if and only if

$$h(v_{max}) > p(v_{max}). \tag{5.18}$$

This condition is equivalent to

$$\frac{\gamma}{\kappa + 1} < \frac{f_{max}}{v_{max}}. \tag{5.19}$$

To determine the middle steady state, (v_2, w_2), we look for solutions of

$$0 = (m_2 v_2 + b_2) + \gamma(w_2 - v_2), \tag{5.20}$$

$$0 = \kappa v_2 - (1+\kappa) w_2, \tag{5.21}$$

which yields

$$v_2 = -\frac{b_2(\kappa+1)}{(\kappa+1)m_2 - \gamma}, \tag{5.22}$$

$$w_2 = -\frac{b_2 \kappa}{(\kappa+1)}. \tag{5.23}$$

Since $m_2 > \frac{f_{max}}{v_{max}} > \frac{\gamma}{\kappa+1}$ when condition (5.19) holds, we know that $v_2 > 0$. If we substitute m_3 for m_2, and b_3 for b_2 in the above equations and use the fact that $m_3 = -b_3$, then the third steady state, (v_3, w_3), is given by

$$v_3 = \frac{b_3(\kappa+1)}{b_3(\kappa+1) + \gamma}, \tag{5.24}$$

$$w_3 = \frac{b_3 \kappa}{b_3(\kappa+1) + \gamma}. \tag{5.25}$$

The stability of the steady states (let us denote the steady state at the origin as (v_1, w_1)) can be determined by looking at the stability matrix

$$A_i = \begin{bmatrix} m_i - \gamma & \gamma \\ \kappa & -(1+\kappa) \end{bmatrix}, \quad i = 1, 2, 3. \tag{5.26}$$

Its determinant, $det(A_i)$, and trace, $tr(A_i)$ are

$$det(A_i) = -m_i(1+\kappa) + \gamma, \quad i = 1, 2, 3, \tag{5.27}$$

$$tr(A_i) = m_i(1+\kappa) - 1 - \gamma - \kappa, \quad i = 1, 2, 3. \tag{5.28}$$

Since $m_1, m_3 < 0$, we know that $det(A_1), det(A_3) > 0$ and $tr(A_1), tr(A_3) < 0$, so (v_1, w_1) and (v_3, w_3) represent stable steady states. Conversely, since $m_2 > \frac{f_{max}}{v_{max}} > \frac{\gamma}{\kappa+1}$, we know that $det(A_2) < 0$, and this steady state is a saddle point.

Since there are two stable steady states separated by a saddle point in the space-clamped case when condition (5.19) holds, we now inquire into the existence of traveling front solutions between the two steady states.

5.2 Traveling front solutions

We now seek out traveling fronts with constant speed c which traverse a path from the steady state at (v_1, w_1) to the one at (v_3, w_3) as solutions to our PWLC model. As in the previous chapter, we look only for solutions with constant shape and make the reduction to the characteristic

$$z = x - ct. \tag{5.29}$$

Substituting into (5.1) and (5.2), we get

$$-cv' = \hat{f}(v) + \gamma(w - v), \tag{5.30}$$

$$-cw' = w'' - \frac{w}{\tau} + \frac{\kappa}{\tau}(v - w) \tag{5.31}$$

where $'$ denotes differentiation with respect to z. The relevant boundary conditions are

$$\lim_{z\to-\infty} w(z) = w_3, \tag{5.32}$$

$$\lim_{z\to-\infty} v(z) = v_3, \tag{5.33}$$

$$\lim_{z\to\infty} w(z) = 0, \tag{5.34}$$

$$\lim_{z\to\infty} v(z) = 0. \tag{5.35}$$

As in the PWLD model, there is no spatial dependence in the right–hand side of our nonlinear ODE, and the associated boundary conditions are at $\pm\infty$. Thus, without loss of generality, we enforce the condition that

$$v(0) = v_{min}. \tag{5.36}$$

Furthermore, since we expect our solution to be monotonic, we shall require

$$v(z_1) = v_{max} \tag{5.37}$$

where $z_1 < 0$.

If we solve (5.31) for v, we get

$$v = -\frac{\tau}{\kappa}\left[w'' + cw' - \frac{1+\kappa}{\tau}\right]. \tag{5.38}$$

Differentiating the above equation with respect to z, we get

$$v' = -\frac{\tau}{\kappa}\left[w''' + cw'' - \frac{1+\kappa}{\tau}w'\right]. \tag{5.39}$$

We see that the boundary conditions on v become redundant since if w satisfies the boundary conditions (5.32) and (5.34), then the boundary conditions for v are automatically satisfied. Eliminating v and v' in (5.30) using (5.38) and (5.39), respectively, we get

$$cw''' + [c^2 - (\gamma - m_i)]w'' - c\left[\gamma - m_i + \frac{1+\kappa}{\tau}\right]w' + \frac{\gamma - (1+\kappa)m_i}{\tau} = \frac{\kappa b_i}{\tau} \tag{5.40}$$

where $i = 1$ for $v\epsilon(\infty, v_{min})$, $i = 2$ for $v\epsilon(v_{min}, v_{max})$, and $i = 3$ for $v\epsilon(v_{max}, \infty)$. We denote the characteristic polynomial of the above ODE by cp_i where

$$cp_i(y) = cy^3 + \left[c^2 - (\gamma - m_i)\right]y^2 - c\left[\gamma - m_i + \frac{1+\kappa}{\tau}\right]y + \frac{\gamma - (1+\kappa)m_i}{\tau}. \tag{5.41}$$

Notice that $cp_1(0)$, $cp_3(0) > 0$ and $cp_1'(0)$, $cp_3'(0) < 0$ (when $c > 0$), so both of these characteristic polynomials have one negative real root and two with positive real part which may be complex. However, $cp_2(0) < 0$, so it has one positive real root, but may have either two roots with negative real part or two roots with positive real part.

The next step is to search for stationary solutions, that is, solutions for $c = 0$. The reasons for doing this is that it reduces the order of the ODE, so it is easier to solve. Also, it allows us to determine the boundary in parameter space that corresponds to positive speed traveling front solutions.

5.2.1 Stationary front solutions

Here we set $c = 0$ in (5.40) to obtain

$$(m_i - \gamma)w'' + \frac{\gamma - m_i(1+\kappa)}{\tau}w = \frac{b_i\kappa}{\tau}. \tag{5.42}$$

Thus, we define

$$\lambda_i = \sqrt{\frac{\gamma - m_i(1+\kappa)}{\tau(\gamma - m_i)}}, \quad i = 1, 3, \tag{5.43}$$

$$\omega = \sqrt{\frac{m_2(1+\kappa) - \gamma}{\tau(\gamma - m_2)}}, \tag{5.44}$$

and write down a solution for w

$$w(z) = \begin{cases} d_{1,1}e^{\lambda_1 z} + d_{1,2}e^{-\lambda_1 z}, & 0 < z < \infty, \\ d_{2,1}\cos(\omega z) + d_{2,2}\sin(\omega z) + w_2, & z_1 < z < 0, \\ d_{3,1}e^{\lambda_3(z-z_1)} + d_{3,2}e^{-\lambda_3(z-z_1)} + w_3, & -\infty < z < z_1. \end{cases} \tag{5.45}$$

In order to match the boundary condition (5.32), we require $d_{3,2} = 0$, and in order to match the boundary condition (5.34), we require $d_{1,1} = 0$. We now apply C^1 continuity conditions on w, and the matching conditions (5.36) and (5.37).

If we apply continuity and differentiability across $z = 0$, we get

$$d_{1,2} - d_{2,1} = w_2, \tag{5.46}$$

$$-\lambda_1 d_{1,2} - \omega d_{2,2} = 0, \tag{5.47}$$

and if we do the same at $z = z_1$, we obtain

$$d_{3,1} - d_{2,1}\cos(\omega z_1) - d_{2,2}\sin(\omega z_1) = w_2 - w_3, \tag{5.48}$$

$$\lambda_3 d_{3,1} + d_{2,1}\omega\left[\sin(\omega z_1) - d_{2,2}\sin(\omega z_1)\right] = 0. \tag{5.49}$$

Now let us write down the solution for v using (5.38):

$$v(z) = \begin{cases} \frac{d_{1,2}\tau}{\kappa}\left[-\lambda_1^2 + \frac{1+\kappa}{\tau}\right]e^{\lambda_1 z}, & 0 < z < \infty, \\ \frac{\tau}{\kappa}\left[\omega^2 + \frac{1+\kappa}{\tau}\right]\left[d_{2,1}\cos(\omega z) + d_{2,2}\sin(\omega z)\right] + v_2, & z_1 < z < 0, \\ \frac{d_{3,1}\tau}{\kappa}\left[-\lambda_3^2 + \frac{1+\kappa}{\tau}\right]e^{\lambda_3(z-z_1)} + v_3, & -\infty < z < z_1. \end{cases} \tag{5.50}$$

If we apply our matching conditions (5.36) and (5.37), we get

$$\frac{d_{1,2}\tau}{\kappa}\left[\frac{1+\kappa}{\tau}-\lambda_1^2\right] = v_{min}, \tag{5.51}$$

$$\frac{d_{3,1}\tau}{\kappa}\left[\frac{1+\kappa}{\tau}-\lambda_3^2\right]+v_3 = v_{max}. \tag{5.52}$$

If we substitute in for λ_1 and λ_3 in the above equations using (5.43), we get,

$$d_{1,2} = \frac{v_{min}(\gamma-m_1)}{\gamma}, \tag{5.53}$$

$$d_{3,1} = \frac{v_{max}-v_3}{\gamma-m_3}\gamma. \tag{5.54}$$

We may substitute in for $d_{1,2}$ in (5.46) using (5.53) and solve for $d_{2,1}$

$$d_{2,1} = \frac{v_{min}(\gamma-m_1)-\gamma w_2}{\gamma}. \tag{5.55}$$

Similarly, using (5.53) and (5.47), we may solve for $d_{2,2}$

$$d_{2,2} = \frac{v_{min}}{\gamma}\sqrt{\frac{[\gamma-m_2][\gamma-m_1][\gamma-m_1(1+\kappa)]}{m_2(1+\kappa)-\gamma}}. \tag{5.56}$$

We only have to solve for $d_{3,1}$ and z_1 using (5.48) and (5.49). If we let

$$y_1 = \cos(\omega z_1), \tag{5.57}$$

$$y_2 = \sin(\omega z_1), \tag{5.58}$$

$$\alpha_1 = d_{3,1}+w_3-w_2, \tag{5.59}$$

$$\alpha_2 = -\frac{\lambda_3 d_{3,1}}{\omega}, \tag{5.60}$$

then we may rewrite the problem as

$$\begin{bmatrix} d_{2,1} & d_{2,2} \\ -d_{2,2} & d_{2,1} \end{bmatrix}\begin{bmatrix} y_1 \\ y_2 \end{bmatrix} = \begin{bmatrix} \alpha_1 \\ \alpha_2 \end{bmatrix}, \tag{5.61}$$

with solution

$$\begin{bmatrix} y_1 \\ y_2 \end{bmatrix} = \frac{1}{d_{2,1}^2+d_{2,2}^2}\begin{bmatrix} d_{2,1}(d_{3,1}+w_3-w_2)+\frac{d_{2,2}d_{3,1}\lambda_3}{\omega} \\ d_{2,2}(d_{3,1}+w_3-w_2)-\frac{d_{2,1}d_{3,1}\lambda_3}{\omega} \end{bmatrix}. \tag{5.62}$$

Enforcing the condition $y_1^2 + y_2^2 = 1$ gives us a solvability condition on the parameters. However, it turns out that there is an easier way of determining this restriction in a certain case, and we derive the restriction this way. Once this condition is known, we can use the above derivation to obtain the full solution to the problem. The method we use is to integrate (5.30) and (5.31).

First, multiply both sides of (5.31) by w' and integrate from $z = -\infty$ to $z = \infty$ to obtain

$$\int_{-\infty}^{\infty} \left[w''w' - \frac{1+\kappa}{\tau} w'w + \frac{\kappa}{\tau} vw' \right] dz = 0 \tag{5.63}$$

Using integration by parts and the fundamental theorem of calculus, the above expression can be simplified to:

$$\frac{\tau \left(w'(z)\right)^2 - (1+\kappa)\left(w(z)\right)^2 + 2\kappa v(z)w(z)}{2\tau}\Bigg|_{z=-\infty}^{z=\infty} - \kappa\tau \int_{-\infty}^{\infty} v'w\, dz = 0, \tag{5.64}$$

or if we use the boundary conditions $w'(\pm\infty) = 0$, $w(-\infty) = w_3$, $w(\infty) = 0$, $v(-\infty) = v3$, $v(\infty) = 0$, and $w_3 = \frac{\kappa v_3}{\kappa+1}$, we obtain

$$\int_{-\infty}^{\infty} v'w\, dz = -\frac{\kappa v_3^2}{2(1+\kappa)}. \tag{5.65}$$

Now multiply (5.30) by v' and integrate both sides from $z = -\infty$ to $z = \infty$ to obtain

$$0 = \int_{-\infty}^{\infty} \left(\left[\hat{f}(v(z)) - \gamma v(z) \right] v'(z) + \gamma w(z) v'(z) \right) dz. \tag{5.66}$$

Using (5.65) and the fundamental theorem of calculus, we get

$$\int_0^{v_3} \hat{f}(v)\, dv = \frac{\gamma v_3^2}{2(1+\kappa)}. \tag{5.67}$$

We can do the integral on the left in three parts as follows:

$$\begin{aligned}\int_0^{v_3} \hat{f}(v)\,dv &= \int_0^{v_{min}} \hat{f}(v)\,dv + \int_{v_{min}}^{v_{max}} \hat{f}(v)\,dv + \int_{v_{max}}^{v_3} \hat{f}(v)\,dv \\ &= \int_0^{v_{min}} m_1 v\,dv + \int_{v_{min}}^{v_{max}} (m_2 v + b_2)\,dv + \int_{v_{max}}^{v_3} b3(1-v)\,dv \\ &= \frac{m_1 v_{min}^2}{2} + \frac{[v_{max} - v_{min}]\,[m_2(v_{max} - v_{min}) + 2b_2]}{2} \\ &\quad + b_3\,[v_3 - v_{max}]\left[1 - \frac{v_3 + v_{max}}{2}\right] \\ &= \frac{1}{2}\,[f_{max}(v_{max} - v_{min}) + f_{min}v_{max}] + b_3\,[v_3 - v_{max}]\left[1 - \frac{v_3 + v_{max}}{2}\right].\end{aligned} \tag{5.68}$$

Thus, going back to (5.67), we require

$$\frac{1}{2}\,[f_{max}(v_{max} - v_{min}) + f_{min}v_{max}] + b_3\,[v_3 - v_{max}]\left[1 - \frac{v_3 + v_{max}}{2}\right] - \frac{\gamma v_3^2}{2(1+\kappa)} = 0. \tag{5.69}$$

If we let $u = \frac{\gamma}{\kappa+1}$ and substitute in $v_3 = \frac{b_3}{b_3+u}$, we get

$$\frac{1}{2}\,[f_{max}(v_{max} - v_{min}) + f_{min}v_{max}] + b_3\left[\frac{b_3}{b_3+u} - v_{max}\right]\left[\frac{2 - v_{max}}{2} - \frac{b_3}{b_3+u}\right] - \frac{b_3^2 u}{2(b_3+u)^2} = 0. \tag{5.70}$$

If we multiply the above equation by $(b_3+u)^2$ and collect powers of u, we get

$$a_2 u^2 + a_1 u + a_0 = 0, \tag{5.71}$$

where

$$a_0 = \frac{b_3^2}{2}\left[f_{max}(v_{max} - v_{min}) + f_{min}v_{max} + (1 - v_{max})^2\right], \tag{5.72}$$

$$a_1 = b_3\left(\left[f_{max}(v_{max} - v_{min}) + f_{min}v_{max}\right] + b_3\left[\frac{1}{2} - 2v_{max} + v_{max}^2\right]\right), \tag{5.73}$$

$$a_2 = \frac{1}{2}\left[f_{max}(v_{max} - v_{min}) + f_{min}v_{max} - b_3 v_{max}(2 - v_{max})\right]. \tag{5.74}$$

Now a_0, a_1, and a_2 depend only upon a, and it can be shown that for $0 < a < \frac{1}{2}$, $a_0 > 0$, $a_1 < 0$, and $a_2 < 0$, so there is only one positive root to this equation. Also, for $a = \frac{1}{2}$,

$a_0 = 0$ and thus there is one negative root and one zero root. What this shows, in essence, is that there can be no positive speed traveling wave solutions for $a \geq \frac{1}{2}$.

It can be shown that one part of the boundary corresponding to traveling wave solutions is determined by

$$\frac{\gamma}{\kappa + 1} < \frac{-a_1 - \sqrt{a_1^2 - 4a_0 a_2}}{2a_2}. \tag{5.75}$$

If we recall, the result for the PWLD model is that there were usually two values of γ which corresponded to stationary front solutions. It turns out that there is another boundary for zero speed waves in the PWLC model, but it has to be attained in a different manner than the above result. The reason why it does not appear in the integral method we just used is that it occurs as $z_1 \to 0$, and thus v' attains a jump discontinuity which it did not previously have and the above analysis is incorrect. Also, when we tried to solve the problem exactly, we were operating under the assumption that there was an internal matching layer. Again, as before, this second boundary emerges as a consequence of the discontinuity. The same methods and techniques that were used to solve the problem for the stationary fronts in the PWLD model could be used here, in principle.

In order to find the other boundary, we first have to recognize that it occurs for small values of γ. In fact, we assume $\gamma < m_2$ unlike what we had tacitly assumed previously. In this case we have lost our internal matching layer, so our solution for w becomes

$$w(z) = \begin{cases} \hat{d}_{1,2} e^{-\lambda_1 z}, & z > 0, \\ \hat{d}_{3,1} e^{\lambda_3 z} + w_3, & z < 0. \end{cases} \tag{5.76}$$

We can apply our matching conditions, (5.46) and (5.47) to obtain

$$\hat{d}_{1,2} = \hat{d}_{3,1} + w_3, \tag{5.77}$$

$$-\lambda_1 \hat{d}_{1,2} = \lambda_3 \hat{d}_{3,1}. \tag{5.78}$$

We solve the above system of equations to obtain

$$\hat{d}_{1,2} = \frac{\lambda_3 w_3}{\lambda_3 + \lambda_1}, \tag{5.79}$$

$$\hat{d}_{3,1} = -\frac{\lambda_1 w_3}{\lambda_3 + \lambda_1}. \tag{5.80}$$

Now, we use equation (5.38) to write down a solution for v

$$v(z) = \begin{cases} \frac{\hat{d}_{1,2}\tau}{\kappa}\left[\frac{1+\kappa}{\tau} - \lambda_1^2\right] e^{-\lambda_1 z}, & z > 0, \\ \frac{\hat{d}_{3,1}\tau}{\kappa}\left[\frac{1+\kappa}{\tau} - \lambda_3^2\right] e^{-\lambda_3 z} + v_3, & z < 0. \end{cases} \tag{5.81}$$

Here we cannot enforce matching condition (5.36), but we try to enforce the condition we did before in the PWLD model

$$\lim_{z \to 0^+} v(z) = v_{min}, \tag{5.82}$$

which is equivalent to

$$d_{1,2}\left[\frac{1+\kappa}{\tau} - \lambda_1^2\right] = \frac{\kappa v_{min}}{\tau}. \tag{5.83}$$

If we substitute for $\hat{d}_{1,2}$ and λ_1 in the above equation using (5.79) and (5.43), we get

$$\frac{\lambda_3 \gamma}{(\lambda_1 + \lambda_3)(\gamma - m_1)} = \frac{v_{min}}{w_3}. \tag{5.84}$$

Thus we see that there is a second boundary condition for zero speed waves. The above equation could be solved explicitly to yield a lower bound for γ in terms of a and κ.

Our next goal will be to tackle the problem of positive speed traveling wave fronts since we have some idea of the parameter set we require.

5.2.2 Positive speed traveling fronts

We are looking for solutions to equation (5.40) subject to the boundary conditions $w(-\infty) = w_3$ and $w(\infty) = 0$ with $v(0) = v_{min}$ and $v(z_1) = v_{max}$ for some $z_1 < 0$.

Let us denote by $\lambda_{i,j}$ one of the roots of the characteristic polynomial cp_i. We know that cp_1 and cp_3 each have one negative real root and two roots with positive real part. We initially assume that all three roots are real and distinct. We also note that in the limiting case of zero speed solutions, cp_2 had two imaginary roots and one positive real root. Here we initially assume that cp_2 has two complex conjugate roots with negative real part. Thus the solution for w is given by

$$w(z) = \begin{cases} d_{1,1}e^{\lambda_{1,1}z}, & 0 < z < \infty, \\ e^{\mu z}\left[d_{2,1}\cos(\omega z) + d_{2,2}\sin(\omega z)\right] + d_{2,3}e^{\lambda_{2,3}z} + w_2, & z_1 < z < 0, \\ d_{3,2}e^{\lambda_{3,2}(z-z_1)} + d_{3,3}e^{\lambda_{3,3}(z-z_1)} + w_3, & -\infty < z < z_1, \end{cases} \tag{5.85}$$

where $\lambda_{1,1} < 0$, $\mu \pm \omega$ are roots of cp_2 with $\mu < 0$, $\lambda_{2,3} > 0$, and $0 < \lambda_{3,2} < \lambda_{3,3}$.

Now we apply our boundary conditions and matching conditions to pin down some of these constants. Applying C^0, C^1, and C^2 conditions at $z = 0$, we get

$$d_{1,1} - d_{2,1} - d_{2,3} = w_2, \tag{5.86}$$

$$\lambda_{1,1}d_{1,1} - \mu d_{2,1} - \omega d_{2,2} - \lambda_{2,3}d_{2,3} = 0, \tag{5.87}$$

$$\lambda_{1,1}^2 d_{1,1} - \mu^2 d_{2,1} - 2\mu\omega d_{2,2} + \omega^2 d_{2,3} = 0. \tag{5.88}$$

At $z = z_1$, we obtain

$$d_{3,2} + d_{3,3} + w_3 = e^{\mu z_1}\left[d_{2,1}\cos(\omega z_1) + d_{2,2}\sin(\omega z_1)\right] + d_{2,3}e^{\lambda_{2,3}z_1} + w_2, \tag{5.89}$$

$$\begin{aligned} \lambda_{3,2}d_{3,2} + \lambda_{3,3}d_{3,3} = {} & \mu e^{\mu z_1}\left[d_{2,1}\cos(\omega z_1) + d_{2,2}\sin(\omega z_1)\right] \\ & + \omega e^{\mu z_1}\left[-d_{2,1}\sin(\omega z_1) + d_{2,2}\cos(\omega z_1)\right] \\ & + \lambda_{2,3}d_{2,3}e^{\lambda_{2,3}z_1}, \end{aligned} \tag{5.90}$$

$$\begin{aligned} \lambda_{3,2}^2 d_{2,3} + \lambda_{3,3}^2 d_{3,3} = {} & d_{2,1}e^{\mu z_1}\left[\mu^2\cos(\omega z_1) - 2\mu\omega\sin(\omega z_1) - \omega^2\cos(\omega z_1)\right] \\ & + d_{2,2}e^{\mu z_1}\left[\mu^2 sin(\omega z_1) + 2\mu\omega cos(\omega z_1) - \omega^2 sin(\omega z_1)\right] \\ & + \lambda_{2,3}^2 d_{2,3}e^{\lambda_{2,3}z_1}. \end{aligned} \tag{5.91}$$

Unfortunately, no easy formula exists for finding the solution of the $d_{i,j}$ in terms of the $\lambda_{i,j}$. In principle, it is a linear system, but one that does not appear to simplify neatly as in the PWLD model. Thus, we do not attempt to write down a solution for the $d_{i,j}$.

We can write down a solution for v easily using (5.38)

$$v(z) = \begin{cases} -\frac{d_{1,1}\tau}{\kappa} g(\lambda_{1,1}) e^{\lambda_{1,1} z}, & 0 < z < \infty, \\ -\frac{\tau}{\kappa} e^{\mu z} d_{2,1} \left[(\mu^2 - \omega^2 + c\mu - \frac{1+\kappa}{\tau}) \cos(\omega z) - \omega(2\mu + c) \sin(\omega z) \right] & \\ -\frac{\tau}{\kappa} e^{\mu} z d_{2,2} \left[(\mu^2 - \omega^2 + c\mu - \frac{1+\kappa}{\tau}) \sin(\omega z) + \omega (2\mu + c) \cos(\omega z) \right] & \\ -\frac{d_{2,3}\tau}{\kappa} g(\lambda_{2,3}) e^{-\lambda_{2,3} z} + v_2, & z_1 < z < 0, \\ -\frac{\tau}{\kappa} \left[d_{3,2} g(\lambda_{3,2}) e^{\lambda_{3,2}(z - z_1)} + d_{3,3} g(\lambda_{3,3}) e^{\lambda_{3,3}(z - z_1)} \right] + v_3, & -\infty < z < z_1, \end{cases} \tag{5.92}$$

where g is as given previously in (4.63). We can explicitly write down equations for our matching conditions (5.36) and (5.37)

$$d_{1,1} g(\lambda_{1,1}) = -\frac{v_{min}\kappa}{\tau}, \tag{5.93}$$

$$d_{3,2} g(\lambda_{3,2}) + d_{3,3} g(\lambda_{3,3}) = \frac{\kappa(v_3 - v_{max})}{\tau}. \tag{5.94}$$

Thus we are left with the problem of solving 14 transcendental equations (the 8 listed above and the six for the eigenvalues). In general, it is difficult to give a sufficiently accurate initial guess for the Newton method nonlinear equation solver that we are using to determine a solution to such a system. However, we showed previously how one can get two different zero speed solutions, one corresponding to a small value of γ, and one corresponding to a larger value of γ. The small γ problem is a very difficult one to perturb off of, so we do not attempt to do that here. One can perturb off of the large γ solution, but it requires a bit more work than in the PWLD model as we don't have explicit expressions for the $d_{i,j}$ in terms of the eigenvalues. Here we need to use a bit of asymptotics to guess the appropriate scalings for the non–order 1 coefficients.

In order to begin the process, we proceed as in the PWLD model and let $c = \epsilon \ll 1$ and assume that κ, a, and τ are fixed. Let γ be expanded in a power series in ϵ as

$$\gamma = \gamma_0 + \epsilon\gamma_1 + O(\epsilon^2). \tag{5.95}$$

We also need asymptotic expansions of our steady states

$$\begin{aligned}
w_2 &= w_{2,1} + \epsilon w_{2,2} + O(\epsilon^2), && (5.96)\\
w_3 &= w_{3,1} + \epsilon w_{3,2} + O(\epsilon^2), && (5.97)\\
w_{2,1} &= -\frac{b_2(\kappa+1)}{m_2(\kappa+1) - \gamma_0}, && (5.98)\\
w_{2,2} &= \frac{\gamma_1 b_2(\kappa+1)}{[m_2(\kappa+1) - \gamma_0]^2}, && (5.99)\\
w_{3,1} &= \frac{b_3(\kappa+1)}{b_3(\kappa+1) + \gamma_0}, && (5.100)\\
w_{3,2} &= -\frac{\gamma_1 b_3(\kappa+1)}{[b_3(\kappa+1) + \gamma_0]^2}. && (5.101)
\end{aligned}$$

Expansions of v_2 and v_3 can be attained by multiplying the equation for w_2 and w_3, respectively, by $\frac{\kappa+1}{\kappa}$.

In the next step, we seek to find expansions for the eigenvalues. The ones which were $O(1)$ in the limit $\epsilon \to 0$ are easy to handle, and we deal with them first. Thus, we expand $\lambda_{1,1}$, ω, and $\lambda_{3,2}$ as follows

$$\begin{aligned}
\lambda_{1,1} &= \lambda_{1,1}^{(1)} + \epsilon\lambda_{1,1}^{(2)} + O(\epsilon^2), && (5.102)\\
\omega &= \omega^{(1)} + \epsilon\omega^{(2)} + O(\epsilon^2), && (5.103)\\
\lambda_{3,2} &= \lambda_{3,2}^{(1)} + \epsilon\lambda_{3,2}^{(2)} + O(\epsilon^2). && (5.104)
\end{aligned}$$

Following the same techniques as before, we try to find expansions for the "missing eigenvalues" as in the PWLD model. Here, we can expand $\lambda_{2,3}$ and $\lambda_{3,3}$ as we did in the

PWLD model for λ_3. Thus we expect

$$\lambda_{2,3} = \frac{\lambda_{2,3}^{(1)}}{\epsilon} + \lambda_{2,3}^{(2)} + O(\epsilon), \tag{5.105}$$

$$\lambda_{3,3} = \frac{\lambda_{3,3}^{(1)}}{\epsilon} + \lambda_{2,3}^{(2)} + O(\epsilon). \tag{5.106}$$

We also notice that $\mu = 0$ in the limiting zero speed wave case, so we expect to be able to expand μ as:

$$\mu = \epsilon\mu^{(1)} + O(\epsilon^2). \tag{5.107}$$

5.3 Numerical Results

5.3.1 Varying a over its range

In Figure 5.1, we see the fairly classical result that the speed is a monotonic decreasing function of a with the zero–speed wave occurring before $a = 0.5$.

In Figure 5.2, we see that the absolute value of z_1 is a monotonic increasing function of a. This is somewhat counterintuitive as one would expect that when a is decreased, the dendrite should be becoming more excitable, and this should translate into faster moving, steeper solutions. One should note that the absolute value of z_1 corresponds to distance traveled within the wave for the value of v to increase from v_{min} to v_{max}. However, the difference between v_{max} and v_{min},

$$v_{max} - v_{min} = \frac{2\sqrt{a^2 - a + 1}}{3}, \tag{5.108}$$

is a decreasing function of a. Thus, although z_1 is increasing as a decreases, a greater portion of the total height achieved by the traveling front is being traversed, and the solution is not necessarily any less steep.

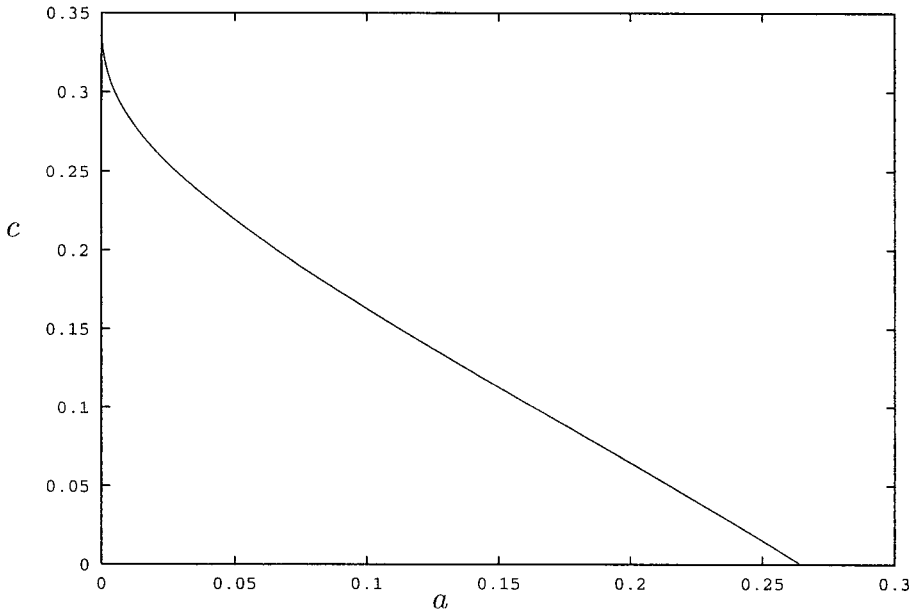

Figure 5.1: Speed of the wave as a function of a for $\gamma = 1.5$, $\kappa = 5$, $\tau = 10$.

5.3.2 Varying κ over its range of values

In Figure 5.3, we see roughly the same relationship between c and κ that we saw in the PWLD model, that is, there is something of a skewed hump which intuitively should asymptote at some positive value of c.

In Figure 5.4, we have plotted z_1 against κ over the range corresponding to traveling front solutions.

Here we see the relationship between z_1 and κ is directly opposite to that between c and κ. One can immediately reason out that this is the case because when the dendrite is highly excitable, this should correspond to high speed, steep solutions. That is, solutions in which c is large and the absolute value of z_1 is small. Conversely, when the dendrite is not highly excitable, this should correspond to low speed, gently sloped solutions. That

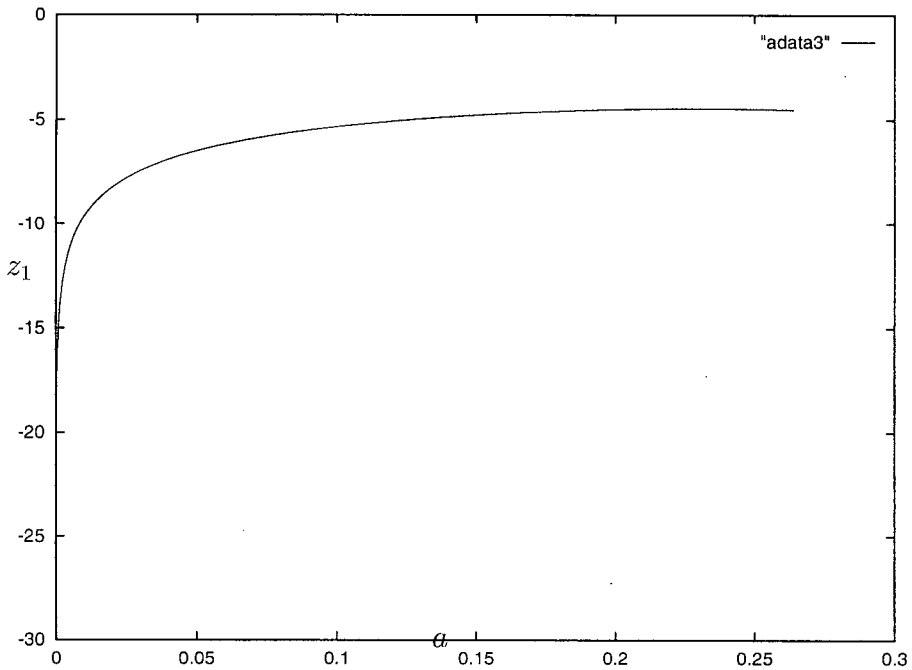

Figure 5.2: z_1 as a function of $\gamma = 1.5$, $\kappa = 5$, $\tau = 10$.

is, solutions in which c is small and the absolute value of z_1 is large.

5.3.3 Varying γ over its range of values

In Figure 5.5, we see the same relationship that we noted in the PWLD model, that is, there appears to be a hump shaped relationship between γ and c. This is due to the balancing factors of the strength of local depolarization, voltage saturation, and current attenuation which are intricately linked to γ.

The next two graphs, Figures 5.6 and 5.7, show where the the assumed functional form of the wave breaks down. When γ becomes small, the roots are no longer complex conjugates in the inner matching region. Instead, they become negative real roots. In Figure 5.6, we see the complex portion of the root going to zero. In Figure 5.7, we see

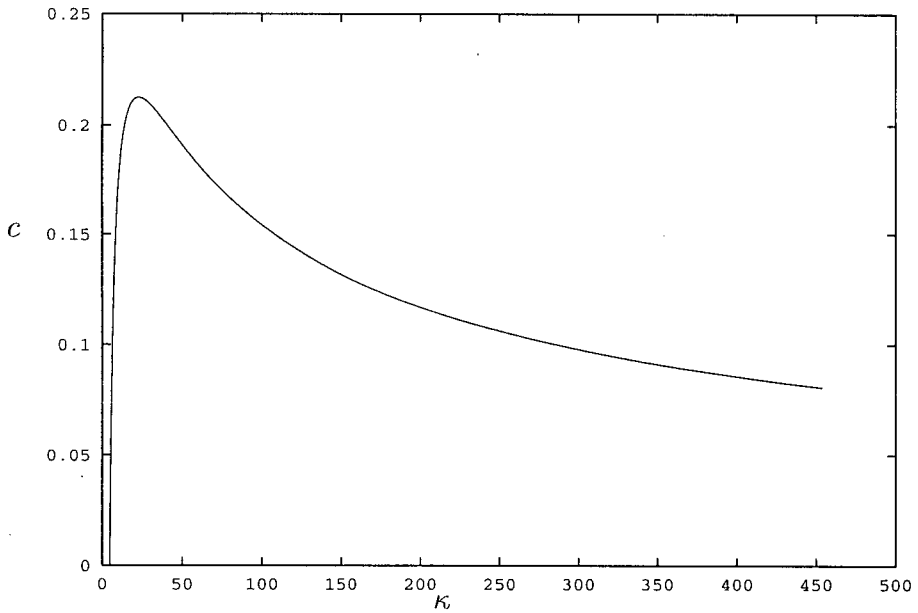

Figure 5.3: Speed of the wave as a function for κ for $a = 0.1$, $\gamma = 1.5$, $\tau = 10$.

the emergence and splitting of the two real roots. This bifurcation was difficult to get numerically. The problem was that non–simple roots are typically very ill–conditioned. Thus, while only an $O(\epsilon)$ change is made in the coefficients of the polynomial, there is an $O(1)$ change in the roots. The easiest way around the problem that I found was to jump comfortably across the bifurcation, and project all other variables across the jump according to a simple linear approximation. Then go back, and accurately calculate the two negative real roots using Maple. One can head back towards the bifurcation site, or move on in the other direction.

In Figure 5.8, we have plotted a graph of z_1 against γ. Here we see that as γ goes to its lower critical value corresponding to zero–speed waves, the inner matching region disappears (i.e., $z_1 \to 0$). This can be understood quite well mechanistically. If γ is small,

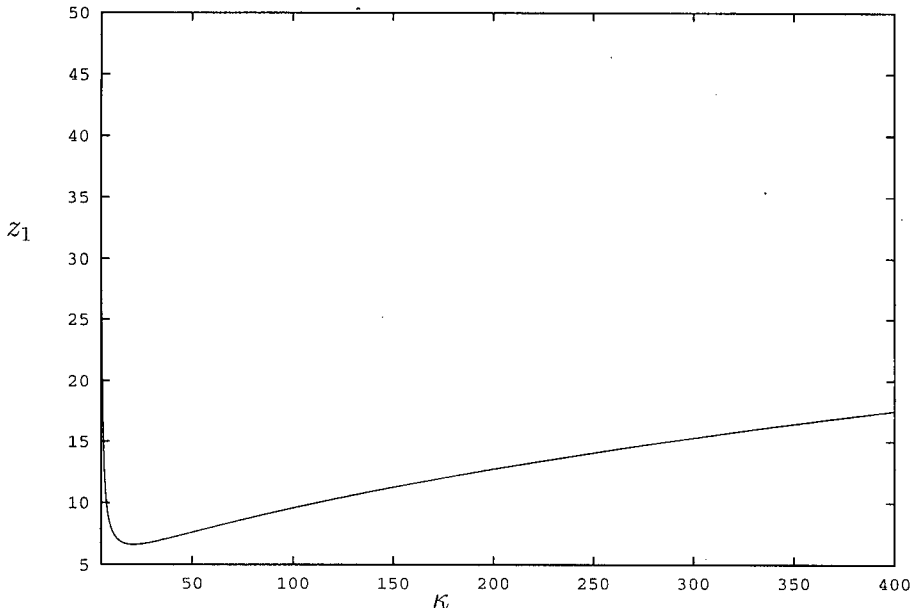

Figure 5.4: z_1 as a function of κ of $a = 0.1$, $\gamma = 1.5$, $\tau = 10$.

there is very strong local depolarization so the spine head voltage should quickly jump to its equilibrium value. This corresponds to a slow–moving wave because it effectively chokes off the current source for the dendrite due to voltage saturation. Conversely, as γ approaches its higher critical value corresponding to zero–speed waves, we see that the absolute value of z_1 is increasing. This is due to the low excitability of the spines which occurs because too much current is being lost to the dendrite. This results in a requirement for a long period of time for the spines to depolarize and thus a large absolute value of z_1.

5.3.4 Varying τ over its range of values

In Figure 5.9, we have graphed $\sqrt{\tau}c$ against τ to compensate for the factor involved in the nondimensionalization and to make it easier to interpret graphically. We see that the

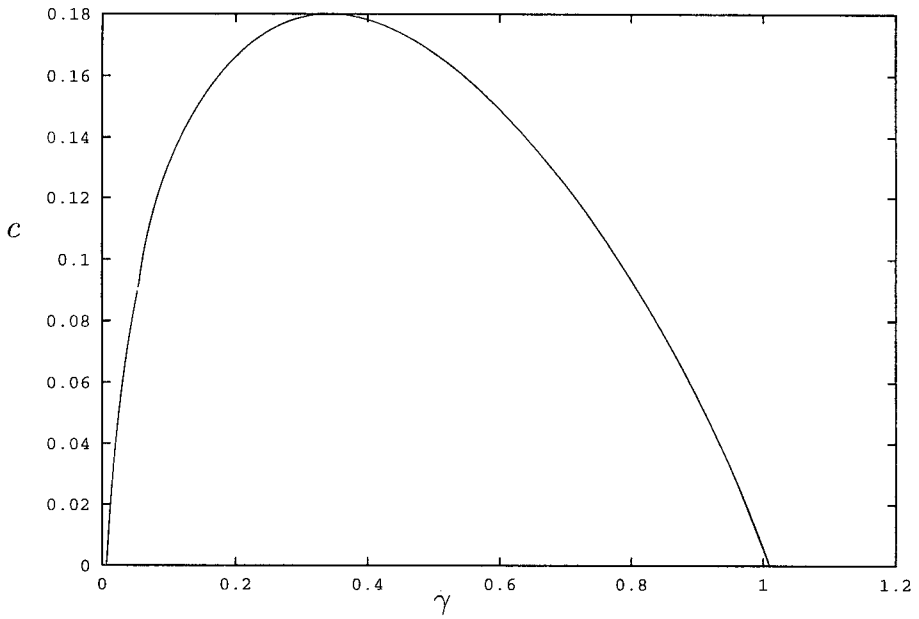

Figure 5.5: Speed of the wave as a function of γ $a = 0.1$, $\kappa = 5$, $\tau = 10$.

speed of the wave, c, is a monotonic increasing function of τ, the nonlinear time scale, which appears to asymptote to some finite positive value just as in the PWLD model.

In Figure 5.10, we have plotted the relationship of z_1 with τ. The graph shows that the magnitude of z_1 is a monotonic decreasing function of τ. This result is intuitively obvious, as the wave should become steeper as the nonlinear dynamics are sped up.

5.3.5 Numerical simulation of the PDE model

The analytical method we developed for numerically finding solutions to the system of ODEs that we derived was very valuable in mapping out some of the relevant parameter ranges, and allowed us quickly to verify numerically some of our intuitive expectations from the PWLD and full Hodgkin–Huxley models. However, these traveling fronts are

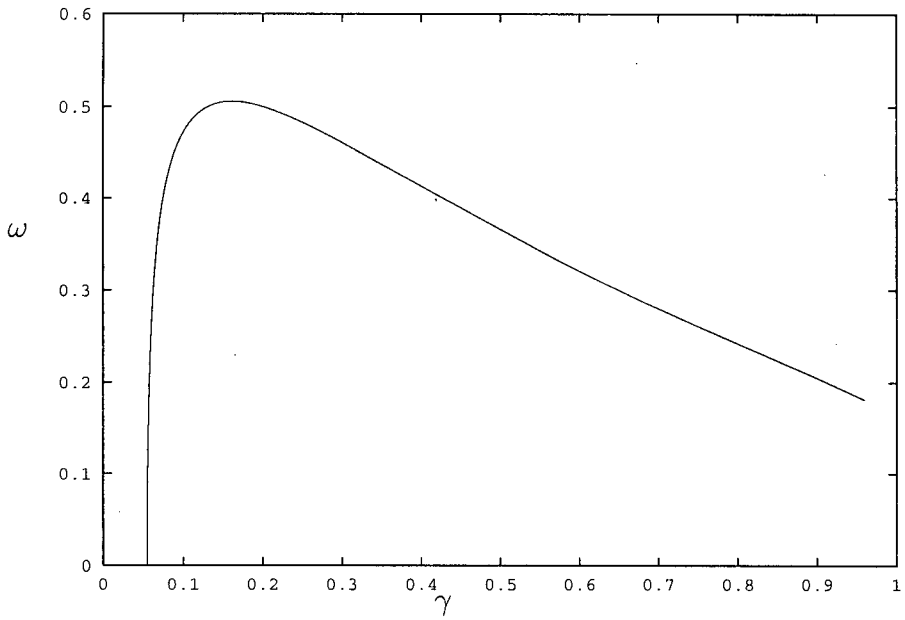

Figure 5.6: ω over the range of γ values for which there are complex conjugate roots for $a = 0.1$, $\kappa = 5$, $\tau = 10$.

not of much experimental importance unless they can be shown to correspond to stable solutions. Lacking a proof of the stability of the system of PDEs, we instead decided to examine the solution numerically using PDEcol. The program was run with Neumann boundary conditions, and the initial guess was the computed solution from our analysis (slight perturbations to the initial guess were made and still gave the same result). The result is shown in Figure 5.11. The traveling front appears to propagate to the right with the theoretically computed speed without changing shape and thus acts as an important check of our analysis.

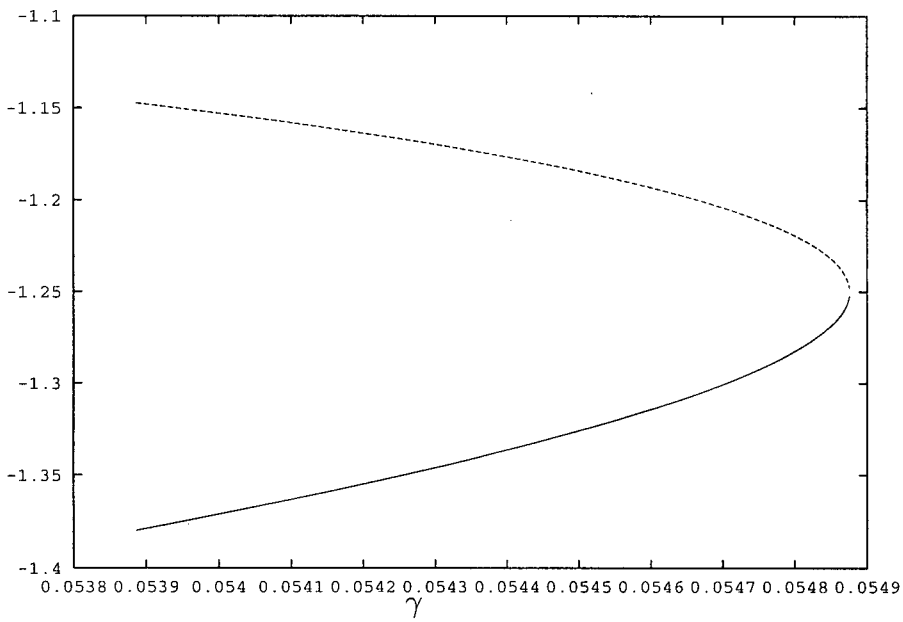

Figure 5.7: The real eigenvalues which exist on the other side of the bifurcation for $a = 0.1$, $\kappa = 5$, $\tau = 10$.

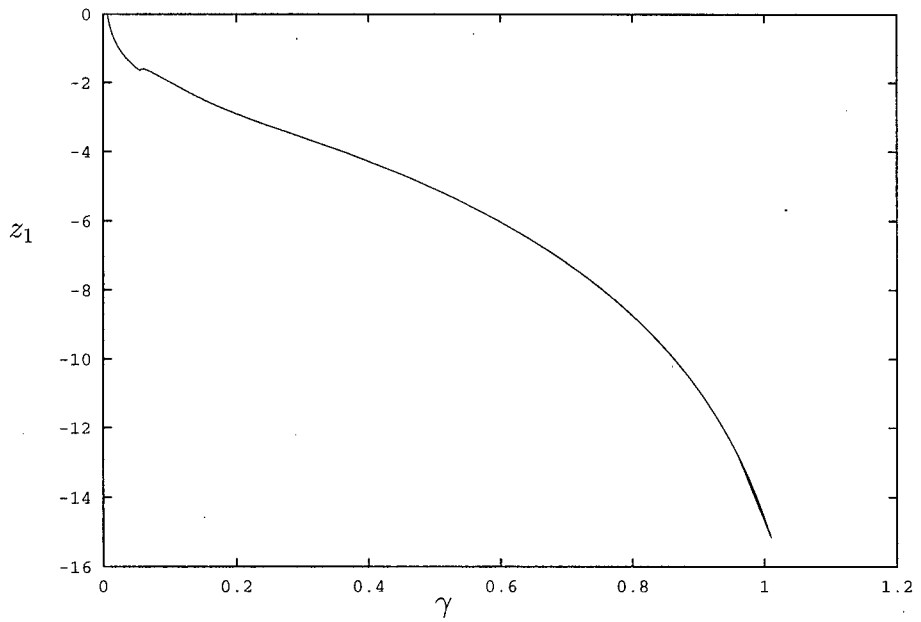

Figure 5.8: Graph of z_1 as a function of γ for $a = 0.1$, $\kappa = 5$, $\tau = 10$.

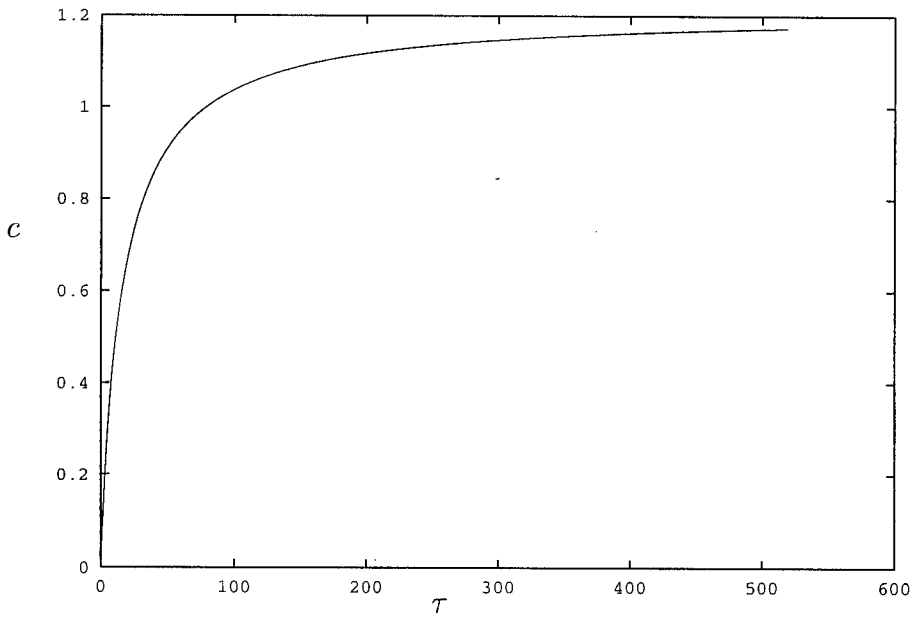

Figure 5.9: Speed of the wave as a function of τ for $a = 0.1$, $\gamma = 1$, $\kappa = 5$.

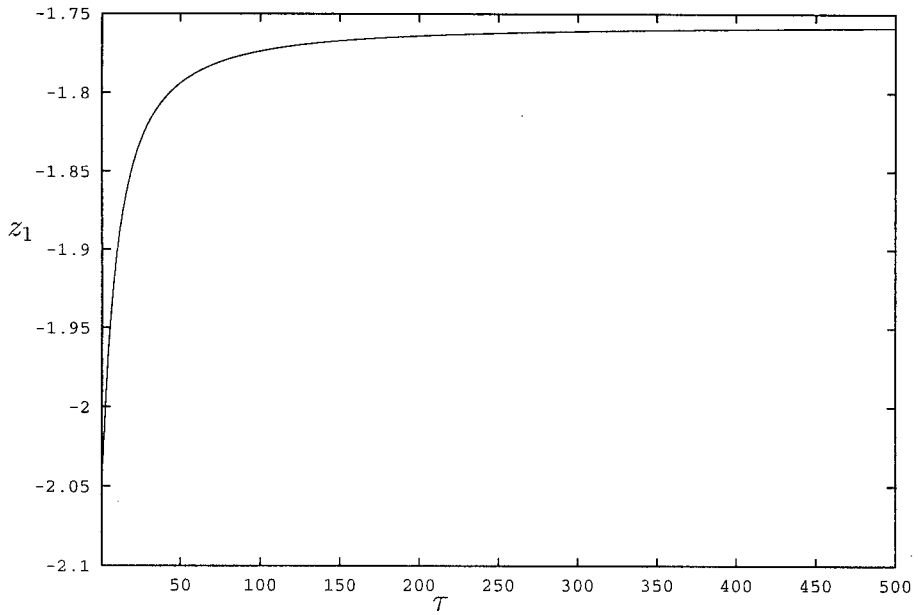

Figure 5.10: z_1 as a function of τ for $\gamma = 1$, $\kappa = 5$, $\tau = 10$.

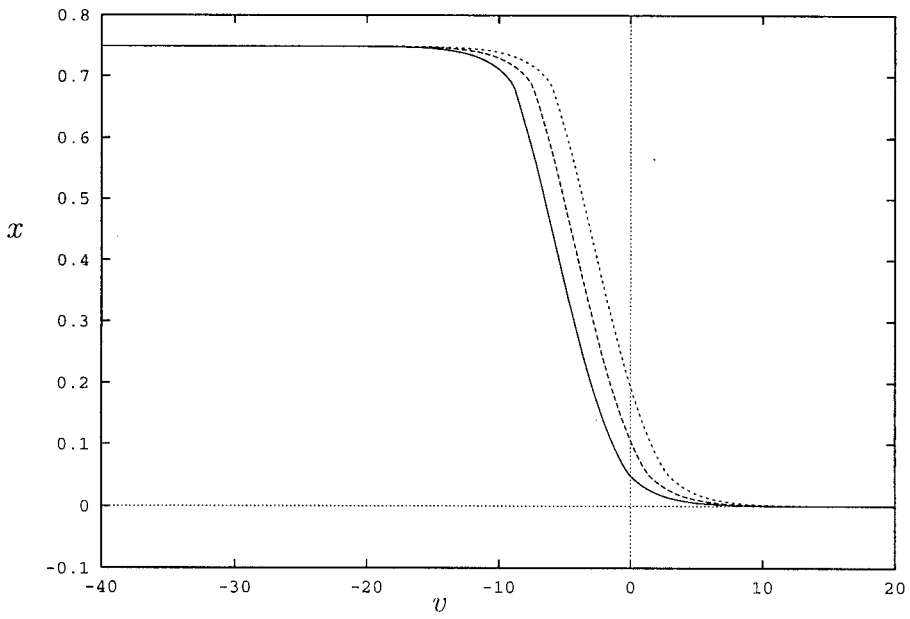

Figure 5.11: This is a simulation of the traveling front for $a = 0.1$, $\gamma = 1$, $\kappa = 5$, $\tau = 10$.

Chapter 6
The Full Cubic Model

In this chapter I will attempt to solve some of the dynamics for the full cubic model. This system will be seen to be similar to an FHN system with reversed kinetics. This reduced system parallels some of the ideas developed for the FHN equations by Rinzel and Terman for bistable steady states.

The main thing that will be seen here is that some of the steps from the analysis of the piecewise linear approximations have natural correlates in the fully nonlinear model. However, there are a couple of important differences which will be noted and will be shown to be artifacts of the discontinuity of the linear interpolations.

The form of the equations that we are studying is

$$\frac{\partial v}{\partial t} = f(v) + \gamma(w - v), \tag{6.1}$$

$$\frac{\partial w}{\partial t} = \frac{\partial^2 w}{\partial x^2} - \frac{w}{\tau} + \frac{\kappa}{\tau}(w - v), \tag{6.2}$$

where $\gamma > 0$, $\kappa > 0$, $\tau > 0$, $0 < a < 1$, and f is given by

$$f(v) = v(v - a)(1 - v). \tag{6.3}$$

6.1 Spatially homogeneous steady states

For spatially homogeneous steady states, we are looking for solutions to

$$\begin{aligned} 0 &= f(v) + \gamma(w - v), \qquad (6.4) \\ 0 &= \kappa v - (1 + \kappa)w. \qquad (6.5) \end{aligned}$$

One obvious solution is the origin, $v = 0 = w$. To determine the existence of other steady states, we have to be a bit more thorough.

The equation of the v nullcline is

$$\begin{aligned} w &= v - \frac{f(v)}{\gamma} \\ &= \frac{p(v)}{\gamma}, \end{aligned} \qquad (6.6)$$

while the equation for the w nullcline is

$$\begin{aligned} w &= \frac{\kappa}{1 + \kappa} v, \\ &= h(v). \end{aligned} \qquad (6.7)$$

Since $f'(0) < 0$, we know that the slope of the v nullcline in the (v, w)-plane is greater than 1 at the origin. However, $h'(0) < 1$, so the v nullcline always passes over the top of the w nullcline at the origin which is exactly the opposite of the case in the FHN equations.

In order to find the other steady states we see that the equilibria must satisfy

$$p(v) - \frac{\gamma\kappa}{1 + \kappa} v = 0, \qquad (6.8)$$

or alternatively,

$$v\left(v^2 - (a + 1)v + a + \frac{\gamma}{1 + \kappa}\right) = 0. \qquad (6.9)$$

The non–zero roots of the above cubic are given by

$$v_2 = \frac{1}{2}\left(a+1+\sqrt{(a-1)^2-\frac{4\gamma}{1+\kappa}}\right), \tag{6.10}$$

$$v_3 = \frac{1}{2}\left(a+1-\sqrt{(a-1)^2-\frac{4\gamma}{1+\kappa}}\right), \tag{6.11}$$

which represent the v components of the steady state. The corresponding w components are obtained by noting that

$$w_i = \frac{\kappa}{1+\kappa}v_i, \quad i=2,3. \tag{6.12}$$

An obvious condition on the existence of these roots is

$$\frac{4\gamma}{1+\kappa} < (1-a)^2. \tag{6.13}$$

If we let $v_1 = 0 = w_1$, then we can determine the stability of the steady states from the eigenvalues of the matrix

$$A_i = \begin{bmatrix} f'(v_i)-\gamma & \gamma \\ \kappa & -(1+\kappa) \end{bmatrix}, \quad i=1,2,3. \tag{6.14}$$

Since $trace(A_1) < 0$ and $det(A_1) > 0$ (since $f'(0) = -a < 0$), we know that the origin is always stable and can be shown to correspond to a stable node. If the inequality (6.13) holds, then we know that v_2 is the second root of (6.8). As this equation is a positive cubic, we see that this cubic must have a negative slope at v_2, and hence

$$p'(v_2) < \frac{\kappa\gamma}{1+\kappa}. \tag{6.15}$$

Thus, substituting for $p'(v_2)$ using inequality (6.15) in the equation for $det(A_2)$, we see that

$$\begin{aligned} det(A_2) &= p'(v_2)(1+\kappa) - \gamma\kappa \\ &< \frac{\gamma\kappa}{1+\kappa}(1+\kappa) - \gamma\kappa \\ &< 0. \end{aligned} \tag{6.16}$$

Thus, this equilibrium point must be a saddle point. Similarly, we can show that

$$p'(v_3) > \frac{\kappa\gamma}{1+\kappa} \tag{6.17}$$

and thus determine that $tr(A_3) < 0$ and $det(A_3) > 0$. Hence, this equilibrium point must be stable. Here we have the classical case of a bistable steady state in the phase plane.

If, however, $\frac{4\gamma}{1+\kappa} = (1-a)^2$, the two roots v_2 and v_3 coalesce into one. In this case, one can easily see that the determinant of the stability matrix should be zero, and we have a nonhyperbolic equilibrium. A center manifold reduction could be attempted here to determine some of the features of this equilibrium, but it is not of much concern here and won't be pursued any further.

Since we now know that there are two stable steady states separated by a saddle point in the space clamped case if inequality (6.13) holds, we now can inquire into the existence of traveling front solutions between the two stable steady states.

6.2 Traveling front solutions

We seek traveling front solutions of the fully nonlinear equations with constant speed c which traverse a path from the steady state at (v_1, w_1) to the one at (v_3, w_3). We proceed as in the previous two chapters and look for solutions with constant shape in the traveling wave coordinate

$$z = x - ct. \tag{6.18}$$

Substituting into (6.1) and (6.2) we get

$$-cv' = f(v) + \gamma(w - v), \tag{6.19}$$

$$-cw' = w'' - \frac{w}{\tau} + \frac{\kappa}{\tau}(v - w), \tag{6.20}$$

where $'$ denotes differentiation with respect to z. The relevant boundary conditions are:

$$\lim_{z\to-\infty} w(z) = w_3, \tag{6.21}$$

$$\lim_{z\to-\infty} v(z) = v_3, \tag{6.22}$$

$$\lim_{z\to\infty} w(z) = 0, \tag{6.23}$$

$$\lim_{z\to\infty} v(z) = 0. \tag{6.24}$$

There are four boundary conditions that we shall try to satisfy for this third–order problem, so the problem is overdetermined.

As in the previous models, our nonlinear ODE is autonomous, and the associated boundary conditions are at ∞. Thus, the problem is translation invariant. Since we know that for some value of z, say z_0, $v(z_0) = v_2$, we may without loss of generality enforce the condition

$$v(0) = v_2. \tag{6.25}$$

The next critical issue is determining the stability of the various equilibria in the traveling wave frame. Let $u = w'$, then we can use the fact that $u' = w''$ to write the above system as the system of three first–order nonlinear ODEs

$$v' = \frac{1}{c}\left[p(v) - \gamma w\right], \tag{6.26}$$

$$w' = u, \tag{6.27}$$

$$u' = \frac{1}{c}\left[-u + \frac{1+\kappa}{\tau}w - \frac{\kappa}{\tau}v\right]. \tag{6.28}$$

The stability matrix of each of the three roots is given by

$$A_i = \begin{bmatrix} \frac{p'(v_i)}{c} & -\frac{\gamma}{c} & 0 \\ 0 & 0 & 1 \\ -\frac{\kappa}{c\tau} & \frac{1+\kappa}{c\tau} & -\frac{1}{c} \end{bmatrix}, \quad i = 1, 2, 3. \tag{6.29}$$

The characteristic polynomials for the equilibria are given by

$$cp_i(\lambda) = \lambda^3 - \left[p^{'}(v_i) - \frac{1}{c}\right]\lambda^2 - \frac{p^{'}(v_i)\tau + 1 + \kappa}{c\tau} + \frac{p^{'}(v_i)(1+\kappa) - \kappa\gamma}{c\tau}, \quad i = 1, 2, 3. \tag{6.30}$$

Since $p^{'}(0) = a + \gamma$, we know that $cp_1(0) > 0$ and $cp_1^{'} < 0$, so cp_1 has one negative real root and two roots with positive real part. Thus, as $z \to \infty$, we have a two–dimensional unstable manifold.

Given inequality (6.15), we assert that $cp_2(0) < 0$ and $cp_2^{'}(0) < 0$, so cp_2 has one positive real root and two roots with negative real part. Thus, as $z \to -\infty$, this equilibrium point has a two–dimensional unstable manifold, and it is unlikely that a trajectory from the equilibrium at $(0, 0, 0)$ could enter this equilibrium.

Similarly, given inequality (6.17), we assert that $cp_3(0) > 0$ and $cp_3^{'}(0) < 0$, so cp_3 has one negative real root and two roots with positive real part. Thus, as $z \to -\infty$, this equilibrium has a two–dimensional stable manifold, so it seems plausible that there may be a path connecting it to the equilibrium at $(0, 0, 0)$ for a certain speed, c.

We notice a problem that we did not have previously. Before, we could explicitly state a general form of the solution by using the fact that the equations were linear with constant coefficients in the various regions. We then could use boundary conditions to try and determine certain coefficients, and the values of z which split up the axis to make everything consistent. Here we first develop a technique to show how one may determine the parameter range which corresponds to zero–speed waves. Then, we show how to obtain an implicit formula for the solution trajectory to the standing wave problem and show that the results are consistent with the analysis done on the previous problem. We verify the results numerically and show the similarity between it and the solution to the PWLC model. Lastly, we suggest a means to perturb off this solution in order to determine the parametric dependence of speed.

6.2.1 Using integration to determine zero speed wave solutions

If we multiply (6.20) by w' and integrate both sides of the equation over $(-\infty, \infty)$, we obtain (using integration by parts, the fundamental theorem of calculus, and the boundary conditions)

$$\begin{aligned} -c\int_{-\infty}^{\infty}(w')^2dz &= \int_{-\infty}^{\infty}\left[w''w' - \frac{1+\kappa}{\tau}ww' + \frac{\kappa}{\tau}vw'\right]dz \\ &= \frac{1}{2}\left[(w')^2 - \frac{1+\kappa}{\tau}w^2\right] + \frac{\kappa}{\tau}vw\Big|_{z=-\infty}^{z=\infty} - \frac{\kappa}{\tau}\int_{-\infty}^{\infty}wv'\,dz, \\ &= \frac{1+\kappa}{2\tau}w_3^2 - \kappa\tau v_3 w_3 - \frac{\kappa}{\tau}\int_{-\infty}^{\infty}wv'\,dz. \end{aligned} \tag{6.31}$$

If we use the above derivation to solve for $\int_{-\infty}^{\infty}wv'dz$, we can use it to derive an implicit equation for c. The first step is to multiply both sides of (6.19) by v' and integrate over $(-\infty, \infty)$ to obtain

$$\begin{aligned} -c\int_{-\infty}^{\infty}(v')^2dz &= \int_{-\infty}^{\infty}\left[(f(v) - \gamma v) + \gamma w\right]v'\,dz \\ &= \int_{v_3}^{0}\left[f(v) - \frac{\gamma}{2}(v^2)'\right]dv + \gamma\int_{-\infty}^{\infty}wv'\,dz. \end{aligned} \tag{6.32}$$

Now we make the substitution described above and isolate the terms involving c on the right to obtain

$$\begin{aligned} -c\int_{-\infty}^{\infty}\left[(v')^2 + \frac{\gamma\kappa}{\tau}(w')^2\right]dz &= \int_{v_3}^{0}f(v)\,dv + \gamma 2v_3^2 + \frac{\gamma(1+\kappa)w_3^2}{2\kappa} - \gamma v_3 w_3 \\ &= -\int_{0}^{v_3}f(v)\,dv + \frac{\gamma v_3^2}{2(1+\kappa)}. \end{aligned} \tag{6.33}$$

Thus, we can obtain the following implicit expression for c

$$c = \frac{\int_0^{v_3}f(v)\,dv - \frac{\gamma}{2(1+\kappa)v_3^2}}{\int_{-\infty}^{\infty}\left[(v')^2 + \frac{\gamma\kappa}{\tau}(w')^2\right]dz}. \tag{6.34}$$

Clearly the denominator in the above expression must always be positive and non–zero for any solution to the system of ODEs we are examining. Thus the speed of the wave equals zero when

$$\int_0^{v_3}f(v)dv - \frac{\gamma}{2(1+\kappa)}v_3^2 = 0. \tag{6.35}$$

If we solve the integral above and do a little bit of algebra we find that

$$v_3^2 - \frac{4(a+1)}{3}v_3 + 2\left(a + \frac{\gamma}{1+\kappa}\right) = 0. \tag{6.36}$$

Recalling the equation for v_3, (6.8), we can derive another constraint

$$v_3^2 - (a+1)v_3 + \left(a + \frac{\gamma}{1+\kappa}\right) = 0. \tag{6.37}$$

We subtract these two equations, yielding

$$\frac{\gamma}{1+\kappa} = \frac{1}{3}(a+1)v_3 - a. \tag{6.38}$$

Substituting the above expression into (6.37), we obtain

$$v_3 = \frac{2}{3}(a+1). \tag{6.39}$$

Then eliminating v_3 in (6.37), we get the tidy result:

$$\frac{\gamma}{1+\kappa} = \frac{2}{9}\left(a - \frac{1}{2}\right)(a-2). \tag{6.40}$$

By analogy, it is easy to see that the positive speed traveling wave fronts should exist if the following inequality is satisfied

$$\frac{\gamma}{1+\kappa} < \frac{2}{9}\left(a - \frac{1}{2}\right)(a-2). \tag{6.41}$$

Now we show a method to determine the profile of a zero-speed solution.

6.2.2 Calculating the profile of a zero–speed front

In this section, we are searching for solutions to the nonlinear ODEs corresponding to $c = 0$. In this case, the ODEs reduce to

$$0 = -p(v) + \gamma w, \tag{6.42}$$

$$0 = w'' - \frac{1+\kappa}{\tau}w + \frac{\kappa}{\tau}v. \tag{6.43}$$

One should notice that the simple change of variable $\hat{z} = \frac{z}{\sqrt{\tau}}$ eliminates τ from the problem. Thus, we shall just adopt the convention that $\tau = 1$ for the analysis that we shall do.

Note that

$$\gamma w^{'} = \frac{dp}{dv} v^{'}, \tag{6.44}$$

$$\gamma w^{''} = \frac{d^2p}{dv^2}(v^{'})^2 + \frac{dp}{dv} v^{''}. \tag{6.45}$$

Substituting these results into (6.43), we obtain the single nonlinear ODE

$$\frac{dp}{dv} v^{''} + \frac{d^2p}{dv^2}(v^{'})^2 - (1+\kappa)p(v) + \kappa\gamma v = 0, \tag{6.46}$$

with the associated boundary conditions given by (6.22) and (6.24), and the enforced condition (6.25).

If we use the assumption that condition (6.40) holds, then we can show that

$$\begin{aligned} \kappa\gamma v - (1+\kappa)p(v) &= \kappa\gamma v - (1+\kappa)v(v^2 - (a+1)v + a + \gamma), \\ &= -(1+\kappa)v\left(v^2 - (a+1)v + a + \frac{\kappa\gamma}{1+\kappa}\right), \\ &= -(1+\kappa)v\left(v - \frac{a+1}{3}\right)\left(v - \frac{2(a+1)}{3}\right), \\ &= F(v). \end{aligned} \tag{6.47}$$

Now let us write

$$\begin{aligned} \frac{dp}{dv} &= 3v^2 - 2(a+1)v + a + \gamma, \\ &= 3\left[\left(v - \frac{a+1}{3}\right)^2 + \rho_o^2\right] \end{aligned} \tag{6.48}$$

where

$$\rho_o^2 = \frac{1}{3}\left[a + \gamma - \frac{(a+1)^2}{3}\right]. \tag{6.49}$$

Thus,

$$\frac{d^2p}{dv^2} = 6\left(v - \frac{a+1}{3}\right). \tag{6.50}$$

There is a natural change of variables to try in order to minimize the algebra

$$u = \frac{v - \frac{1}{3}(a+1)}{\frac{1}{3}(a+1)}, \tag{6.51}$$

$$z = \sqrt{1+\kappa}y, \tag{6.52}$$

$$\rho = \frac{9\rho_o^2}{(a+1)^2}. \tag{6.53}$$

Making these substitutions into (6.46), we get

$$3(u^2+\rho^2)\frac{d^2u}{dy^2} + 6u\left[\frac{du}{dy}\right]^2 + u(1-u^2) = 0 \tag{6.54}$$

subject to the boundary conditions

$$\lim_{y\to-\infty} u = 1, \tag{6.55}$$

$$u(0) = 0, \tag{6.56}$$

$$\lim_{y\to\infty} u = -1. \tag{6.57}$$

We can integrate (6.54) in phase space. Define $g = \frac{du}{dy}$. Rewrite the ODE as

$$\frac{dg}{dy} = \frac{-6ug^2 + u(u^2-1)}{3(u^2+\rho^2)}. \tag{6.58}$$

However, we know that $dg/du = (dg/dy)/(du/dy)$, so we may conclude

$$\frac{dg}{du} = \frac{-6ug^2 + u(u^2-1)}{3g(u^2+\rho^2)}. \tag{6.59}$$

If we now rewrite the equation as

$$3(u^2+\rho^2)gdg + (6g^2u + u(1-u^2))du = 0, \tag{6.60}$$

then the ODE given above has the integrating factor

$$\mu = 3(u^2+\rho^2). \tag{6.61}$$

If we now endeavor to integrate partially (the equation is now exact) we can show that the solution is given by

$$\frac{9}{2}(u^2+\rho^2)^2g^2+\phi(u) = \text{constant}, \tag{6.62}$$

$$\frac{d\phi}{du} = 3u(1-u^2)(u^2+\rho^2), \tag{6.63}$$

or

$$\frac{9}{2}(u^2+\rho^2)^2g^2+\frac{u^2}{4}\left[6\rho^2+3(1-\rho^2)u^2-2u^4\right]=k \tag{6.64}$$

where k is some constant. The above equation is even in u, so if $(u,g)=(1,0)$ is a point on the trajectory, then so is $(u,g)=(-1,0)$. The trajectory goes through these points if

$$\frac{1}{4}(1+3\rho^2)=k. \tag{6.65}$$

Now we may rewrite the equation as

$$\frac{9}{2}\left(u^2+\rho^2\right)g^2=\frac{1}{4}(u^2-1)^2(2u^2+1+3\rho^2). \tag{6.66}$$

If we recall that $g=\frac{du}{dy}$, we obtain the result

$$\frac{du}{dy}=\frac{(u^2-1)\sqrt{2u^2+1+3\rho^2}}{\sqrt{18}(u^2+\rho^2)}. \tag{6.67}$$

Applying the condition $u(0)=0$ yields

$$y=\sqrt{18}\int_0^u\frac{(s^2+\rho^2)ds}{(s^2-1)(2s^2+1+3\rho^2)}, \tag{6.68}$$

and integration gives

$$y=3\log_e\sqrt{(2)}u+g_1(u)+\frac{\delta(1+\rho^2)}{2}\left[atanh(\frac{\delta g_2(-u)}{g_1(u)})-atanh(\frac{\delta g_2(u)}{g_1(u)})\right] \tag{6.69}$$

where

$$g_1(u) = \sqrt{2U^2+1+3\rho^2}, \tag{6.70}$$

$$g_2(u) = 3\rho^2+1+2u, \tag{6.71}$$

$$\delta = \frac{1}{\sqrt{3+3\rho^2}}. \tag{6.72}$$

Now that we have shown how to generate implicit solutions to the problem for zero–speed waves, we can see that if we perturb one of the parameters, we should be able to predict the speed of the resulting wave analytically. This is, however, beyond the scope of the present investigation and will be left as an open problem for someone else to pursue. The basic techniques are standard regular perturbation techniques, and the leading order solutions is stated above. The problem should simplify to finding the solution to some linear second–order differential equation which can be solved numerically.

One thing that is somewhat striking about the above result is that it should perhaps generalize to other sets of equations. We now show that this is, in fact, the case.

6.2.3 General method for getting solution trajectories to degenerate reaction–diffusion traveling fronts

The problem can be stated as follows

$$0 = -q(v) + w, \tag{6.73}$$

$$0 = w'' - w + \psi v, \tag{6.74}$$

subject to the boundary conditions

$$\lim_{z\to-\infty} v = v_3, \tag{6.75}$$

$$\lim_{z\to-\infty} w = w_3, \tag{6.76}$$

$$\lim_{z\to\infty} v = 0, \tag{6.77}$$

$$\lim_{z\to\infty} w = 0, \tag{6.78}$$

where (v_3, w_3), $(0, 0)$ represent spatially homogeneous stable steady states and (v_2, w_2) represents a spatially homogeneous unstable steady state, $\psi > 0$, $q(0) = 0$ and is generally a cubic in profile. Here we also assume the auxiliary condition $v(0) = v_2$.

We can proceed as before by noting that $w = q(v)$, and thus

$$w'' = v'' \frac{dq}{dv} + (v')^2 \frac{d^2q}{dv^2}. \tag{6.79}$$

Substituting these results into (6.74), we get

$$\frac{dq}{dv} v'' + \frac{d^2q}{dv^2}(v')^2 - q(v) + \psi v. \tag{6.80}$$

If we let $Q(v) = \psi v - q(v)$ and $g = v'$, we again can simplify the problem by recalling that $\frac{dg}{dv} = \frac{g'}{g}$. If we substitute these relationships into (6.80) , we get

$$\frac{dg}{dv} = -\frac{\frac{d^2q}{dv^2} g^2 + Q(v)}{g \frac{dq}{dv}}, \tag{6.81}$$

which may be rewritten as

$$g \frac{dq}{dv} dg + \left(\frac{d^2q}{dv^2} g^2 + Q(v) \right) dv = 0. \tag{6.82}$$

Now this equation is not exact, but we may determine an integrating factor. If we let

$$M(g, v) = g \frac{dq}{dv}, \tag{6.83}$$

$$N(g, v) = \frac{d^2q}{dv^2} g^2 + Q(v), \tag{6.84}$$

then we notice that

$$\frac{1}{M(g, v)} \left[\frac{dN}{dg} - \frac{dM}{dv} \right]. \tag{6.85}$$

is independent of g. Thus, we know that there is an integrating factor of the form

$$e^{\int \left[\frac{1}{M(g,v)} \left(\frac{dN}{dg} - \frac{dM}{dv} \right) \right] dv} \tag{6.86}$$

The equation is now exact, and the general solution is given by

$$k = \frac{1}{2}(v' \frac{dq}{dv})^2 - \theta(v), \tag{6.87}$$

$$\theta(v) = \int_0^v \frac{dq}{dv} Q(v) dv, \tag{6.88}$$

where k is some constant.

Since $\theta(0) = 0$ and $\lim_{z\to\infty} v' = 0$, we immediately see that $k = 0$. Now in order for this to be possible, we also see that we require $\theta(v) > 0$ for v in the open interval $(0, v_3)$ and $\theta(v_3) = 0$ to match the boundary condition at $z = -\infty$. That is,

$$\int_0^{v_3} \frac{dq}{dv} Q(v) dv = 0. \tag{6.89}$$

We can apply integration by parts here and noting that $Q(v_3) = 0 = Q(0)$, we see that we require

$$\int_0^{v_3} q(v) \frac{dQ}{dv} dv = 0. \tag{6.90}$$

If we follow this derivation for our problem, we will end up with the result:

$$\frac{\gamma\kappa}{\tau} \left[\frac{\gamma v_3^2}{2(1+\kappa)} - \int_0^{v_3} f(v) dv \right] = 0. \tag{6.91}$$

The fact that the speed of the wave goes to zero as $\tau \to \infty$ is something of an anomaly. The actual physical speed of the wave goes to a constant, but in the nondimensionalization of the problem, the distance was scaled by τ so the unit distance goes to ∞ as τ goes to ∞. Here we also see the classical results that the speed of the wave should go to zero as γ and κ become small. Physically, this makes sense, since as $\gamma \to 0$, we have a situation in which current through the dendritic shaft is unable to penetrate into the spine head, Thus spines ahead of the traveling wave cannot reach threshold and create current to continue feeding the wave. Similarly, the speed of the wave should go to zero as $\kappa \to 0$ since there is no source to feed the dendritic shaft voltage. It should be noted here that these results do not agree with the results from the PWLD model, the PWLC model, or the full HH model of Baer and Rinzel. The lack of agreement with the former two can be shown to be due to a lack of sufficient continuity for the source term (i.e., f). The lack of agreement with the full HH equations is almost certainly due to the lack of a recovery term. Intuitively, one would expect the region in parameter space corresponding

to traveling waves to contract in each direction as a recovery term is added, that is, the parameter space for positive speed pulses for the FHN equations with recovery should contain the parameter space for positive speed fronts for the FHN equations without recovery.

6.3 Numerical simulation of the PDE

We decided to attempt a numerical simulation of the full PDE model on PDEcol to ensure that there were actual traveling front solutions in our presumed parameter space. We ran the simulation using Neumann boundary conditions, and used a scaled version of a solution to the PWLC model for the same parameter set as an initial guess. The solution to the PWLC model was scaled so that it had the same height as the solution to the full cubic model, but no alterations in the shape were made. The resulting wavefront solution is plotted in Figure 6.1.

One can see that the PWLC model gave a solution with a fairly similar shape to the cubic model as the shape did not evolve very much with time. Furthermore, the speeds of the fronts were actually quite comparable. However, it should be noted that the slope of the wave front in the cubic case is steeper than the the slope of the PWLC wavefront as would be expected.

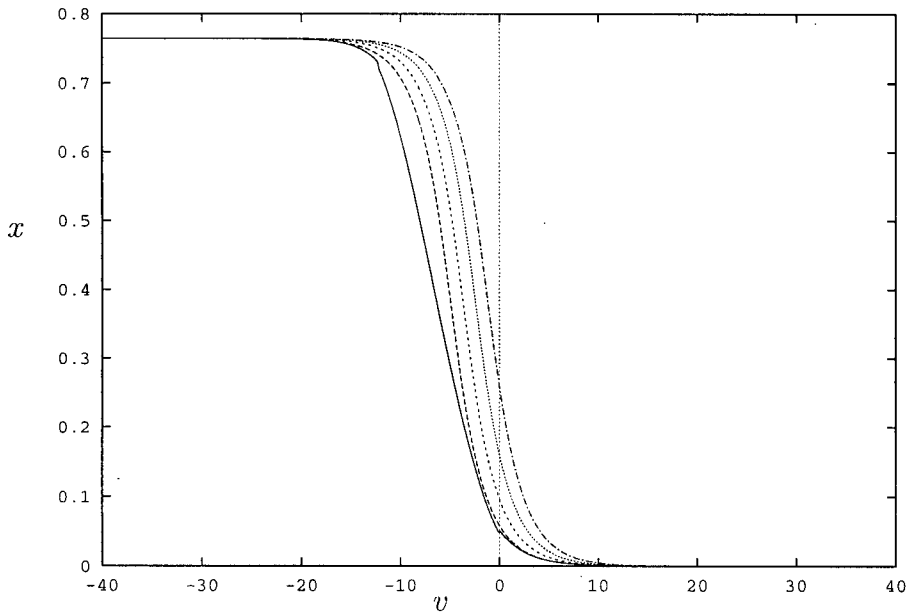

Figure 6.1: This is a simulation of the traveling front for $a = 0.1$, $\gamma = 1$, $\kappa = 5$, $\tau = 10$.

Chapter 7
Discussion

7.1 Theories of spine function

The function of dendritic spines is a mystery that has long plagued neuroscientists. Many different theories have been put forth on their functions, but until recently, they have largely been untestable due to lack of appropriate experimental techniques. With the advent of devices such as fluorescence microscopy and other advances in laboratory equipment, some direct observation of spine function has been possible in recent years. This has intensified the interest in the field amongst experimentalists and theoreticians alike. The main goal of this thesis was to review some of the major theories and study mathematical models put forth on spine function.

In order to understand spine function, one has to understand that spines are the main site of reception of excitatory synaptic transmission. The exact reason for why this is the case has been debated for many years. There are two predominant theories within the field of research. One theory holds that the primary reason is to allow for spatially localized regions in which biochemical reactions mediating changes in synaptic efficacy can be sequestered. This was the primary focus of Chapter 2. The other major theory suggests that spines may have special electrical properties that allow them to modify the size of the EPSP at the axon hillock compared to a neuron without spines. This is the focus of much of Chapter 3. We subsequently explored in greater detail one particular

continuum model of excitable spine heads and proceeded to derive an analogue model based on the Fitzhugh–Nagumo equations. The mathematical analysis of three different models was the focus of Chapters 4, 5, and 6. The main purpose behind these analogue models was that the forms of their equations allow for analytical results which cannot be attained by numerical simulation and may give a deeper understanding of the underlying phenomena.

7.2 Discussion of spines and LTP

7.2.1 Spines and LTP

In Chapter 2, we focused primarily on evidence suggesting a role for spines in mediating a localized memory phenomena known as long–term potentiation (LTP). We introduced some of the important features of LTP such as cooperativity, associativity and input–specificity. We explored three initial models suggesting how spines can play an important role in LTP by allowing high localized concentrations of $[Ca^{2+}]_i$ to develop within the spine head in response to high frequency stimulation. This high level of intracellular calcium then could activate a number of calcium–dependent enzymes and unleash a biochemical cascade which eventually culminates in an increased postsynaptic response when that synapse is subsequently activated. These theories focused primarily on the contributory roles of spine morphology, the presence of a specialized postsynaptic receptor known as a NMDAR which has a high calcium conductance and is largely inactive during low frequency activation but highly active during high frequency stimulation, and the presence of calcium buffers and pumps. These models went a long way in demonstrating that the special features of a spine, its shape and size, may be critical in creating a biochemical compartment specific to a particular synapse.

We then proceeded to explore some ideas concerning calcium dynamics within spines. The work of Woolf and Greer [118] showed that spines could develop localized calcium

transients if they had long spine necks, high amounts of buffers, and the absence of calcium–induced calcium release mechanisms in the spine neck. The unfortunate aspect of the above numerical result was that it failed to give one a true qualitative feeling about how all the different factors interplay to produce localized calcium transients in the spine heads. Zador and Koch managed to shed a great deal of light on the subject through a linearization of calcium dynamics through the use of asymptotics [121]. They showed that under certain conditions, the nonlinear calcium dynamics reduce to the cable equation and were able to identify analogues to the concepts of input resistance, time constant and space constant. They showed that the chemical input resistance of the spine head was much larger than the parent dendrite, which allows for much higher increases in $[Ca^{2+}]_i$ in the spine head than the same input would cause on the parent dendrite. Furthermore, the chemical space constant of the spine was also much smaller than the parent dendrite. This means that much higher levels of $[Ca^{2+}]_i$ will be seen in the spine head than at the base of the spine head, which allows for spatial localization of calcium transients. Finally, they showed that the chemical time constant of the spine head was much smaller than the parent dendrite. This only further amplifies the difference in $[Ca^{2+}]_i$ between the spine head and parent dendrite during calcium transients.

We proceeded to explore the temporal nature of calcium transients required in LTP. It was shown that there may be an important role for calcium–induced calcium release processes to keep the level of $[Ca^{2+}]_i$ in the spine head elevated for long enough to allow for the biochemical cascade controlling LTP induction to become sufficiently activated. Finally, we looked at the presumed final common pathway involved in LTP induction, the activation of protein kinases. We focused on how CaMKII's peculiar autophosphorylation capacity may be critical in the induction of LTP, and briefly reviewed the results from a finite Markov chain model of CaMKII function.

We felt it was important to give the reader an understanding of LTP and its relationship

to spine function as this is one of the major fields of interest in neuroscience today.

7.2.2 The electrical properties of spines

In Chapter 3, we explored a number of theories proposed for the unique electrical properties that the presence of spines may confer to neurons. Some of the more prominent ideas put forth in the past include:

- Spines mediate synaptic potential attenuation such that there is a large voltage gradient between the spine head and parent dendrite upon synaptic excitation.
- Spines may allow for linear summation of EPSPs by decreasing nonlinear interactions with neighboring spines.
- The spine neck resistance may be a controller of synaptic weight.
- Spines increase the low–pass filtering capacity of neurons simply by increasing the surface area of dendrites.
- Spines effectively decrease the space constant and input resistance of dendrites while having little effect on the time constant.
- Spines with active channels are computationally richer than passive spines and may allow for a form of pseudosaltatory conduction in dendrites.

We finished the chapter by exploring a continuum model of active dendritic spines. The goal of this model was to simplify the problem of modeling spines by averaging them over the dendrite as a continuous density and thus significantly simplify the problem. Active continuous channels based on the Hodgkin–Huxley equations were placed in the spine head, and a thorough numerical investigation of changing various parameters such as spine neck resistance was made. This model went a long way in allowing more detailed analysis of the possible role of active spine dynamics on dendritic action potentials.

However, the model is still far too complicated to allow for the derivation of any significant numerical results. Instead, it must rely upon brute force numerics to simulate a solution for each individual parameter set.

In order to obtain a better qualitative feeling for the nature of the various parameters in dendritic action potentials, we decided to employ the simpler Fitzhugh–Nagumo dynamics for the Hodgkin–Huxley dynamics. This approach has proven to be very successful in allowing insights to be made into action potential generation in axons by maintaining the basic flavor of the equations, while drastically simplifying the functional form of the PDEs involved. Thus, we derived a continuum model based on active spines with Fitzhugh–Nagumo–type dynamics. We decided to simplify the model in the manner of Bell and Cosner [8] by removing the recovery variable as justified by asymptotics. This reduced the problem to a third–order problem which is analogous to a Fitzhugh–Nagumo system with bistable steady states, which was studied previously by Rinzel and Keller [92].

We now compare and contrast the results from our analogue models.

7.3 Results for the 3 analogue models

7.3.1 The piecewise linear discontinuous model

In Chapter 4, we used the piecewise linear term $-v + H(v - a)$ where H is a Heaviside function instead of the cubic which classically is used in the Fitzhugh–Nagumo equations. We used this equation as it is the simplest one that retains the salient features of a cubic and allows for an initial exploration of the behaviour of the system of PDEs. We started by deriving the conditions under which a bistable steady state exists,

$$\frac{\gamma}{1+\kappa} < \frac{1-a}{a}. \tag{7.1}$$

We further demonstrated that both steady states are stable.

We then began to search for constant speed traveling front solutions that travel with constant speed which go from one steady state to the other. We then proceeded to change the variables into the moving wave frame which allowed us to reduce the problem to a third–order system of ODEs with boundary conditions at $z = \pm\infty$. Since the problem was translation invariant, and we knew that there was some value of z, say z_0, for which $v(z_0) = a$, we arbitrarily imposed the condition that $z_0 = 0$.

Since we were primarily interested in determining the parameter range which corresponded to positive speed traveling front solutions, we can simplify the problem by mapping out the boundary of this region. That is, we can attempt to study the region in parameter space corresponding to zero–speed solutions. This has the effect of reducing the problem to a simple second–order ODE which can be solved explicitly. Moreover, we find that zero–speed waves correspond to

$$\frac{\gamma\kappa}{(1+\gamma)(1+\gamma+\kappa}} = 2a, \tag{7.2}$$

and positive speed solutions occur for the inequality

$$\frac{\gamma\kappa}{(1+\gamma)(1+\gamma+\kappa}} > 2a. \tag{7.3}$$

Interestingly, it can be shown that there are no positive speed solutions for $a > \frac{1}{2}$.

We then proceeded to examine positive speed traveling front solutions in the appropriate parameter range. Our technique was to try and solve the set of nonlinear equations by a Newton's method, but we needed a reasonable approximate solution initially for a given parameter set. An initial guess for a solution corresponding to a slow moving wave was made by perturbation techniques. Having accomplished this, we then could explore the dependence of the shape and speed of the wave in terms of the parameter set by holding three of the parameters fixed and altering the fourth using the method of continuation. Since we were mainly interested in the speed of the wave, we will not comment any further on the shape of the wave.

We were most interested in the effects of the parameters on the speed of the wave. We found that the speed is a monotonic decreasing function of a. This is intuitively obvious since low values of a correspond to more highly excitable systems which should have faster propagating solutions. The speed of the wave has a skewed hump solution for κ with a lower value which corresponds to a zero–speed solution. This is due to the fact that κ is a measurement of the extent to which spines can depolarize the dendritic shaft. However, there is a value of κ corresponding to a maximum speed because increasing spine density beyond a certain limit creates a very large conductance load on the dendritic shaft which must be overcome to bring spines that are on the leading edge of the wave up to threshold. The graph of the speed of the wave against γ also had a skewed hump appearance, but there were two values of γ which corresponded to zero–speed solutions. If γ was too small, the spine would achieve voltage saturation too quickly and not enough current would be delivered to the parent dendrite to bring the set of spines ahead of the front to threshold. Conversely, if γ was too large, too much current would be lost to the parent dendrite, and the spine would be unable to reach voltage threshold. The graph of the speed of the wave against τ was monotonic increasing. This is not surprising since it is intuitively obvious that speeding up the dynamics of the nonlinearities within the spine head should speed up the wave as well. This is seen, and there appears to be a definite maximum speed of the wave.

Our technique of simplifying the original set of equations and parameters to more manageable sets allowed us to do some analytical work suggesting the appropriate balances in parameters to achieve propagating solutions. This gives one a better qualitative feel for the features of dendrites and spines required to allow for dendritic action potentials. This is much more intuitive than studying each of the numerous parameters of the individual model with time–consuming and computationally expensive nonlinear PDEs.

7.3.2 The piecewise linear continuous model

In Chapter 5, we used a piecewise linear continuous (PWLC) approximation of the FitzHugh–Nagumo cubic. This approximation, $\hat{f}$, satisfied $\hat{f}(0) = 0 = \hat{f}(1)$, and $\hat{f}$ achieved the same maximum and minimum as the Fitzhugh–Nagumo cubic at the same points. The general aim in using this approximation was to attempt to reflect more accurately the true shape of the FHN cubic while still retaining the feature that the problem could be reduced down to solving a set of nonlinear algebraic equations.

Most of the salient features of piecewise linear discontinuous (PWLD) model were retained in the piecewise linear continuous model. There were again two stable steady states in the traveling front frame so long as the inequality

$$\frac{\gamma}{1+\kappa} < \frac{f_{max}}{v_{max}} \tag{7.4}$$

is satisfied. This is clearly analogous to the result in the piecewise linear discontinuous model. However, in the PWLC model, there was a third steady state which is a saddle point. Thus, as in the PWLD model, we looked for traveling front solutions going from one stable steady state to the other.

As in the PWLD model, we showed there were no traveling wave solutions for $a > \frac{1}{2}$, and that for a parameter set with $a < \frac{1}{2}$, there are two values of γ which correspond to zero–speed traveling fronts for fixed γ and κ, but only one value for a and κ when the other two parameters are set. Finally, the dependence of the speed of the wave on the different parameters was generally the same in the two models.

One of the major differences between the two models is that the piecewise linear continuous model has an "inner matching region" that the PWLD model lacks, and this generates a new set of eigenvalues. This creates a difference in how the smaller value of γ which corresponds to zero–speed waves, can be calculated. In the PWLC model, this cannot be accomplished directly as in the PWLD model, because the solution is

degenerate. That is, as γ decreases towards its critical value, $c \to 0$ and $z_1 \to 0$. In this case, we can circumvent this problem and discover the lower value of γ by recognizing the disappearance of the "internal matching layer" and the problem becomes similar to the PWLD model in that there is a jump discontinuity in v.

Another dimension that has to be accounted for in the PWLC model is the parametric dependence of z_1 on a, γ, κ and τ. z_1 is a monotonic decreasing function of a, meaning that as a decreases, the distance required for v to reach v_{max} increases. This is to a certain extent counterintuitive. However, it should be noted that z_1 is the distance required for the value of v to go from v_{min} to v_{max} and

$$v_{max} - v_{min} = \frac{2\sqrt{a^2 - a + 1}}{3}, \tag{7.5}$$

so the difference between v_{max} and v_{min} is a decreasing function of a for $a < \frac{1}{2}$. In terms of the relationship between z_1 and κ, we note that z_1 becomes large as κ goes its critical value which corresponds to zero–speed waves, develops a local minimum at roughly the same value of κ for which the maximum speed is obtained, and then begins to increase thereafter as the speed begins to fall. It can easily be reasoned that the same line of reasoning which explained the relationship of speed to κ in terms of the excitability of the system applies to z_1 in terms of the steepness of the solution. The relationship between z_1 and γ is a bit more interesting. For large values of γ, we see that the value of z_1 decreases, which corresponds to the decreased excitability of the system due to excess current loss to the dendrite. However, we also noticed that the value of z_1 went to 0 as γ approached its smaller critical value which corresponds to zero–speed waves. This can be seen to be due to the overexcitability of the spines due to the fact that little current is lost to the dendrite. This results in the rapid firing of spines which is reflected in the small absolute value of z_1, and the small value of c due to the voltage saturation of the spine choking off current transfer to the dendrite. In terms of τ, we get the expected result that z_1 is an increasing function of τ which plateaus at some level. The reasoning

here is related to an increased level of excitability as τ increases which steepens the wave profile.

7.3.3 The cubic model

The cubic model presents unique challenges that are lacking in the PWLC and PWLD models. The foremost problem is the presence of a cubic nonlinearity. In the other models, we knew the general form of the solution would be a linear combination of exponentials in different regions of space. This allowed us to reduce the problem from solving a series of ODEs to solving a system of nonlinear algebraic equations, for which a certain amount of analysis was possible.

Our first step was to analyze the problem in phase space. As in the PWLC model, there are three steady states when

$$\frac{4\gamma}{1+\kappa} < (1-a)^2 \tag{7.6}$$

is satisfied. Furthermore, the first and third roots again can be shown to be stable, while the middle root corresponds to a saddle point. Thus, we again looked for solutions going from one stable steady state to another.

We proceeded to look for zero–speed traveling wave solutions. By using integration techniques, we demonstrated that zero–speed solutions exist when

$$\frac{\gamma}{1+\kappa} = \frac{2}{9}(a-\frac{1}{2})(a-2) \tag{7.7}$$

is satisfied. This result is analogous to the upper limit value of γ corresponding to zero–speed solutions in the PWLC and PWLD models as positive speed solutions exist when

$$\frac{\gamma}{1+\kappa} < \frac{2}{9}(a-\frac{1}{2})(a-2). \tag{7.8}$$

It also shows the same relationship in κ and a in that there is some lower value of κ and upper value of a which correspond to zero–speed waves. However, an important difference was that it was not immediately obvious whether there was a lower value of γ which corresponded to zero–speed solutions. We were able to show in a more general manner later that there were zero–speed solutions, but they were degenerate and occurred in the limit as $\gamma \to 0$. The fact that the PWLC and PWLD models had zero–speed solutions for positive values of γ is a consequence of the lack of sufficient continuity in the equations.

Finally, we calculated the profile of the zero–speed solutions by integrating in phase space and demonstrated that this technique was applicable to all similar degenerate reaction–diffusion systems. The ability to calculate this profile gives us a technique to perturb off this solution using asymptotics to determine an approximate profile of a slow moving wave.

7.4 Future areas of investigation

We reviewed the field of research of mathematical models of LTP induction, and clearly much remains to be done. The biggest challenge that remains to be worked out here are the exact mechanisms of regulation of a huge biochemical cascade of calcium–dependent protein kinases and phosphatases. An interesting project here would be to look into viable forms of regulation that could explain the spatiotemporal requirements of calcium transients required to induce LTP.

There is also much work that can be done in following up theories of the electrical functions of dendritic spines. The two problems that could immediately be taken up are the utilization of asymptotic techniques to perturb off of the zero–speed wave profile that we have calculated to generate approximations of the profile of slow moving waves. Additionally, reaction–diffusion systems with one small diffusion coefficient and a functional form similar to our set of equations also could be handled using asymptotics to perturb

off the degenerate solution profile that we have calculated. Lastly, an interesting problem to pursue would be to try to determine traveling pulse solutions by not excluding the recovery variable that we have dropped. This problem is much more difficult as it greatly increases the dimension of the parameter space and increases the order of the system of ODEs involved from three to four.

7.5 Conclusion

The field of mathematical neurobiology is developing rapidly and many new interesting problems surface every day. It offers an excellent opportunity for theoreticians and experimentalists to work together in gaining a better understanding of the functioning of the central nervous system. Dendritic spines present a unique challenge to theoreticians due to the sparsity of experimental data and the compelling belief that they must be there for some reason. The challenge as always is to determine what they are doing, and how they accomplish it.

Bibliography

[1] W.C. Abraham and M.F. Bear. Metaplasticity: the plasticity of synaptic plasticity. *Trends Neurosci.*, 19:126–130, 1996.

[2] L. Aniksztejn and Y. Ben-Ari. Novel form of long-term potentiation produced by a K^+ channel blocker in the hippocampus. *Nature*, 349:67–69, 1991.

[3] R. Anwyl. Protein kinase C and long–term potentiation in the hippocampus. *Trends Pharm. Sci.*, pages 236–239, 1989.

[4] A. Artola and W. Singer. Long–term depression of excitatory synaptic transmission and its relationship to long–term potentiation. *Trends Neurosci.*, 16:480–487, 1993.

[5] S.M. Baer and J. Rinzel. Propagation of dendritic spikes mediated by excitable spines: a continuum theory. *J. Neurophys.*, 65:874–890, 1991.

[6] Z.I. Bashir, Z.A. Bortolotto, C.H. Davies, N. Berretta, A.J. Irving, A.J. Seal, J.M. Henley, D.E. Jane, J.C. Watkins, and G.L. Collingridge. Induction of LTP in the hippocampus needs synaptic activation of glutamate metabotropic receptors. *Nature*, 363:347–350, 1993.

[7] T. Behnisch and K.G. Reymann. Thapsigargin blocks long–term potentiation induced by weak, but not strong tetanisation in rat hippocampal CA1 neurons. *Neurosci. Lett.*, 192:185–188, 1995.

[8] J. Bell and C. Cosner. Threshold conditions for a diffusive myelinated axon. *J. Math. Biol.*, 18:39–52, 1983.

[9] M.J. Berridge. Inositol trisphosphate and calcium signaling. *Nature*, 361:315–325, 1993.

[10] T. V. P. Bliss and A. R. Gardner-Medwin. Long–lasting potentiation of synaptic transmission in the dentate area of the unanaesthetized rabbit following stimulation of the perforant path. *J. Physiol., Lond.*, 232:357–374, 1973.

[11] T. V. P. Bliss and T. Lomo. Long–lasting potentiation of synaptic transmission in the dentate area of the anaesthetized rabbit following stimulation of the perforant path. *J. Physiol., Lond.*, 232:331–356, 1973.

[12] T.V.P. Bliss and G.L. Collingridge. A synaptic model of memory: long–term potentiation in the hippocampus. *Nature*, 361:31–39, 1993.

[13] Z.A. Bortolotto and G.L. Collingridge. Activation of glutamate metabotropic receptors induces long–term potentiation. *Eur. J. Pharm.*, 214:297–298, 1992.

[14] Z.A. Bortolotto and G.L. Collingridge. Characterisation of LTP induced by the activation of glutamate metabotropic receptors in area CA1 of the hippocampus. *Neuropharm.*, 32:1–9, 1993.

[15] J.M. Bower and D. Beeman. *The Book of Genesis.* Springer Verlag, New York, 1995.

[16] A.P. Braun and H. Schulman. The multifunctional calcium/calmodulin–dependent protein kinase: from form to function. *Annu. Rev. Physiol.*, 57:417–445, 1995.

[17] S.R. Cajal. Estructura de los centros nerviosos de las aves. *Rev. trim. Histol. norm. patol.*, 1:1–10, 1888.

[18] R.G. Casten, H. Cohen, and P.A. Lagerstrom. Perturbation analysis of an approximation of the Hodgkin–Huxley theory. *Quarterly of Applied Mathematics*, XXXII:365–402, 1975.

[19] H.T. Chang. Cortical neurons with particular reference to the apical dendrites. *Cold Spring Harbor Symp. Quant. Biol.*, 17:189–202, 1952.

[20] A.S. Cohen and W.C. Abraham. Facilitation of long–term potentiation by prior activation of metabotropic glutamate receptors. *J. Neurophys.*, 76:953–962, 1996.

[21] R.W. Cohen, J.E. Margulies, P.M. Coulter II, and J.B. Watson. Functional consequences of expression of the neuron–specific, protein kinase C substrate RC3 (neurogranin) in *xenopus* oocytes. *Brain Res.*, 627:147–152, 1993.

[22] R.J. Cormier, M.D. Mauk, and P.T. Kelly. Glutamate iontophoresis induces long–term potentiation in the absence of evoked presynaptic activity. *Neuron*, 10:907–919, 1993.

[23] F. Crick. Do dendritic spines twitch? *Trends Neurosci.*, 5:44–46, 1982.

[24] J.A. Cummings, R.M. Mulkey, R.A. Nicoll, and R.C. Malenka. Ca^{2+} singalling requirements for long-term depression in the hippocampus. *Neuron*, 16:825–833, 1996.

[25] N.B. Fedorov, P. Pasinelli, A.B. Oestreicher, P.N.E. DeGraan, and K.G. Reymann. Antibodies to postsynaptic PKC substrate neurogranin prevent long–term potentiation in hippocampal CA1 neurons. *Eur. J. Neurosci.*, 7:819–822, 1995.

[26] K. Fukunaga, D. Muller, and E. Miyamoto. Increased phosphorylation of Ca^{2+}/calmodulin–dependent protein kinase II and its endogenous substrates in the induction of long–term potentiation. *J. Biol. Chem.*, 270:6119–6124, 1995.

[27] E. Gamble and C. Koch. The dynamics of free calcium in dendritic spines in response to repetitive synaptic input. *Science*, 236:1311–1315, 1987.

[28] D.D. Gerendasy, S.R. Herron, J.B. Watson, and J.G. Sutcliffe. Mutational and biophysical studies suggest RC3/neurogranin regulates calmodulin availability. *J. Biol. Chem.*, 269:22420–22426, 1994.

[29] J.I. Gold and M.F. Bear. A model of dendritic spine Ca^{2+} concentration exploring possible bases for a sliding synaptic modification threshold. *Proc. Natl. Acad. Sci. USA*, 91:3941–3945, 1994.

[30] S.G.N. Grant and A.J. Silva. Targeting learning. *Trends Neurosci.*, 17:71–75, 1994.

[31] E.G. Gray. Axo–somatic and axo–dendritic synapses of the cerebral cortex: An electron microscopic study. *J. Anat.*, 93:420–433, 1959.

[32] P.B. Guthrie, R.W. Davenport, and S.B. Kater. Local calcium regulatory compartments in neurons. *Japanese J. Physiol.*, 43:S139–S151, 1993.

[33] P.B. Guthrie, M. Segal, and S.B. Kater. Independent regulation of Ca^{2+} revealed by imaging dendritic spines. *Nature*, 354:76–80, 1991.

[34] P.I. Hanson, T. Meyer, L. Stryer, and H. Schulman. Dual role of calmodulin in autophosphorylation of multifunctional CaM kinase may underlie decoding of calcium signals. *Neuron*, 12:943–956, 1994.

[35] K.M. Harris and S.B. Kater. Dendritic spines: Cellular specializations imparting both stability and flexibility to synaptic function. *Ann. Rev. Neurosci.*, 17:341–371, 1994.

[36] K.M. Harris and J.K. Stevens. Dendritic spines of CA1 pyramidal cells in the rat hippocampus: Serial electron microscopy with reference to their biophysical characteristics. *J. Neurosci.*, 9:2982–2997, 1989.

[37] J. Harvey and G.L. Collingridge. Thapsigargin blocks the induction of long–term potentiation in rat hippocampal slices. *Neurosci. Lett.*, 139:197–200, 1992.

[38] D.O. Hebb. *The Organization of Behavior.* John Wiley and Sons, Inc., New York, 1949.

[39] O. Herreras. Propagating dendritic action potential mediates synaptic transmission in CA1 pyramidal cells *in situ*. *J. Neurophysiol.*, 64:1429–1441, 1990.

[40] W.R. Holmes. A continuous cable method for determining the transient potential in passive dendritic trees of known geometry. *Biol. Cybern*, 55:115–124, 1986.

[41] W.R. Holmes and W.B. Levy. Insights into associative long–term potentiation from computational models of NMDA receptor–mediated calcium influx and intracellular calcium concentration changes. *J. Neurophysiol.*, 63:1148–1167, 1990.

[42] Jr. H.P. McKean. Nagumo's equation. *Advances in Mathematics*, 4:209–223, 1970.

[43] J. J. B. Jack, D. Noble, and R. W. Tsien. *Electric current flow in excitable cells.* Clarendon Press, Oxford, 1975.

[44] D.B. Jaffe and T.H. Brown. Metabotropic glutamate receptor activation induces calcium waves within hippocampal dendrites. *J. Neurophys.*, 72:471–474, 1994.

[45] D.B. Jaffe, S.A. Fisher, and T.H. Brown. Confocal laser scanning microscopy reveals voltage–gated calcium signals within hippocampal dendritic spines. *J. Neurobiol.*, 25:220–233, 1994.

[46] S.W. Jaslove. The integrative properties of spiny distal dendrites. *Neurosci.*, 47:495–519, 1992.

[47] H. Kaba, Y. Hayashi, T. Higuchi, and S. Nakanishi. Induction of an olfactory memory by the activation of a metabotropic glutamate receptor. *Science Wash. DC*, 265:262–264, 1994.

[48] E.R. Kandel and J.H. Schwartz. *Principles of Neural Science.* Elsevier Science Publishing Co., Inc., New York, 1985.

[49] M. Kawato and N. Tsukahara. Theoretical study on electrical properties of dendritic spines. *J. theor. Biol.*, 103:507–522, 1983.

[50] M. Kawato and N. Tsukahara. Electrical properties of dendritic spines with bulbous end terminals. *Biophys. J.*, 46:155–166, 1984.

[51] E. Klann, S.-J. Chen, and J.D. Sweatt. Persistent protein kinase activation in the maintenance phase of long–term potentiation. *J. Biol. Chem.*, 266:24253–24256, 1991.

[52] C. Koch and T. Poggio. A theoretical analysis of electrical properties of spines. *Proc. R. Soc. Lond. B*, 218:455–477, 1983.

[53] C. Koch and A.M. Zador. The function of dendritic spines: devices subserving biochemical rather than electrical compartmentalization. *J. Neurosci.*, 13:413–422, 1993.

[54] D.M. Kullmann, D.J. Perkel, T. Manabe, and R.A. Nicoll. Ca^{2+} entry via postsynaptic voltage-sensitive Ca^{2+} channels can transiently potentiate excitatory synaptic transmission in the hippocampus. *Neuron*, 9:1175–1183, 1992.

[55] T. Kutsuwada, N. Kashiwabuchi, H. Mori, K. Sakimura, E. Kushiya, K. Araki, H. Meguro, H. Masaki, T. Kumanishi, M. Arakawa, and M. Mishina. Molecular diversity of the NMDA receptor channel. *Nature*, 358:36–41, 1992.

[56] D.J. Linden. Long–term synaptic depression in the mammalian brain. *Neuron*, 12:457–472, 1994.

[57] J.E. Lisman. A mechanism for memory storage insensitive to molecular turnover: a bistable autophosphorylating kinase. *Proc. Natl. Acad. Sci. USA*, 82:3055–3057, 1985.

[58] J.E. Lisman. A mechanism for the Hebb and the anti–Hebb processes underlying learning and memory. *Proc. Natl. Acad. Sci. USA*, 86:9574–9578, 1989.

[59] J.E. Lisman. The CaM Kinase II hypothesis for the storage of synaptic memory. *Trends Neurosci.*, 17:406–412, 1994.

[60] J.E. Lisman and M.A. Goldring. Feasibility of long–term storage of graded information by the Ca^{2+}/calmodulin–dependent protein kinase molecules of the postsynaptic density. *Proc. Natl. Acad. Sci. USA*, 85:5320–5324, 1988.

[61] R.C. Malenka. Postsynaptic factors control the duration of synaptic enhancement in area CA1 of the hippocampus. *Neuron*, 6:53–60, 1991.

[62] R.C. Malenka, J.A. Kauer, D.J. Perkel, M.D. Mauk, P.T. Kelly, R.A. Nicoll, and M.N. Waxham. An essential role for postsynaptic calmodulin and protein kinase activity in long–term potentiation. *Nature*, 340:554–557, 1989.

[63] R.C. Malenka, J.A. Kauer, R.S. Zucker, and R.A. Nicoll. Postsynaptic calcium is sufficient for potentiation of hippocampal synaptic transmission. *Science*, 242:81–84, 1988.

[64] R.C. Malenka, B. Lancaster, and R.S. Zucker. Temporal limits on the rise in postsynaptic calcium required for the induction of long-term potentiation. *Neuron*, 9:121–128, 1992.

[65] R. Malinow, H. Schulman, and R.W. Tsien. Inhibition of postsynaptic PKC or CaMKII blocks induction but not expression of LTP. *Science*, 245:862–866, 1989.

[66] M.R. Martzen and J.R. Slemmon. The dendritic peptide neurogranin can regulate a calmodulin–dependent target. *J. Neurochem.*, 64:92–100, 1995.

[67] E. McGlade-McCulloch, H. Yamamoto, S. Tan, D.A. Brickey, and T.R. Soderling. Phosphorylation and regulation of glutamate receptors by calcium/calmodulin–dependent protein kinase II. *Nature*, 362:640–643, 1993.

[68] T. Meyer, P.I. Hanson, L. Stryer, and H. Schulman. Calmodulin trapping by calcium–calmodulin dependent protein kinase. *Science*, 256:1199–1202, 1992.

[69] S. Michelson and H. Schulman. CaM kinase: a model for its activation and dynamics. *J. Theor. Biol.*, 171:281–290, 1994.

[70] J.P. Miller, W. Rall, and J. Rinzel. Synaptic amplification by active membranes in dendritic spines. *Brain Res.*, 325:325–330, 1985.

[71] S.G. Miller, B.L. Patton, and M.B. Kennedy. Sequences of autophosphorylation sites in neuronal type II CaM kinase that control Ca^{2+}–independent activity. *Neuron*, 1:593–604, 1988.

[72] H. Miyakawa, W.N. Ross, D. Jaffe, J.C. Callaway, N. Lasser-Ross, J.E. Lisman, and D. Johnston. Synaptically activated increases in Ca^{2+} concentration in CA1 pyramidal cells are primarily due to voltage–gated Ca^{2+} channels. *Neuron*, 9:1163–1173, 1992.

[73] K. Moriyoshi, M. Masu, T. Ishii, R. Shigemoto, N. Mizuno, and S. Nakanishi. Molecular cloning and characterization of the rat NMDA receptor. *Nature*, 354:31–37, 1991.

[74] D. Muller, S. Hefft, and A. Figurov. Heterosynaptic interactions between LTP and LTD in CA1 hippocampal slices. *Neuron*, 14:599–605, 1995.

[75] W. Muller and J.A. Connor. Dendritic spines as individual neuronal compartments for synaptic Ca^{2+} responses. *Nature*, 354:73–76, 1991.

[76] N. Murakami, N. Sakai, K. Nei, S. Matsuyama, N. Saito, and C. Tanaka. Potassium and calcium channel involvement in induction of long–lasting synaptic enhancement by calyculin a, a protein phosphatase inhibitor, in rat hippocampal CA1 region. *Neurosci. Lett.*, 176:181–184, 1994.

[77] D. Neveu and R.S. Zucker. Postsynaptic levels of $[Ca^{2+}]_i$ needed to trigger LTD and LTP. *Neuron*, 16:619–629, 1996.

[78] M.C. Nowycky and M.J. Pinter. Time courses of calcium and calcium–bound buffers following calcium influx in a model cell. *Biophys. J.*, 64:77–91, 1993.

[79] A. Obenaus, I. Mody, and K.G. Baimbridge. Dantrolene–Na (dantrium) blocks induction of long–term potentiation in hippocampal slices. *Neurosci. Lett.*, 98:172–178, 1989.

[80] C.C. Ouimet, E.F. da Cruz e Silva, and P. Greengard. The α and $\gamma 1$ isoforms of protein phosphatase 1 are highly and specifically concentrated in dendritic spines. *Proc. Natl. Acad. Sci. USA*, 92:3396–3400, 1995.

[81] D.H. Perkel. The functional role of dendritic spines. *J. Physiol., Paris*, 78:695–699, 1983.

[82] D.H. Perkel and D.J. Perkel. Dendritic spines: role of active membrane in modulating synaptic efficacy. *Brain Res.*, 325:331–335, 1985.

[83] D.J. Perkel, J.J. Petrozzino, R.A. Nicoll, and J.A. Connor. The role of Ca^{2+} entry via synaptically activated NMDA receptors in the induction of long–term potentiation. *Neuron*, 11:817–823, 1993.

[84] J.J. Petrozzino, L.D.P. Miller, and J.A. Connor. Micromolar Ca^{2+} transients in dendritic spines of hippocampal pyramidal neurons in brain slice. *Neuron*, 14:1223–1231, 1995.

[85] D. L. Pettit, S. Perlman, and R. Malinow. Potentiated transmission and prevention of further LTP by increases CaMKII activity in postsynaptic hippocampal slice neurons. *Science*, 266:1881–1885, 1994.

[86] N. Qian and T.J. Sejnowski. An electro–diffusion model for computing membrane potentials and ionic concentrations in branching dendrites, spines and axons. *Biol. Cybern.*, 62:1–15, 1989.

[87] W. Rall and I. Segev. Computational study of an excitable dendritic spine. *J. Neurophys.*, 60:499–523, 1988.

[88] W. Rall and I. Segev. Synaptic integratin and excitable dendritic spine clusters: structure/function. In R.J. Lasek and M.M. Black, editors, *Intrinsic Determinants of Neuronal Form and Function*, volume 37, pages 263–282. Alan R. Liss, Inc., New York, 1988.

[89] W. Rall, G.M. Shepherd, T.S. Reese, and M.W. Brightman. Dendrodendritic synaptic pathway for inhibition in the olfactory bulb. *Experimental Neurology*, 14:44–56, 1966.

[90] W.M. Rall. Dendritic spines, synaptic potency, and neuronal plasticity. In C.D. Woody, K.A. Brown, Jr. T.J. Crow, and J.D. Knispel, editors, *Cellular Mechanisms Subserving Changes in Neuronal Activity*, pages 13–21. University of California Los Angeles, 1974.

[91] K.G. Reymann, U. Frey, R. Jork, and H. Matthies. Polymyxin B, an inhibitor of protein kinase C, prevents the maintenance of synaptic long–term potentiation in hippocampal CA1 neurons. *Brain Res.*, 440:305–314, 1988.

[92] J. Rinzel and J.B. Keller. Travelling wave solutions of a nerve conduction equation. *Biophys. J.*, 13:1313–1337, 1973.

[93] J. Rinzel and D. Terman. Propagation phenomena in a bistable reaction–diffusion system. *SIAM J. Appl. Math.*, 42:1111–1137, 1982.

[94] C. Romano, M.A. Sesma, C.T. McDonald, K. O'Malley, A.N. Van Den Pol, and J.W. Olney. Distribution of metabotropic glutamate receptor 5 mGluR5 immunoreactivity in rat brain. *J. Comp. Neurol.*, 355:455–469, 1995.

[95] G.J. Rose and S.J. Call. Evidence for the role of dendritic spines in the temporal filtering properties of neurons: the decoding problem and beyond. *Proc. Natl. Acad. Sci. USA*, 89:9662–9665, 1992.

[96] G.J. Rose and S.J. Call. Temporal filtering properties of midbrain neurons in an electric fish: implications for the functions of dendritic spines. *J. Neurosci.*, 13:1178–1189, 1993.

[97] A. Schiegg, W. Gerstner, R. Ritz, and J. L. van Hemmen. Intracellular Ca^{2+} can account for the time course of LTP induction: A model of Ca^{2+} dynamics in dendritic spines. *J. Neurophys.*, 74:1046–1055, 1995.

[98] H. Schulman, P.I. Hanson, and T. Meyer. Decoding calcium signals by multifunctional CaM kinase. *Cell Calcium*, 13:400–411, 1992.

[99] M. Segal. Fast imaging of $[Ca^{2+}]_i$ reveals presence of voltage-gated calcium channels in dendritic spines of cultured hippocampal neurons. *J. Neurophysiol.*, 74:484–488, 1995.

[100] M. Segal. Imaging of calcium inside dendrites and spines: Goals, issues, and perspectives. *J. Neurosci. Meth.*, 59:25–29, 1995.

[101] M. Segal. Imaging of calcium variations in living dendritic spines of cultured rat hippocampal neurons. *J. Physiol.*, 486:283–295, 1995.

[102] K. Seki, H.-C. Chen, and K.-P. Huang. Dephosphorylation of protein kinase C substrates, neurogranin, neuromodulin, and MARCKS, by calcineurin and protein phosphatases 1 and 2A. *Archives of Biochemistry Biophysics*, 316:673–679, 1995.

[103] A.H. Sharp, P.S. McPherson, T.M. Dawson, C. Aoki, K.P. Campbell, and S.H. Snyder. Differential immunohistochemical localization of inositol 1,4,5–trisphosphate- and ryandodine–sensitive Ca^{2+} release channels in rat brain. *J. Neurosci.*, 13:3051–3063, 1993.

[104] Y. Shen, S.M. Specht, I.D. Ghislain, and R. Li. The hippocampus: a biologial model for studying learning and memory. *Prog. Neurobiol.*, 44:485–496, 1994.

[105] G.M. Shepherd. The dendritic spine: A multifunctional integrative unit. *J. Neurophysiol.*, 75:2197–2210, 1996.

[106] G.M. Shepherd, K.M. Brayton, J.P. Miller, I. Segev, J. Rinzel, and W.M. Rall. Signal enhancement in distal cortical dendrites by means of interactions between active dendritic spines. *Proc. Natl. Acad. Sci. USA*, 82:2192–2195, 1985.

[107] K. Svoboda, D.W. Tank, and W. Denk. Direct measurement of coupling between dendritic spines and shafts. *Science*, 272:716–719, 1996.

[108] O. Thibault, D. Muller M. Joly, F. Schottler, S. Dudek, and G. Lynch. Long–lasting physiological effects of bath applied N–methyl–d–aspartate. *Brain Res.*, 476:170–173, 1989.

[109] J. von Neumann. *The Brain as a Computer.* Yale University Press, New York, 1957.

[110] J. Wagner and J. Keizer. Effects of rapid buffers on Ca^{2+} diffusion and Ca^{2+} oscillations. *Biophys. J.*, 67:447–456, 1994.

[111] J.-H. Wang and D.-P. Feng. Postsynaptic protein kinase C essential to induction and maintenance of long–term potentiation in the hippocampal CA1 region. *Proc. Natl. Acad. Sci. USA*, 89:2576–2580, 1992.

[112] Jin-Hui Wang and Paul T. Kelly. Postsynaptic injection of Ca^{2+}/cam induces synaptic potentiation requiring CaMKII and pkc activity. *Neuron*, 15:443–452, 1995.

[113] J.B. Watson, J.G. Sutcliffe, and R.S. Fisher. Localization of the protein kinase C phosphorylation/calmodulin–binding substrate rc3 in dendritic spines of neostriatal neurons. *Proc. Natl. Acad. Sci. USA*, 89:8581–8585, 1992.

[114] E.M. Wexler and P.K. Stanton. Priming of homosynaptic long–term depression in hippocampus by previous synaptic activity. *Neuroreport*, 4:591–594, 1993.

[115] J. Wickens. Electrically coupled but chemically isolate synapses: dendritic spines and calcium in a rule for synaptic modification. *Prog. Neurobiol.*, 31:507–528, 1988.

[116] C.J. Wilson. Passive cable properties of dendritic spines and spiny neurons. *J. Neurosci.*, 4:281–297, 1984.

[117] C.J. Wilson. Cellular mechanisms controlling the strength of synapses. *Journal of electron microscopy technique*, 10:293–313, 1988.

[118] T.B. Woolf and C.A. Greer. Local communication within dendritic spines: models of second messenger diffusion in granule cell spines of the mammalian bulb. *Synapse*, 17:247–267, 1994.

[119] T.B. Woolf, G.M. Shepherd, and C.A. Greer. Serial reconstructions of granule cell spines in the mammalian olfactory bulb. *Synapse*, 7:181–192, 1991.

[120] R. Yuste and W. Denk. Dendritic spines as basic functional units of neuronal integration. *Nature*, 375:682–684, 1995.

[121] A. Zador and C. Koch. Linearized models of calcium dynamics: formal equivalence to the cable equation. *J. Neurosci.*, 14:4705–4715, 1994.

[122] A. Zador, C. Koch, and T.H. Brown. Biophysical model of a Hebbian synapse. *Proc. Natl. Acad. Sci USA*, 87:6718–6722, 1990.

[123] A.M. Zador, H. Agmon-Snir, and I. Segev. The morphoelectrotonic transfrom: a graphical approach to dendritic function. *J. Neurosci.*, 15:1669–1682, 1995.

[124] Y. Zhou and J. Bell. Study of propagation along nonuniform excitable fibres. *Math Biosciences*, 119:169–203, 1994.